REPORT DOCUMENTATION PAGE

Form Approved
OMB No. 0704-0188

1. AGENCY USE ONLY (Leave blank)	2. REPORT DATE	3. REPORT TYPE AND DATES COVERED
	Dec, 1995	Final Technical – Jan, 1993–Aug, 1995

4. TITLE AND SUBTITLE
Closed–Loop Control Systems for unsteady Forebodies and Three–Dimensional Pitching Airfoils at High Reynolds Number.

5. FUNDING NUMBERS
AFOSR-F49620-93-0106
IIT-5-54621

2307/CS

AFOSR-TR-96

0112

6. AUTHOR(S)
David R. Williams
Mukund Acharya
A. Frank D'Souza

7. PERFORMING ORGANIZATION NAME(S) AND ADDRESS(ES)
Fluid Dynamics Research Center
Illinois Institute of Technology
3110 S. State St.
Chicago, IL 60616

9. SPONSORING / MONITORING AGENCY NAME(S) AND ADDRESS(ES)
Air Force Office of Scientific Research
110 Duncan Ave., Suite B115
Bolling AFB, DC 20332-0001

NA

10. SPONSORING / MONITORING AGENCY REPORT NUMBER
93-1-0106

11. SUPPLEMENTARY NOTES

12a. DISTRIBUTION / AVAILABILITY STATEMENT

12b. DISTRIBUTION CODE

19960320 074

13. ABSTRACT (Maximum 200 words)
Progress made on closed loop control systems with application to aircraft forebodies and pitching airfoils is described in this report. The three main areas of the investigation included: (1) development of suitable control law algorithms for control of pitching wings and forebodies, (2) vorticity control on three-dimensional swept wings at high angles of attack, and (3) vortex control on forebody models at high angles of attack with unsteady motions. The three areas were investigated in parallel by laboratory experiment and numerical simulations. The numerical simulations examined the ability of distributed suction to control the flow over an airfoil undergoing a pitch-up motion and sinusoidal oscillation. Experiments on the feasibility of controlling dynamic stall using leading-edge suction were conducted. By studying the influence of different parameters such as pitch rate, Reynolds number, suction timing, suction slot size and location, a scaling law for the suction flow rate was developed. The third area of investigation involved closed-loop control of forebody flow vortex asymmetry. By incorporating a closed-loop system, the desired side force could be maintained under a variety of different pitching. The relative performance of linear, nonlinear and neural network control algorithms was explored.

14. SUBJECT TERMS
Closed loop control, high angle of attack maneuverability, unsteady flow control, forebody, airfoils.

15. NUMBER OF PAGES
114

16. PRICE CODE

17. SECURITY CLASSIFICATION OF REPORT	18. SECURITY CLASSIFICATION OF THIS PAGE	19. SECURITY CLASSIFICATION OF ABSTRACT	20. LIMITATION OF ABSTRACT

NSN 7540-01-280-5500

Standard Form 298 (Rev. 2-89)
Prescribed by ANSI Std. 239-18

DTIC QUALITY INSPECTED 1

CLOSED-LOOP CONTROL SYSTEMS FOR UNSTEADY FOREBODIES AND THREE-DIMENSIONAL PITCHING AIRFOILS AT HIGH REYNOLDS NUMBERS

FINAL TECHNICAL REPORT

AFOSR-F49620-93-0106

INVESTIGATORS:

David R. Williams (PI)
Mukund Acharya (Co-PI)
A. Frank D'Souza (Co-PI)

January 1993- August 1995

ILLINOIS INSTITUTE OF TECHNOLOGY

Fluid Dynamics Research Center
&
Mechanical, Materials & Aerospace Engineering Department

Chicago, Illinois 60616

1. Summary

Control systems and theories were studied with application to enhancing aircraft maneuverability at high angles of attack. The effort combined expertise in the area of control theory and fluid mechanics to explore control methodologies on pitching airfoils and aircraft forebodies. The three main areas of the investigation included:

1) development of suitable control law algorithms for control of pitching wings and forebodies,

2) vorticity control on three-dimensional swept wings at high angles of attack, and

3) vortex control on forebody models at high angles of attack with unsteady motions.

The three areas were investigated in parallel by laboratory experiment and numerical simulations.

The numerical simulations examined the ability of distributed suction to control the flow over an NACA-0012 profile and a flat plate undergoing a pitch-up motion and sinusoidal oscillation. A control law was developed using an approach based on Lyapunov's second method to guarantee stability of the controller. Simulations demonstrated the ability to maintain an attached flow over the profiles during the unsteady maneuvering of two-dimensional airfoils.

In the second area, experiments on the feasibility of controlling dynamic stall using leading-edge suction were conducted in a wind tunnel. By studying the influence of different parameters such as pitch rate, Reynolds number, suction timing, suction slot size and location, a scaling law for the suction flow rate was developed. Parameter ranges were identified for complete or partial suppression of the dynamic stall vortex.

The effect of control by suction on unsteady surface pressures was examined under a variety of pitching conditions. The flow state over the airfoil was correlated with surface pressure data that would meet three different control objectives:

1) suppression of dynamic stall vortex,

2) delaying detachment of the vortex

3) maximizing unsteady lift.

The third area of investigation involved experiments on the feasibility of closed-loop control of forebody flow vortex asymmetry. Small amounts of suction through small holes in the tip of the model were used as actuators. With open loop control, the side force due to vortex asymmetry could be removed by adjusting the forebody vortices to a symmetric state. To enhance maneuverability, the side force could be made left or right-handed with small changes in the suction conditions at the tip of the model. By incorporating a closed-loop system, the desired side force could be maintained under a variety of different pitching conditions, provided the angle of attack was less than 55 degrees. The relative performance of linear, nonlinear and neural network control algorithms was explored. For the forebody model the linear PID type of controller offered the best result over the limited range of test conditions.

2. Nomenclature

c	airfoil chord length
C_l	lift coefficient
C_p	pressure coefficient, $2(p - p_\infty)/(\rho U_\infty^2)$
C_y	sectional side force coefficient
C_μ	momentum flux bleed coefficient (* indicates critical value)
C_{ws}	nondimensional wave speed
D	cylinder diameter
E_d	distortion energy
E_o	initial distortion energy
G_s	gain of forebody vortex system
m	mass flow per unit length and span
p	surface pressure
p_∞	reference static pressure
Q, Q_{nd}	dimensionless suction flow rate, $\dot{Q}_s/(U_\infty c^2)$
Q_{opt}	optimum suction rate for a given objective
$\dot{Q}_s$	volumetric suction flow rate
$\dot{Q}_{rf}$	reverse-flow accumulation rate
r_d	ratio of displacement thicknesses (desired/actual)
Re_c	Reynolds number based on chord, $U_\infty c/\nu$
s	coordinate along airfoil surface
S	surface vorticity flux, $(1/\rho)(\partial p / \partial s)$
S^+	dimensionless surface vorticity flux, $2cS/U_\infty$
t_p	time period for pitch-up motion through $\Delta\alpha$
U_e	local external flow speed over airfoil surface
U_∞	free-stream velocity
U_p	tangential velocity of the airfoil nose
U_{rf}	average reverse-flow velocity
U_{ws}	wave speed
U_o	freestream flow speed
v_o	suction or blowing velocity
W_s	slot width
X	coordinate in freestream direction
Y	cross flow coordinate
Z	coordinate along forebody axis
α	angle of attack
α^+	dimensionless pitch rate, $(\Delta\alpha c)/(t_p U_\infty)$
$\dot{\alpha}$	angular velocity (rad/sec)
$\Delta\alpha$	change in angle of attack
ρ	fluid density
ν	kinematic viscosity

3. Introduction

A great deal was learned over the last decade about the behavior of the vortical flows and their influence on the performance of highly maneuverable aircraft. It is known that high angle of attack aerodynamics is dominated by the presence and behavior of strong vortices originating from the forebody, leading edge extensions, swept wings and wing body junctions. Because the evolution of the vorticity into fully-formed vortices is a gradual process, one can modify the strength and arrangement of the vortices by changing their formation process. In some situations very effective control of the forces on aircraft is possible with low-power input. The vortex formation process is understood well enough that it is now feasible to combine our understanding of the flow field physics into feedback control systems will enhance the maneuverability of aircraft. An interdisciplinary effort teaming expertise in the areas of control theory with experimental fluid dynamics developed closed-loop control systems for the forebody and wing components of aircraft, and investigated a number of issues associated with implementing such a systems on prototype aircraft. Throughout the project an emphasis was placed on developing "practical" control methodologies.

It was originally proposed that two generic configurations, which are common to most aircraft be explored, namely, the forebody and the 3-dimensional swept wing. Both flow fields are dominated by strong, well-defined vortices. The ability for rapid transition of the results to application in prototype aircraft was a key objective of the project. However, time constraints in the project limited the unsteady airfoil work to the two-dimensional case only.

A major challenge to the successful design of a feedback control system is finding an efficient control law algorithm. A large portion of the project dealt with the search for a control algorithm that accurately modeled the flow over an airfoil, yet was fast and simple enough to be incorporated on a microprocessor or small computer. Different control strategies were investigated, such as, a two component inviscid outer flow and viscous inner flow model, a control law based on the Lyapunov approach, and a neural nets algorithm. The neural nets approach matured to the point that off-the-shelf software was used to develop controllers for the forebody and pitching airfoil. The effectiveness of the different approaches was evaluated with numerical simulations and wind tunnel experiments. In addition to the development of practical control laws, other issues investigated included flow state identification, management of flow instabilities, development of controllers, the integrated (complex) effects of three dimensionality, flow field unsteadiness, etc.

The performance of the control systems was studied in a variety of different flow conditions, beginning with low-speed steady flow experiments with static models and progressing toward an unsteady flow environment with pitching models at high Reynolds number. The goals were to demonstrate the feasibility of closed-loop control systems to maintain a desired flow state under unsteady conditions that simulate maneuvers of a pitching aircraft, and to identify the major issues to be resolved before implementing the control on prototype aircraft. The ultimate objective was to obtain a sufficient base of knowledge about the integration of the components in a flight vehicle control system, to

allow the designer to develop a feedback control system for prototype aircraft for maneuverability at high angles of attack.

The results are reported in the following three sections describing the computational studies in section 4.A, the experimental pitching airfoil in section 4.B, and forebody flow control studies in section 4.C. Conclusions and recommendations for future work are discussed in section 5.

4. Results

4.A Feedback Control of Unsteady Flow Separation over Airfoils

Principal Investigator - Professor A. Frank D'Souza
Research Assistant - Prashant Rao

Summary of Research Work

The study considered the problem of maintaining attached flow over airfoils undergoing maneuvers that are not known a priori. The approach has applications in aerodynamics where the ability to control unsteady flow separation results in safer and more maneuverable aircraft. The system to be controlled is distributed in nature and described by the nonlinear partial differential equations of boundary layer theory and the continuity equation.

It is impractical to measure, in the field, the pressure gradient and the velocity boundary condition imposed by the potential flow on the boundary layer. A model was therefore developed to determine both the pressure gradient and the velocity boundary condition using the time-history of the motion of the airfoil. Comparison was made with experimental results obtained for a NACA 0012 airfoil undergoing a pitch-up motion and a sinusoidal oscillation about a fixed span-wise axis.

The technique of suction distributed over the airfoil surface was used as the control input for its demonstrated ability to control unsteady separation and its known ability to maintain laminar flow, which results in reduced drag. The approach developed attempts to define the desired state as broadly as possible. The desired state was defined by specifying the ratio of the thickness of the attached layer to the displacement thickness that was to be maintained, r_d. This simplified the problem considerably, since the two dimensional boundary layer equation is replaced by the one dimensional integral momentum equation. A control law was then developed using an approach based on Lyapunov's second method, which guarantees asymptotic stability of the controller provided that the desired state is controllable. Simulation results were obtained that combine the potential flow model with finite difference models of the boundary layer and the control law. The simulations were run considering a flat plate airfoil pitching up at a constant pitch rate. The control law was found to be effective at maintaining attached flow for all the situations considered.

Background and Objectives

The phenomenon of flow separation, in the presence of certain adverse pressure gradients, results in a drastic change in the flow behavior. In internal flows, such as diffusers and turbines, separation results in a loss of performance and lower efficiencies. In the case of lifting surfaces, flow separation at high angles of attack may result in a stall and loss of control. The control of unsteady flow separation is very desirable for expanding the flight envelope of aircraft and enhancing the maneuverability.

The prevention and delay of flow separation has been studied by several investigators in the past and a review is given by Gad-el-Hak and Bushnell (1991). Several methods have been used and these include vortex generators, wall jets, movement of a compliant wall, and boundary layer suction or injection. The control methods in the existing studies are open-loop and the techniques are mostly experimental as reported by Karim and Acharya (1993), and others. The results of a numerical study are given by Visbal (1991). The open-loop control method has the disadvantage that the correct control effort cannot be determined on-line when the unsteady maneuver is not known a priori. Hence, closed loop control is very desirable for these applications.

The system to be controlled was described by nonlinear partial differential equations (PDE), and such systems were also referred to as distributed parameter systems. The closed loop control theory for linear PDE is fairly well developed. The common approach has been to extend the optimal control theory with a quadratic performance index developed for a system of ordinary differential equations, to PDE. The details are given by Tzafestas (1982) and others. The control law requires that the state as a function of time and space coordinates be available for feedback. Since this is not practical, a state estimator based on sensor measurements at a few discrete locations was used for feedback, instead of the actual state. The method of optimal filter estimator (Kalman type) is also well developed for linear PDE as given by Sakawa (1972).

The system under study is described by nonlinear PDE, for which the control theory is not well established. One approach was to develop a nonlinear control law based on the Lyapunov method as done by Franke (1982), and by Anderson and D'Souza (1994). Franke considers the feedback control of temperature, where the system is described by a bilinear PDE. Anderson and D'Souza have studied the feedback control of unsteady flow over a flat pate at zero angle of attack and in a divergent channel to satisfy the dual objectives of prevention of flow separation under adverse pressure gradients and prevention of transition to turbulence (laminar flow control).

This study was concerned with the development of feedback control of unsteady flow separation over airfoils undergoing arbitrary pitching motion. The control input was wall suction, since it has the additional benefit of delaying transition to turbulence. The use of Navier-Stokes equations as a mathematical model to develop a feedback control theory imposes a considerable burden for on-line computations and even for off-line computations required for design. Hence, in this study, the flow near the surface was described by boundary layer equations, and potential flow theory was used outside the boundary layer. The airfoil motion was obtained from sensors and supplied to the potential flow model, which then determined the pressure gradient imposed on the boundary layer, and the unsteady velocity outside the boundary layer.

According to the Moore-Rott-Sears (MRS) criterion, unsteady separation is characterized by the simultaneous vanishing of the shear and velocity at some point of the boundary layer as seen by an observer moving with the separation point. A full velocity profile with positive velocity gradient and a negative curvature everywhere in the boundary layer will result in an attached flow. However, this profile is not unique and there exists a family of such profiles.

Anderson and D'Souza (1994) used a full desired velocity profile as the command to the control system. However, such a profile cannot be chosen arbitrarily, because it may not be controllable or reachable with only boundary control (wall suction), unless it satisfies the boundary layer equations. Hence, a desired profile must be obtained by first solving the boundary layer equations on-line. The results of Anderson and D'Souza showed that an arbitrary desired profile is not controllable with wall suction, and the control system is not asymptotically stable in the Lyapunov sense. However, the desired profile can be approached closely.

In this study the unsteady momentum integral equation was used to design a control law that determines the suction velocity. A full velocity profile in the boundary layer was obtained indirectly. The control law was based on Lyapunov's method which ensured the asymptotic stability of the control system.

Potential Flowfield   The potential flowfield of unsteady airfoils has been studied for the past several years by many investigators, and solutions have been obtained for specific motions. The early studies include the sinusoidal oscillations in pitch considered by Theodorsen, the problem of a step change in the angle of attack studied by Wagner, and the case of a sharp-edged gust by Kussner. Their solutions contain Bessel functions with complex arguments and are known as Theodorsen, Wagner, and Kussner functions, respectively, as discussed by McCroskey (1973).

This study considers a rigid symmetric airfoil executing an arbitrary pitching motion while translating forward at a constant velocity. A noninertial coordinate system which rotates and translates with the airfoil attached to it was used both for the potential flow and for the boundary layer equations. The incompressible, irrotational flow satisfies the two-dimensional Laplace equation, and the general boundary conditions in noninertial body coordinates were discussed by Katz and Plotkin (1991).

The velocity potential was divided into three parts caused by the thickness effect, by the quasi steady instantaneous motion if the wake had no effect, and by the wake effect, respectively. The thickness effect was solved by distributing sources on the airfoil chord from the leading to the trailing edge. Abbot and von Doenhoff (1959) give the thickness of various airfoil profiles. Using their data, a solution to the thickness effect was obtained here for the NACA 0012 airfoil.

The quasi steady instantaneous motion effect was solved by a vorticity distribution from the leading edge up to but not including the trailing edge of the chord. The vorticity at the trailing edge was set to zero to satisfy the Kutta condition. It leads to an integral equation which was originally solved by Sohngen and the details are given by Dowell et al. (1989). This vorticity distribution was obtained in terms of the airfoil instantaneous motion. The wake effect was solved by placing an unknown vorticity distribution along the wake and considering its effect on the bound circulation of the

8

airfoil such that the Kutta condition was satisfied at its trailing edge. The bound circulation around the airfoil caused by the wake effect was solved by Von Karman and Sears (1938) by the method of images.

Finally, the unknown wake vorticity distribution was obtained from the Kelvin condition that the total circulation including the airfoil bound circulation and the wake circulation is zero. This leads to an equation in the form of a convolution integral. Here, it was solved recursively by expressing it as a convolution summation, which was convenient for on-line computation with the motion being obtained from sensor measurements. The velocity tangent to the airfoil upper surface was obtained by summing the contributions of the three potentials. The pressure coefficient Cp was obtained from the unsteady Bernoulli equation in noninertial frame (Katz and Plotkin (1991).

The analytical results for the pressure distribution in unsteady motion were compared with the existing experimental results. Metwally (1990) and Acharya and Metwally (1992) experimentally investigated the unsteady pressure distribution for a NACA 0012 airfoil pitching about its quarter chord line. In their experiments, a constant $d\alpha/dt$, hold-pitch-hold motion of the airfoil was used. The reduced pitch rate is defined as $\alpha+=\dot{\alpha}c/U_\infty$. Comparison between the analytical results of this study and the experimental results of Metwally (1990) for Cp is shown in Figs. 1 and 2 for reduced pitch rates of 0.036 and 0.072, respectively. The agreement is good except close to the leading edge where the analytical model has a singularity.

The analytical results of this study also compared well with other existing experimental results, such as those of St. Hilaire and Carta (1983) for an oscillating airfoil, but these results are not shown here. The potential flow model required some on-line computations which were difficult to do in real time. Hence, a neural network was trained to produce the unsteady flowfield by taking advantage of its parallel nature to considerably reduce the time required by a sequential processor to compute the temporal and spatial distributions of pressure and velocity.

A back propagating neural network was created with the delta learning rule and the hyperbolic tangent function as the activation function. It was trained using the supervised learning strategy. The values of the pressure coefficient used to train and test the network were obtained from the experimental results of Metwally (1990), and the values of the tangential velocity were obtained from the potential flow model (PFM) of this study.

The network is shown in Fig 3. The input layer has two processing elements (PEs) for the angle of attack, and nondimensional pitch rate from motion sensors as inputs. It has one hidden layer consisting of nine PEs for pressure prediction and seven PEs for the tangential velocity prediction. The output layer has 20 PEs for pressure coefficient output at the locations used by Metwally and 20 PEs for velocity at the same locations. The pressure and velocity predictions of this trained network are shown in Figs. 4 and 5, along with the experimental or analytical results. The performance of the network was good.

Feedback Control

Firstly, the Navier-Stokes equation were obtained in the rotating and translating coordinate system used in this study. The boundary layer order of magnitude analysis was used to simplify the equations, which in addition to the usual local and convective acceleration terms, now also contain the centripetal acceleration, angular acceleration, and Coriolis acceleration terms. With the assumptions that the nondimensional pitch rate $\alpha+<<1$, and the nondimensional angular acceleration $\dot{\alpha}+=\ddot{\alpha}c^2U^2<<1$, the equations reduced to the familiar boundary layer equations in an inertial reference frame.

The control objective was to make the normal velocity component zero at a certain distance $h(x,t)$ from the surface, where $h(x,t)$ was greater than the boundary layer thickness. When the boundary layer displacement thickness was a small fraction of the boundary layer thickness, the velocity profile would be full, thus resulting in attached flow. The desired value of $h(x,t)$ was defined as a certain multiple r_d of the displacement thickness, where r_d may be a function of x and t. The control suction velocity was set to zero where the pressure gradient was favorable. Otherwise r_d may be set adaptively as a quadratic function of the pressure gradient.

The asymptotic stability of the control system was ensured by using Lyapunov stability theory to determine the equation that $h(x, t)$ should satisfy. The block diagram of the control system is shown in Fig 6. The problem of designing a state estimator has not been studied. Here, an on-line solution of the boundary layer equations (the plant in Fig. 6) was obtained to determine the parameters such as boundary layer displacement and momentum thickness required to solve for $h(x,T)$.

The simulations were run for a flat plate airfoil. Derivatives in the x-direction were replaced by a second order backward difference approximation, except in the case of backflow, in which case a second order forward difference approximation was used. Sears and Telionis (1975) point out the necessity of reversing the difference scheme in the presence of backflow if the boundary layer equation is to be used to predict the onset of separation. The derivatives in the y-direction were replaced by a fourth order central difference approximation. The integration over time was carried out using a fourth order Adams-Bashforth-Moulton predictor-corrector method.

Firstly, the simulation was run without the control system to determine if the scheme was able to indicate the occurrence of separation. The flow was found to remain fully attached up to an angle of attack of about 8 degrees, after which flow reversal was observed at the trailing edge. The boundary layer equation did not break down until the recirculation region had spread to about a quarter of the chord length. At an angle of attack of 10.3 degrees, the boundary layer equations did not coverage at all. Figure 7 shows the velocity profiles at this angle of attack.

The simulations were then run with the control system. Figure 8 compares the suction velocity distribution when r_d is set adaptively with the suction velocity distributions when r_d is set to content values of 4 and 12 at angles of attack of 8 and 14 degrees. It is seen that at an angle of attack 8 degrees, the suction velocity distribution for three adaptively set r_d is closer to the curve for $r_d=4$. But an angle of attack of 14 degrees, the suction velocity curve moves closer to the curve for $r_d=12$.

4.B Management of Unsteady Separation over Pitching Airfoils Using Controlled Leading-Edge Suction

Principal Investigator: Professor Mukund Acharya
Research Assistants: M. A. Karim & M. Alrefai

Summary of Research Work

The tasks in this part of the grant effort were divided into two phases. In the first phase, experiments were carried out to examine the feasibility of controlling the dynamic-stall vortex (DSV) over the suction surface of a two-dimensional NACA 0012 airfoil, undergoing a 'hold-pitch-hold' motion. Measurements were performed over a range of Reynolds number ($3.0\times10^4 \leq Re_c \leq 1.18\times10^5$) and pitch rate ($0.072 \leq \alpha^+ \leq 0.31$), using leading-edge suction during a prescribed period of the airfoil motion. This strategy to manage the DSV, using controlled leading-edge suction, was developed from a study of the mechanisms responsible for the evolution of the vortex. The results indicate that formation of the DSV can be suppressed by removing an appropriate amount of the reverse-flowing fluid to prevent its accumulation in the near-leading-edge region, thereby preventing lift up of the shear layer. The influence of different parameters such as pitch rate, Reynolds number, suction timing, and suction-slot size and location on the control of the DSV was examined. A scaling was developed for the suction flow rate which provides valuable information about the growth of the reverse-flow region and its dependency on different parameters. Parameter ranges were identified for which complete or partial suppression of the DSV can be achieved.

In the second phase of this work, the effect on the unsteady surface pressures of controlled suction from a spanwise slot, located at 2% chord in the suction surface, was examined in detail for a wide range of pitch rates with a constant velocity ramp motion. The optimum suction required to meet three different control objectives: suppression of the dynamic-stall vortex, delaying detachment of the vortex from the airfoil surface, and maximizing the unsteady lift was determined for different pitch rates and angles of attack. The pressure data were used to develop specifications for the flow state over the airfoil surface that would meet these objectives. Such specifications are necessary for the development of on-line flow management systems. A procedure was also developed to account for variations in suction and motion history.

Background and Objectives

The study of unsteady flow over pitching airfoils has been largely motivated by the need to understand helicopter-blade aerodynamics, and more recently, by interest in aircraft supermaneuverability. In the case of rapidly-pitching airfoils, delay of flow separation on the upper surface results in an additional, transient component to the lift force obtained under static conditions. This increased aerodynamic lift is caused by the formation of a coherent vortical structure, referred to as the dynamic-stall vortex (DSV).

11

A system that is to successfully manage and control this unsteady, separated flow, and thus the aerodynamic behavior of rapidly pitching airfoils, must first be able to monitor and control the DSV.

Depending on the application, the objectives of unsteady, separated flow management may be very different. For example, in helicopter applications the formation of the DSV is undesirable altogether, and the objective of flow control could be to prevent its occurrence in the leading-edge region of rotor blades. In the case of highly maneuverable aircraft, the objective could be to take advantage of the increased dynamic lift by allowing the DSV to form, but to delay detachment and shedding of the DSV from the airfoil suction surface, thereby delaying dynamic stall.

A great deal of effort has been devoted to investigations of this complex flow field, in order to develop an understanding of the physical mechanisms that lead to the formation of the dynamic-stall vortex. Excellent reviews by McCroskey (1982), Gad-el-Hak (1987), and Ericsson and Reding (1987) summarize most of this work. Recent studies at IIT (Metwally (1990), and Acharya and Metwally (1992)) have revealed important information about the evolution of unsteady pressure field and vorticity production over the surface of a two-dimensional airfoil model. Computational work by Visbal (1991), with an emphasis on the initial stage of the formation of the DSV, has also provided useful insight to the problem. As a follow-up to the work by Metwally, Karim (1992) examined the initial stages of the formation of the DSV. His results, and additional experiments reported by Acharya, Karim and Metwally (1995), provide a further understanding of the mechanisms responsible for the formation of the DSV, and the basis for the development of a strategy for its control. There have been a few computational efforts to model flow control over unsteady airfoils using suction or injection. For instance, Yang et al. (1993) described control of the dynamic-stall vortex using modulated suction and injection at the airfoil surface, over an area that varies with the dimensionless pitch rate. Their computational results showed a delay in the onset of dynamic stall, with a corresponding increase in lift and reduction of drag.

This report describes the use of leading-edge suction as one possible strategy for flow control for two-dimensional pitching airfoils. It examines the effectiveness of this approach to suppress the formation of the DSV. The influence of different parameters such as pitch rate, Reynolds number, suction timing and suction-slot size and location on the control of the DSV is also described. The overall goal of work of this nature is to develop control techniques which can be used ultimately for flow management in highly maneuverable aircraft. Such applications involve flow over three-dimensional shapes, high Reynolds number, and lower dimensionless pitch rates. The applicability of leading-edge suction or other control strategies for flow management under these conditions remains to be established. The first phase of this work focused on the effectiveness of leading-edge suction to *suppress* the DSV. Other control objectives, such as alteration, delay in detachment, or enhancement of the DSV are also appropriate, and the second phase examined the effectiveness of leading-edge suction in meeting some of these objectives. This phase was designed to investigate controlled leading-edge suction in more detail, and to assess its applicability as an actuator in a prototype flow-control system that would be useful for flow management strategies with different objectives. Three objectives were examined: suppression of the dynamic-stall vortex, delaying the

detachment of the vortex from the wing (thereby delaying dynamic stall), and optimizing the unsteady lift during a maneuver. In addition, the experiments generated a data base used by Kawthar-Ali and Acharya (1996) for the development and training of a neural-network based controller that is being developed as part of a prototype feedback control system.

Experimental Arrangement

<u>Wind Tunnel</u>   The experiments were conducted in the Andrew Fejer Unsteady Wind Tunnel at IIT's Fluid Dynamics Research Center. This is a closed-circuit, low-speed facility, driven by an axial-vane fan powered by a 40 hp synchronous motor. The wind-tunnel test section is $0.61m \times 0.61m$ in cross section and 3.1 m. in length. Flow velocities up to 40 m/s can be reached by adjusting a magnetic clutch excitation, which controls the fan rotational speed. Screens, honeycombs, and a contraction region upstream of the test section yield a turbulence level of 0.03% at the maximum velocity. Controlled oscillation of a shutter mechanism, mounted at the downstream end of the test section, can produce an unsteady-flow component. A controlled, unsteady motion can also be imparted to a model positioned in the flow.

<u>Airfoil Model</u>   The airfoil model used for this investigation had an NACA 0012 profile, with a chord length of 30 cm., a thickness of 12% chord and a span of 60 cm. The model was made hollow to accommodate tubing for surface-pressure measurements, and to make room for suction and blowing chambers. Details of its design and construction are described by Metwally (1990).

A special feature of the airfoil design provided the ability to withdraw fluid from a spanwise suction slot placed in the near-leading-edge region of the suction surface. A suction chamber with a volume of 50 cm^3 was built into the leading-edge region and connected to the slot. The slot width could be changed by changing the width of an insert. The slot could be located at 2% or 5% of chord from the leading edge. In the present investigation, slot widths of 0.5 mm and 2 mm were used at the two locations. Another feature of the airfoil, not used in the present experiments, provided the ability to introduce a two-dimensional jet into the airfoil wake, through a blowing manifold connected to a spanwise, trailing-edge slot.

The airfoil was mounted in the horizontal mid-plane of the test section, allowing it to pitch about its quarter-chord pivot line. The model was driven by a low-inertia, high-torque, servo-controlled DC motor with an analog servo-amplifier. A Schaevitz R30D Rotary-Variable-Differential Transformer (RVDT) was used to obtained a signal proportional to the airfoil angular position.

<u>Suction System</u>   The airfoil suction chamber was divided into five compartments to achieve uniform suction across the span. These compartments were connected by flexible tubes to a circular distributor located inside the airfoil. The distributor was connected to an evacuated tank located outside the tunnel, through a high-vacuum, direct-acting solenoid valve. The TVP flow meter described in the next section was mounted between

the distributor and the solenoid valve. The solenoid valve was actuated by signals from the minicomputer to enable suction through the leading-edge slot at predetermined angles while the airfoil was in motion. The vacuum tank was evacuated to a specified vacuum level prior to each experimental run, to obtained the desired suction flow rate.

Instrumentation   Smoke-wire flow visualization was used to examine the flow field over the pitching airfoil. A 0.1-mm diameter, nichrome wire was coated with oil droplets and heated electrically, causing the droplets to vaporize, thereby producing uniform streaklines of smoke. The streak lines passing over the model were illuminated and photographed at the appropriate instant.

A vertical smoke wire, placed one chord length upstream of the nose in the central plane of the airfoil, was used to examine the overall flow field. This produced a sheet of streaklines in the central plane, perpendicular to the airfoil span. To examine the near-wall flow structures, another smoke wire was positioned spanwise across the airfoil, at an adjustable height, 0.2 to 1 mm from the airfoil surface. This produced a spanwise sheet of smoke in the near-wall region over the suction surface. A four-bar mechanism mounted on the airfoil model was used to hold the smoke wire to the airfoil, allowing it to remain stationary with respect to the pitching airfoil.

Unsteady pressure measurements were made using a Setra model 239 pressure transducer together with a Scanivalve system. The transducer, tubing etc. together had the required frequency response for these measurements (Metwally, 1990)). The uncertainty in the pressure data reported here was estimated using standard techniques to be $\pm 2.3\%$.

A Trapped-Vortex Pair (TVP) flow meter developed by Mansy and Williams (1989) was used to measure the volumetric flow rate of the fluid withdrawn by suction from the near-leading-edge region. The design of this device results in a jet of fluid that issues into a cavity. A pair of counter-rotating vortices produced in the cavity oscillate as the result of an instability. The oscillation frequency is directly proportional to the volumetric flow rate of the jet. The pressure difference measured between the two sides of the flow-meter axis exhibits the same periodicity as the vortex oscillation. The frequency of this differential-pressure signal is related, through calibration, to the flow rate to be measured. A model DP103 Validyne pressure transducer in combination with a model CD15 Validyne carrier demodulator was used to measure the TVP pressure signal. The uncertainty in the flow rate measurements was estimated to be $\pm 3\%$.

A Masscomp minicomputer was used for all the data acquisition. Data processing was carried out using IBM-compatible PCs and Silicon Graphics INDY workstations.

Parameter ranges   A 'hold-pitch-hold' ramp-up motion of the model at constant velocity was used, covering a range of α^+ between 0.072 and 0.31. The feasibility of leading-edge suction for controlling the dynamic-stall vortex was examined for airfoil pitch-up from 0° to 60° over a range of chord Reynolds numbers from 30,000 to 118,000 using flow visualization and suction flow rate measurements. Slot locations, slot widths, and ranges of other parameters associated with the suction are identified in later sections. The evolution of the unsteady pressure field was studied for a range of pitch rates ($0.01 < \alpha^+ < 0.15$) and suction flow rates ($0 < Q < 24 \times 10^{-3}$). These measurements were

supplemented with a limited amount of flow visualization to examine the state of the flow over the suction surface for selected conditions. The unsteady pressure data were used to obtain ensemble-averaged, chordwise pressure distributions, surface-vorticity-flux distributions, and unsteady lift coefficients. In this phase of the work, unless otherwise stated, a constant suction was applied between 6° and 38° angles of attack. Further details regarding the experimental procedures can be found in Karim (1992) and Alrefai (1995).

Strategy for Control of the DSV

The control strategy was developed from a study of the initial stages in the formation of the DSV that identified the principal mechanisms playing a role in this process. Acharya, Karim and Metwally (1995) provide a detailed description of this process and the evolution of the DSV. A few important results are described in order to develop the basis for the control strategy.

As the airfoil begins its pitching motion, the stagnation point that is initially at the nose of the airfoil moves down the pressure surface, and a strong suction peak develops near the leading edge on the airfoil suction surface. The region between the stagnation point and this leading-edge suction peak experiences a strong, favorable pressure gradient. A concentrated vorticity source located in this region introduces negative, or clockwise, vorticity into the flow. For most of the airfoil motion, this source remains between the airfoil nose and 2% of chord on the pressure side. The fluid containing this clockwise vorticity is confined to a thin shear layer that remains close to the surface initially, and is transported by the shear layer around the nose and over the suction surface. The shear layer has to negotiate an adverse pressure gradient that exists downchord of the suction peak location. As the airfoil continues to pitch up, this adverse pressure gradient increases, slowing down the shear layer, and resulting in an accumulation of vorticity near the leading edge. This is seen by a thickening of the streaklines in Figures 9(a) and (b). The effect of the adverse pressure gradient becomes more severe with increase in the airfoil angle, and eventually builds up to a point where low-momentum fluid close to the surface slows down sufficiently to produce a region of local reverse flow (Figure 9(c)) over the forward portion of the suction surface, between 5% and 10% of the chord. This local, unsteady, reverse flow plays a crucial role in the formation of the dynamic-stall vortex. The reverse-flow layer, which transports fluid particles upchord along the airfoil suction surface, initially remains thin and close to the surface. As the pitch-up continues, the fluid transported by the reverse flow begins to accumulate in the vicinity of the leading edge and forces the shear layer to lift away from the airfoil suction surface (Figure 9(d)). With increasing accumulation of fluid, the shear layer is pushed farther away from the surface, and develops a kink towards the outer flow (Figure 9(e)). As the airfoil angle increases, the region of accumulated reverse-flowing fluid also expands in the chordwise direction (Figure 9(f)). Downstream of this zone of accumulating, reverse-flow fluid, the pressure continues to increase. This results in a further slowing down of the fluid in the shear layer as additional fluid containing clockwise vorticity continues to arrive. At the same time, the shear layer lift-up process continues upchord, as more reverse-flowing fluid accumulates underneath the shear layer.

15

At 26° angle of attack (Figure 9(g)) a recirculating zone of reverse-flow fluid is observed. The accumulation of clockwise vorticity downstream of this zone, caused by the adverse pressure gradient, combines with the outer flow to initiate an instability or a roll-up of the shear layer as seen at 27° angle of attack (Figure 9(h)). This is the first appearance of the dynamic-stall vortex, formed by the roll-up of distributed vorticity in the shear layer into a large-scale vortical structure. The DSV remains compact and stationed over the airfoil surface for a further period, during which it continues to accumulate vorticity from the shear layer. A very abrupt secondary flow feature—a strong, transverse eruption of near-wall fluid, very narrow in streamwise extent and just upstream of the DSV—results in the separation of the DSV from the shear layer. After this stage, the DSV detaches from the surface, grows very rapidly, and convects downstream.

The accumulation of reverse-flowing fluid in the leading-edge region is responsible for the shear-layer lift-up. Subsequent accumulation of vorticity and roll-up of the shear layer causes the formation of the dynamic-stall vortex. This suggests that prevention or delay of the shear-layer lift-up might help control the dynamic-stall vortex formation. To eliminate shear-layer lift-up, we need to prevent accumulation of the reverse-flowing fluid in the leading-edge region. This observation suggested the control strategy for *suppression* of the DSV that we examine in this study: remove the reverse-flowing fluid at the same rate as it arrives in the leading-edge region, through a spanwise slot placed appropriately in the suction surface. Other objectives, such as delaying the detachment of a formed DSV, can be met by changing the rate at which this fluid is removed.

Information on the angle at which lift-up occurs is important for the control experiments. The variation of this angle with the dimensionless pitch rate, plotted in Figure 10, shows that events in the evolution of the DSV are delayed to higher angles as the pitch rate increases.

Evaluation of Control Strategy

The suction concept described above was tested in experiments, in which fluid was withdrawn through a suction slot at a wide range of rates. Figure 11 compares the result of such an experiment at one suction flow rate, to the flow field without suction control. These photographs show a view of 67% of the suction surface and were taken at four different angles of attack, while the airfoil was pitching from 0° to 45° with $\alpha^+=0.15$. The spanwise smoke wire was positioned at the nose, 1 mm from the surface. The dimensionless suction flow rate Q_{nd} for the controlled case was 0.0127 and suction was initiated at 6° angle of attack during pitch up of the airfoil, through a spanwise slot at 2% chord. As discussed in a later section, this flow rate was found to be the optimum suction rate for this flow condition and 35° angle of attack. The pictures with suction control show that the shear layer remains close to the surface; the negative vorticity produced in the leading-edge region convects downstream along the suction surface of the airfoil. At the high angles of attack, the smoke streak becomes thicker and transition to a turbulent state is observed. On the other hand, in the natural cases with no suction control, a fully-grown dynamic-stall vortex is seen over the suction surface of the airfoil.

Based on the experimental results that follow, it is argued that optimum suction removes the necessary amount of near-wall fluid through the suction slot to prevent accumulation of reverse-flowing fluid. Shear-layer lift-up no longer occurs near the leading edge, thereby preventing formation of the DSV. It is this mechanism, rather than removal of fluid from the shear layer that flows downchord, that suppresses the dynamic-stall vortex. The shear-layer fluid is not removed; its agglomeration and roll-up into a vortex is prevented.

The results presented in following sections show that formation of the DSV, the shedding of which culminates in dynamic stall, can be suppressed for a range of flow parameters by removing a small amount of fluid from the near-wall region. On the basis of the experimental evidence, it is reasoned that this suction removes fluid that would otherwise accumulate in the leading-edge region, resulting in lift-up of the shear layer. The level of control required for either complete or partial suppression of the DSV is established by changing the rate at which fluid is removed from the leading-edge region.

The control strategy is based on the amount of fluid removed from the near-wall region rather than the suction pressure level or velocity at the suction slot. Other parameters, such as suction activation time, deactivation time, and slot location also affect the control process. The influence of these parameters, as well as controllability, and limitations with increase in chord Reynolds number and angle of attack are addressed in the following sections. Some scaling properties are also discussed.

Experimental Determination of the Optimal Flow Rate

The effect of varying the suction flow rate over two orders of magnitude was examined for the conditions of Figure 11. Suction was activated at an angle of 6°, and the set of flow-visualization records shown in Figure 12 was obtained at an angle of 35° during the pitch-up. For values of the dimensionless suction flow rate from 0.064 to 0.0123, there is no significant difference in the flow field over the airfoil suction surface. Below a rate of 0.0123, ability to suppress the DSV is progressively degraded. For a suction of 0.0101, the development of a vortex is seen near the leading-edge region. At 0.000718, the last record in the figure, the flow over the suction surface resembles the natural case (without suction control).

If the earlier description of the physical processes is accurate, removing fluid by suction at a rate higher than that needed to prevent accumulation of reverse-flowing fluid should not produce any additional improvement in the flow state. This should result only in removal of some additional fluid with negative vorticity from the shear layer. Results for suction rates larger than 0.0127 support this argument. Suction at a rate lower than the accumulation rate of the reverse-flowing fluid should result in some accumulation in the leading-edge region, and therefore only a partial suppression of the DSV. In addition, partial removal of the reverse-flowing fluid should slow down the rate of accumulation, and lead to a delay in the vortex formation with a smaller vortex compared to the natural state at the same angle of attack. Results for suction rates smaller than 0.0127 validate this reasoning. While the accumulation rate is not measured directly, it is logical to argue that for the experimental conditions described above, a suction rate of 0.0127 removes

reverse-flowing fluid at the accumulation rate, and that for each set of flow conditions, there must be an optimum suction flow rate which prevents any accumulation of reverse-flowing fluid, thereby suppressing the vortex completely. The optimum conditions must be defined for a specific control objective, such as complete suppression of the vortex. Different objectives, such as partial control or delaying the detachment of a formed DSV, would result in different optimum specifications. The scaling properties of the optimum suction flow rate for complete suppression are described next.

Scaling of the Suction Flow Rate

Complete suppression of the DSV requires that reverse-flowing fluid be removed from the leading-edge region at a specific rate. An examination of the scaling that governs this suction flow rate provides a way to validate the concept as well as insight to the growth of the reverse-flow region and its dependency on different parameters. Dimensional analysis, with the variables free-stream velocity U_∞, a characteristic length, taken to be the chord length c, the angular velocity of the airfoil $\dot{\alpha}$, suction flow rate $\dot{Q}_s$, fluid density ρ and viscosity μ results in three dimensionless groups: $\dot{Q}_s/U_\infty c^2$, $\dot{\alpha}c/U_\infty$, and $U_\infty c/\nu$. The last two are the dimensionless pitch rate α^+, and chord Reynolds number Re_c, respectively. The control strategy calls for a balance between the rate of suction $\dot{Q}_s$ and the reverse-flow accumulation rate $\dot{Q}_{rf}$. A simplified model of the near-wall process is used to obtain an expression for the latter and relate the two rates. The dimensionless pitch rate $\dot{\alpha}c/U_\infty$ is the ratio between a convective time scale c/U_∞ and the time scale of the airfoil motion $1/\dot{\alpha}$. For a fixed chord length c and angular velocity $\dot{\alpha}$, the convection time scale decreases relative to the airfoil motion time scale as U_∞ increases, resulting in an increase in the accumulation rate. The accumulation rate is thus inversely proportional to the convective time scale. The rate of growth of the reverse-flow (viscous) region, on the other hand, is proportional to the viscous length scale ν/U_p and convective time scale (c/U_∞). The ratio of these two scales provides a measure of the accumulation rate U_{rf} of reverse-flowing fluid. The volumetric rate $\dot{Q}_{rf}$ is thus proportional to $U_\infty(\nu/\dot{\alpha})$ $[U_p\sim c\dot{\alpha}$ and $\dot{Q}_{rf}\sim U_{rf}c^2]$. Comparison of the two rates $\dot{Q}_{rf}$ and $\dot{Q}_s$ yields the appropriate scaling. The control strategy requires that the ratio $\dot{Q}_s/\dot{Q}_{rf}$ remain constant for a given dimensionless pitch rate (i.e. a fixed ratio between the convective time scale and the time scale of airfoil motion) and angle of attack. The required suction flow rate for a particular value of α^+ and angle of attack is therefore given by

$$(\dot{Q}_s/U_\infty)(\dot{\alpha}/\nu) = \text{constant}$$
$$\text{or, } (\dot{Q}_s/U_\infty c^2)(\dot{\alpha}c/U_\infty)(U_\infty c/\nu) = \text{constant}$$
$$\text{or, } (\dot{Q}_s/U_\infty c^2)\alpha^+ Re_c = \text{constant}$$

which is the product of the three dimensionless groups obtained by dimensional analysis. The constant needs to be determined by experiment for different pitch rates, Reynolds number and angle of attack.

Effect of Free Stream-Velocity and Pitch Rate at Different Angles of Attack

Experiments were carried out to examine the influence of free-stream velocity and pitch rate on the control of the dynamic-stall vortex at different angles of attack. A 0.5-mm wide slot, located at 2% chord was used. The objective of control was complete suppression of the dynamic-stall vortex. The minimum suction flow rate required to achieve this control was chosen to be the optimum rate. For all the experiments described, suction was activated at 6° angle of attack during pitch-up of the airfoil.

Figure 13 shows that suction with Q_{nd}=0.0127 provides control at 35°, for α^+=.15 over a Reynolds number range of 30,000 to 118,000. Note that for a fixed value of α^+, the product $(\dot{Q}_s/U_\infty c^2)Re_c$ is independent of U_∞. The data of Figure 13 substantiate this. Data at $\alpha^+ = 0.10$ for the same conditions also confirm the scaling argument and model for reverse-flow accumulation, with a higher value (0.0429) for the suction flow rate. Figure 14 shows the results at 35° for $\alpha^+ = 0.072$ and a Reynolds number range of 30,000 to 88,000. In this case, the dynamic-stall vortex was completely suppressed by removing fluid at a rate of 0.109 for a range of Reynolds number 30,000 to 50,000. For the same removal rate, however, the flow field over the airfoil suction surface shows a degraded effect of suction as the free-stream velocity increases beyond this value. This effect is first seen at a Reynolds number of 53,000, where the dynamic-stall vortex starts developing near the airfoil leading edge. With increase in free-stream velocity, the effect grows, and the ability to suppress the DSV decreases. At a Reynolds number of 88,000, the DSV extends up to trailing edge of the airfoil.

The behavior at lower pitch rates is related to early break down of the shear layer (Karim (1992)). At lower pitch rates, the flow is closer to quasi steady in nature. With the increase in the free-stream velocity beyond a critical value, transition to turbulence in the shear layer alters the flow behavior. Since the dynamic-stall vortex is weaker at lower pitch rates, transition and turbulence in the shear layer affect the flow development at comparatively smaller values of Reynolds number. On the other hand, at higher pitch rates, unsteady effects are more dominant, the dynamic-stall vortex is stronger, and the effects of transition and turbulence in the shear layer on the development of the DSV are important only at relatively higher Reynolds numbers. Once a break down of the shear layer occurs, the reverse-flow region becomes substantially thicker, and a larger amount of fluid needs to be removed by suction to achieve complete suppression of the DSV. This amount then needs to be increased as the free-stream velocity increases.

Flow-visualization records and corresponding suction flow rate measurements reveal that as long as the unsteady flow field is not influenced by transition and turbulence in the shear layer, control of the DSV is independent of free-stream velocity (or Reynolds number). The magnitude of the favorable, streamwise pressure gradient on the suction surface increases with pitch rate, and has a highly stabilizing effect on the boundary layer. This causes the shear layer and reverse-flow regions to remain thin, and moves transition to higher Reynolds number. Thus, as the unsteady effect increases, the rate of accumulation of reverse-flowing fluid for a given pitch rate is the same for a wider range of Reynolds number.

In summary, the pitch rate has the primary influence on the unsteady flow behavior, and dictates the suction flow rate needed to achieve optimal control at a given angle of attack. As long as the reverse-flow region remains thin, the flow can be controlled by removing a small amount of fluid to prevent accumulation in the near-leading-edge region, and the amount of fluid removed is independent of the outer flow velocity. As the pitch rate decreases, the Reynolds number at which transition to turbulence occurs in the shear layer decreases, the flow structure is altered, and the height of the reverse-flow region increases at the same angle of attack. Flow control now depends not only on the pitch rate but also on the outer velocity (or Reynolds number).

Data were acquired for a few different angles during the pitch up of the airfoil. The flow rates needed for complete suppression of the vortex are plotted against the dimensionless pitch rates in Figure 15. This representation of the data is useful to study the effect of pitch rate on the control of the dynamic-stall vortex, and to provide evidence for the validity of the simplified model of the accumulation process. The suction flow rate is normalized as $(\dot{Q}_s/U_\infty c^2)\alpha^+ Re_c$, using the scaling developed with the model. For a given angle of attack (e.g. 35°) this product remains constant for a range of dimensionless pitch rates, as predicted by the model. The extent of this range of α^+ increases as the angle of attack decreases. As the pitch rate decreases for a given angle of attack, the model eventually breaks down, and the amount of suction required starts to increase. At some point, the volumetric rate limit of the suction apparatus used in the experiments is reached. Beyond this, only partial suppression of the DSV is possible, i.e., the control objective is not met. The range of pitch rates where partial suppression was obtained is shown by a broken line on the plot for each angle of attack. It is thus possible to define a zone of complete suppression in this parameter space (shown in the figure by a broken line). An increased suction flow rate is required to achieve optimal control as the pitch rate decreases and the airfoil angle of attack increases.

The suction requirements are shown plotted versus angle of attack in Figure 16 for different dimensionless pitch rates. As the angle of attack decreases and pitch rate increases, the suction required for control decreases. Following a line of constant α^+, it is possible to determine the suction requirements during a constant-pitch-rate maneuver. To meet the control objective (complete suppression), the suction flow rate needs to be increased as the angle of attack increases. A broken line once again divides the regions of complete and partial suppression. As the pitch rate increases, complete suppression can be achieved at higher angle of attack for the same suction flow rate. The region above the broken line shows the domain where the DSV can only be partially suppressed, and the effectiveness of control degrades as the Reynolds number increases.

The plots in Figure 17 show the variation of suction flow rate with Reynolds number at two fixed angles of attack for different pitch rates. The range of the Reynolds number where suction control is independent of free-stream velocity (Reynolds number) becomes smaller as the pitch rate decreases or angle of attack increases.

The experiments thus establish a range of applicability for the proposed scaling, verify the validity of a simple model for the accumulation of reverse-flow fluid, and provide the ability to predict the amount of suction required for complete suppression of the DSV over a domain of the primary parameters that influence the process.

Effect of Suction Activation and Deactivation Time

To examine the influence of suction activation time, α_{on}, on the control process, flow-visualization records were obtained at 35° angle of attack, while airfoil was pitching from 0° to 40°, for a range of α_{on}, with α_{off} fixed at 38°. The rate of suction was fixed at the optimum value of 0.0127 for the flow conditions ($\alpha^+=0.15$ and $\alpha=35°$). The flow development over the airfoil suction surface for α_{on} values of 6°, 10°, 15°, 20°, 25°, and 30° is compared with the natural case (no suction) in Figure 10. Suction can be used to suppress the dynamic-stall vortex completely if activated before the airfoil reaches 20° (i.e., $\alpha_{on} < 20°$). Note that shear layer lift-up occurs at about 18° for this pitch rate (Figure 10).

The effect of suction deactivation time on the flow control was examined by fixing α_{on} at 6° and varying α_{off} over a range for the same flow conditions. The results indicate that termination of suction control before the angle of attack at which control is needed, results in incomplete suppression the vortex. This behavior of the unsteady flow suggests that once the suction is initiated, it must be applied continuously, as long as the control is desired. Terminating suction control results in the immediate formation of the dynamic-stall vortex.

Complete suppression of the dynamic-stall vortex therefore requires that two conditions on the suction timing be satisfied: (i) *suction activation should be prior to the angle at which the shear layer lift up occurs* and (ii) *suction control should be continued as long as control is desired.* However, the selection of the suction flow rate depends on the maximum angle at which the flow control is desired and on the rate at which the airfoil is pitching.

Effect of Width and Position of the Suction Slot

The suction slot width was varied by a factor of four and the slot location changed from 2% to 5% chord. Figure 19 shows two visualizations of the flow at 35° angle of attack for $Re_c= 30,000$, $\alpha^+= 0.15$ and slot widths of 0.5 and 2 mm respectively. In both cases the suction slot was located at 2% of the airfoil chord. These pictures show no significant difference in the flow field. All the measurements made indicate that the volume rate of suction, not the suction velocity, is the important control parameter.

Experiments were conducted for slot locations between 2% and 5% of airfoil chord for the same flow conditions as above. No significant differences were observed over this range of slot location. It is argued that the slot location is not critical, as long as it is in a region where reverse-flowing fluid can be removed.

Magnitude of Suction

In order to assess the control technique, some measure of the energy expended in its implementation is needed. The dimensionless suction flow rate Q_{nd} compares the

21

suction flow rate $\dot{Q}_s$ with a representative flux of oncoming fluid, $U_\infty c^2$, and provides a measure to assess the amount of fluid removed. For complete suppression of the DSV over the range of pitch rates, chord Reynolds numbers and angles of attack examined, the ratio $(\dot{Q}_s/U_\infty c^2)$ was of the order of 0.01. Other control strategies suggested have been suggested, with similar results. Visbal's computations showed that suction with a velocity 4% of the free-stream velocity, applied uniformly between the nose and 15% of chord, could suppress the DSV at 36° angle of attack at a dimensionless pitch rate of 0.6. When the suction application was concentrated in a region between the nose and 2% of chord, the suction velocity required to suppress the vortex increased to 10% of the free-stream velocity. Yang et al. describe control of the DSV using modulated suction and injection at the airfoil surface, over an area that varies with the dimensionless pitch rate. Their computational results show a delay in the onset of dynamic stall, with a corresponding increase in lift and reduction of drag.

Characteristic Length Scale

It is important to note that the events influencing the formation and control of the DSV occur in the leading-edge region of the airfoil, and that the mechanisms described can be strongly influenced by the airfoil geometry in this region. A length scale characteristic of this region, such as leading-edge radius, is therefore in all probability the appropriate scale to use, rather than the airfoil chord, when describing the Reynolds-number effects. However, since a single airfoil model was used in these studies, the two scales are related by a constant factor, allowing the use of chord Reynolds number in interpreting the results.

Effect of Suction on the Surface-Pressure Distributions

The effect of leading-edge suction on the evolution of the unsteady surface pressures and flow development over the suction surface was examined by varying the suction flow rate systematically while keeping other parameters constant. Figs. 20, 21 and 22 show the variation of the chordwise surface-pressure coefficient C_p over the airfoil for three angles of attack: 26°, 29°, and 35°. Locations along the suction and pressure surfaces are designated by positive and negative values of x/c respectively. In each case, the dimensionless pitch rate $\alpha^+ = 0.15$, the chord Reynolds number was 1.1×10^5, and pressure distributions are shown for ten different flow rates Q varying from 0 (the natural case with no suction applied) to 0.01364. Flow visualization showed that at $\alpha^+ = 0.15$, with no suction applied, the dynamic-stall vortex was well formed at an angle of attack of 26°, had begun to move across the suction surface by 29°, and had detached and started to convect off the airfoil by 35°. The pressure distributions at these angles for Q = 0 in figs. 20, 21, and 22 are consistent with this sequence of flow development. The presence and extent of the dynamic-stall vortex over the suction surface is indicated in the pressure distributions by a broad suction peak, known as the dynamic-stall vortex peak (DSVP). It first appears between 5% and 15% of chord, the location at which the vortex forms, and its minimum is indicative of the vortex center. As the vortex grows, detaches from the airfoil surface, and convects off the airfoil, a corresponding broadening and movement of the DSVP is observed. This movement of the vortex with increase in angle

of attack is clearly reflected in the behavior of the DSVP for Q = 0 in figs. 20-22. The suction-surface pressure distribution usually contains another peak, referred to as the leading-edge suction peak (LESP). As seen in the figures, this peak occurs over a very narrow spatial region of the surface between 0% and 3% chord as the airfoil pitches up, and is associated with the acceleration of the flow around the leading edge.

Application of suction delays or inhibits formation of the dynamic-stall vortex. The effect of this suction on the flow development and the associated surface-pressure distribution varies with the angle of attack, as one would expect from the results of the first phase. At each of the angles of attack shown in figures 20-22, similar trends were observed with gradual increase in the magnitude of Q. At first, the DSVP becomes more compact and remains further upchord. With further increase in Q, there comes a point when the DSVP is no longer seen. Increase in Q beyond this value does not significantly affect the pressure distribution, other than to increase the magnitude of the LESP. An examination of the data shown in figures 20-22 in conjunction with flow-visualization photographs revealed that the minimum value of Q required to suppress the dynamic-stall vortex completely at an angle of attack of 26° was 0.0017, while the values were 0.0028 and 0.0074 at 29° and 35° respectively. The pressure data also showed that in each of these cases, suction at rates higher than the values specified resulted only in increasing the suction peak, while suction at levels lower than those specified allowed the vortex to form to varying extents, depending on the magnitude of the parameters.

Data obtained at other angles of attack at this pitch rate, as well as measurements at other pitch rates exhibited very similar trends, except that the values of Q at which different states were observed varied with α and α^+. These results are discussed in detail by Alrefai. The observations can be summarized as follows: at a given pitch rate and angle of attack, complete suppression of the dynamic-stall vortex could be achieved by increasing the suction rate until an optimum suction rate (Q_{opt}) was reached. Any further increase in the suction rate had no effect on the flow field or pressure distribution, except to increase the magnitude of the LESP. Suction at rates less than optimum resulted in the presence of a dynamic-stall vortex whose size and location varied with the suction applied, or in a separated flow field established after the vortex had convected off the airfoil.

The minimum suction rate necessary to suppress the dynamic-stall vortex, Q_{opt}, decreased as α^+ increased or α decreased. The criterion described above was used to determine Q_{opt} for the five dimensionless pitch rates examined, over the full range of angle of attack for which the vortex was completely suppressed. The result is shown in fig. 23. It should be noted that the $Q = 24 \times 10^{-3}$ was the upper limit of the suction system.

It is evident from the pressure distributions of figs. 20-22 that the optimum suction needed to delay detachment of the vortex, or to maximize the lift at any angle of attack is different from that required to suppress the dynamic-stall vortex completely. The optimum suction required for these control objectives were determined in a similar fashion.

Specification of Flow State

A central issue in active control of such flows is the identification of flow state. To be effective for this purpose, the variable to be monitored must be measurable with ease; for instance, measurements to obtain velocity-field information might prove difficult or expensive to incorporate in a practical feedback control system.

The variable that presents the most practical alternative for flow-state identification is surface pressure. The signatures of the desired flow states discussed above are discernible in the suction-surface pressure distributions, *allowing use of the latter for identification of the flow state*. Data such as those shown in figs. 20-22 demonstrated that an examination of comparative pressure levels and pressure gradients from measurements at a few discrete locations in the leading-edge region of the suction surface between 0% and 10% chord, can be used to indicate different states of the flow over the suction surface; e.g., a flow state where the dynamic-stall vortex is suppressed, or a state where the vortex is still bound to the airfoil surface.

Suppression of the Dynamic Stall Vortex   An examination of the surface-pressure data showed that the pressure distribution in the region between 4% and 15% chord provided an excellent indication of the flow states corresponding to a fully suppressed vortex (achieved when $\geq Q_{opt}$). A typical example is shown in fig. 24, where the pressure distributions with $Q = Q_{opt}$ are shown for the five pitch rates at an angle of attack of 20°. Beyond $x/c = 0.16$, the data collapsed reasonably well. Between 0% and 4% of chord, a systematic increase in the LESP magnitude was seen with decreasing pitch rate. In the region between 4% and 15%, trends in the pressure variations were very similar, with a small but detectable increase in the magnitude of C_p as α^+ decreased. Similar results were obtained at other angles of attack where suction could be used to suppress the vortex, with a small, but systematic increase in the magnitude of C_p in this region with increase in the angle of attack. The nature of variations in the surface pressure over this region with a suppressed vortex was clearly distinguishable from trends in the pressure for all other states. This observation enabled the development of a specification for the *required* pressure field in the region between 4% and 15% of chord that would *ensure* a flow state over the suction surface corresponding to a suppressed dynamic-stall vortex.

Delaying Dynamic-Stall Vortex Detachment   To develop a criterion that describes the state of flow with an attached dynamic-stall vortex, the unsteady pressure distributions were examined together with the surface vorticity flux, S, computed using spline fits to the pressure data. The range of interest was restricted to the first 15% of the chord. The results are summarized with the aid of fig. 25. The variation of the dimensionless vorticity flux, S^+ is shown in fig. 25(a) for $\alpha^+ = 0.01$ and an angle of attack of 12°. Two prominent features were observed for all the suction rates used: a positive peak at 2% chord and a negative peak at about 4% chord. The corresponding pressure distributions showed that the vortex was still attached to the airfoil surface, even for the natural case (no suction). At an angle of attack of 18°, the pressure data showed that the vortex was suppressed for suction at rates 5.68×10^{-3}, 11.37×10^{-3} and 23.87×10^{-3}, while at

2.84×10^{-3} the vortex had formed and remained attached to the surface, and for $Q = 0$ the vortex had detached from the airfoil. The corresponding vorticity flux variations in fig. 25(b) show positive peaks at 2% and negative peaks between 4% and 5% for all cases except $Q = 0$. An examination of plots such as these for all the pitch rates and angles of attack showed a positive peak with an S^+ magnitude of 20 or greater at 2% chord and a negative peak between 4% and 5% chord *only* for flow states with either a suppressed or attached vortex.

This observation can be used as a criterion to identify a flow state where the vortex has not detached from the airfoil surface. In addition, the optimum suction flow rate to delay detachment of the dynamic-stall vortex may be defined as the minimum value of Q which satisfies the above criterion.

Optimizing the Unsteady Lift   The pressure data acquired at different suction and pitch rates were integrated to determine the lift-coefficient variation with angle of attack. Fig. 26 shows these variations as a function of angle of attack for the natural case (no suction) for the five pitch rates investigated. The steady state C_l - α curve is also shown for comparison. In all cases, the lift coefficient increased beyond the static-stall value, reaching a peak value that increased with pitch rate. Beyond this peak, the lift dropped because of the onset of dynamic stall.

The effect of suction on the lift coefficient for $\alpha^+ = 0.15$ is shown in fig. 27(a). Increase in suction resulted in a systematic shift of the peak value of C_l to higher angles of attack, from 28° with $Q = 0$, to 38° for $Q = 5.68 \times 10^{-3}$. Continuation of this trend is highly likely, but could not be confirmed because suction was turned off at 38°. The effect of suction rate on the magnitude of C_l was interesting. When the angle of attack was lower than the value for the onset of dynamic stall with no suction, the lift decreased with increasing suction, since the effect of suction was either to reduce the size of the vortex, or to suppress it partially or completely. At angles of attack greater than this value, the lift first increased with suction rate, and beyond a certain point decreased as suction was increased further. In this case, suction initially served to delay detachment of the vortex, thereby providing increased lift. Beyond a certain magnitude of suction however, the suction started to affect the size of the vortex, and the lift decreased. An examination of the corresponding pressure distributions supported this explanation. The amount of suction needed to maximize the lift gradually increased with the angle of attack. With decrease in pitch rate, the effects were similar; however, both the maximum values of C_l, and the angles of attack at which these occurred decreased as the pitch rate decreased. The behavior at $\alpha^+ = 0.018$ is shown in fig. 27(b). Results for the other pitch rates are discussed by Alrefai.

Comparison of Suction Requirements   The minimum suction (i.e., Q_{opt}) required at any pitch rate and angle of attack varied with the objective. Not surprisingly, Q_{opt} was the largest for complete vortex suppression. The magnitude needed to maximize the lift was smaller, while that required to delay dynamic-stall vortex detachment was the smallest. Fig. 28 shows the surface-pressure distributions and the corresponding magnitudes of Q_{opt} for the three objectives for $\alpha^+ = 0.15$ and $\alpha = 35°$. The variation of

Q_{opt} with the angle of attack for each objective at a constant pitch rate of 0.15 is shown in fig. 29. For each objective, Q_{opt} increased with angle of attack and decreased with pitch rate.

<u>Effect of Motion and Suction History</u>   In these experiments, a constant-velocity ramp motion from 0° to 45° was used, together with a constant suction flow rate applied between angles of attack of 6° and 38° during pitch up. An important assumption was made interpreting the results: for a given angle of attack α, and pitch rate α^+, the net influence of the past motion and suction history is to determine *the flow state* at that (α, α^+), as measured by the pressure distribution. The results of the present experiments should therefore be valid for *any* prior motion of the airfoil and suction history up to that instant, provided that the surface-pressure distribution at that value of (α, α^+) can be matched to one from the present experiments at the same (α, α^+), even if the instantaneous suction flow rate is different. In fact, the likelihood is that the suction flow rates *would* generally be different. If this condition is met, the pressure data generated in the present experiment may be used to determine the *change* ΔQ in suction required to *change* the flow state at that (α, α^+), as measured by the pressure distribution, from one condition to another.

In order to assess the validity of this assumption, experiments were carried out to modify the motion history by the use of a double-ramp motion in which the airfoil velocity was changed from one constant value to another at an intermediate angle during pitch up. Two motion profiles: a slow-fast combination and a fast-slow combination were used. The suction flow rate used through the entire motion was kept constant at a value Q_i. The pressure distribution over the airfoil surface at a selected angle of attack during the second phase of the dual-ramp motion was compared with the pressure distributions at the same pitch rate and angle of attack, but with a single-ramp motion, obtained in the earlier experiments for a range of suction flow rates. The suction flow rate Q_f with the single-ramp motion for which the pressure distribution matched that obtained in the dual-ramp experiment was determined. Based on the assumption described earlier, it was then argued that the *change* $\Delta Q = (Q_{opt} - Q_f)$, required at ($\alpha$, α^+) to suppress the vortex for the simple-ramp motion would be the same for the dual-ramp case as well, i.e., the required suction to suppress the vortex at that (α, α^+) would be $Q_i + (Q_{opt} - Q_f)$. The same procedure was repeated at other angles of attack.

Figure 30(a) shows the pressure distribution at α =23° for a dual-ramp motion with α^+ = 0.036 from 0° to 20°, α^+ = 0.15 from 20° to 45°, and Q_i = 5.68x10^{-3}. The pressure distributions at that angle for a single-ramp motion with α^+ = 0.15 corresponding to Q_{opt} = 2.84x10^{-3} and Q_f = 1.71x10^{-3} are also shown. The dual-ramp pressure distribution for Q_i is very similar to the single-ramp distribution at Q_f = 1.71x10^{-3}. The suggested increase in the flow rate to suppress the vortex for the dual-ramp motion is thus ΔQ = 1.13x10^{-3} m^3/hr. A suction flow rate of 6.82x10^{-3} resulted in the same pressure distribution as that at Q_{opt} for the single-ramp motion. Fig. 30(b) shows another example with the same motion at α = 26°. Here Q_{opt} was 3.41x10^{-3} for the single-ramp motion, and ΔQ was 1.14x10^{-3}.

Similar results were obtained for a fast-slow dual-ramp motion with $\alpha^+ = 0.15$ from $0°$ to $20°$ and $\alpha^+ = 0.036$ from $20°$ to $45°$, when compared with single-ramp results at $\alpha^+ = 0.036$. These comparisons validate the assumption stated earlier: the effects of previous history in the airfoil motion and suction flow rate manifest themselves in the state of the flow at any (α, α^+), as reflected in the pressure distribution. If used properly, the results of the present single-ramp motion experiments can be used for other motion and suction histories to determine the change in suction necessary to alter the flow state as desired at that angle of attack. It should be noted that experiments with more general motions, including combinations of pitch-up and pitch-down segments are necessary to ensure that this argument applies for any general motion of the airfoil.

4.C Closed-Loop Control of Forebody Flow Vortices and Side Forces Using Suction, Blowing and Unsteady Bleed

Principal Investigator: Professor David R. Williams
Research Assistant: John E. Bernhardt

The experimental results relating to the forebody models are presented in this section. The results focus on several important areas of forebody flow behavior including the instability characteristics of the forebody wake and the behavior of the asymmetric tip vortices. The experimental data clearly shows the effect of Reynolds number on the vortex asymmetry. Additional results concentrate on the different vortex control techniques and the control systems designed for the various models. The results for the static model are presented first, followed by the pitching cases.

Background and Objective

<u>Forebody Vortex Behavior</u>   The vortex behavior was investigated using the forebody model with the conical nose. A preliminary set of pressure measurements was taken with the model in order to verify the presence of the three basic flow regimes. For angles of attack from $0°$ to $30°$, the flow was symmetric and the sectional side-force coefficient was negligible. For α between $30°$ and $60°$, the sectional side-force coefficient was large due to the system of steady asymmetric vortices that separated near the model tip. Above $60°$ angle of attack, unsteady vortex shedding similar to Karman vortex shedding began on the lower portion of the cylinder. Further increases in the angle of attack moved the shedding region closer to the tip. The time-averaged value of C_y was again negligible.

The results for this section focus on two angles of attack. Initial experiments with the forebody model indicated that significant differences in vortex behavior occurred between $\alpha = 45°$ and $55°$. In this angle of attack range, Zilliac et al. (1990) demonstrated that the flow became bistable. Consequently, the model was positioned at these two angles of attack for the experiments.

<u>Sectional Side-Force Measurements</u>   The effect of forcing on the sectional side-force coefficient is shown in Figure 31(a) for $\alpha = 45^{\circ}$ and $Re = 6300$. The Reynolds number calculation was based on the cylinder diameter and the freestream velocity. As illustrated by the filled circle in the figure, the natural asymmetry of the tip vortices produced a C_y value of -0.51. When the unsteady bleed was activated on the same side as the primary vortex ($C_{\mu} > 0$), the sectional side-force coefficient initially increased. The side-force coefficient continued to increase as the forcing level was increased until it saturated at a value of 0.60. The corresponding bleed coefficient at the saturation point was 0.004. It was possible to achieve intermediate values of the side-force coefficient due to the continuous variation in the vortex configuration. Any additional increases in the forcing amplitude beyond the saturation point did not change the vortex configuration, but caused a slight reduction in the side-force coefficient.

Activation of the control on the side opposite to the primary vortex ($C_{\mu} < 0$) resulted in a decrease of C_y to -0.61 at $C_{\mu} = -0.003$. Further increases in the forcing amplitude caused a small reduction in the magnitude of C_y from the saturated value. It is important to note that the vortex system always returned to the natural state when the control was turned off on either side.

The forebody vortices displayed a fundamentally different behavior at $\alpha = 55^{\circ}$. Figure 31(b) shows the effect of forcing on the sectional side-force coefficient for this angle of attack. The value of the side-force coefficient for the natural state of the vortex system was 0.49, which corresponds to the upper filled symbol in the figure. For positive bleed coefficients, a transition point occurred at $C_{\mu} = 0.007$ where the vortices switched rapidly to the mirror image of their original configuration with $C_y = -0.55$. No intermediate states could be attained with the forcing system. Increasing the forcing amplitude beyond the transition point did not cause any major changes in the vortex configuration.   Most importantly, the vortices did not return to their original configuration when the unsteady bleed was turned off. Instead, the side-force coefficient remained negative with a value equal to -0.47 (lower filled symbol). This behavior of the vortex system is clear evidence of bistable states, where bistable is defined as the existence of two stable states of the flow in the absence of external perturbations.

A similar response of the vortex system was found for negative bleed coefficients. In this case, the vortex configuration switched at a transition bleed coefficient of -0.005. Once again, no intermediate values of C_y were achievable with the forcing system. Turning off the unsteady bleed recovered the original state of the flow field.   The combined positive and negative forcing form a hysteresis loop in the C_y versus C_{μ} plot. The path around the hysteresis loop is shown by the arrows in Figure 31(b).

<u>Pressure Distributions, Velocity Maps, and Flow Visualization</u>   The sectional side-force measurements do not provide sufficient evidence that the entire vortex system is responding to the unsteady bleed control. In addition, a correlation must be established between the side-force coefficient and the configuration of the vortex system. With these

ideas in mind, pressure distributions and velocity maps have been acquired to give more detailed information about the effects of the control technique. Flow visualization studies were carried out in order to supplement the pressure and velocity data.

Three different configurations of the vortex system were studied in detail at $\alpha = 45^\circ$. These vortex configurations included the natural case (yaw right), the symmetric case (zero yaw), and the antisymmetric case (yaw left). The data for the natural vortex configuration is displayed in Figure 32 where $C_y = -0.47$. Figure 32(a) consists of flow visualization photographs of the forebody wake viewed from two distinct perspectives. The strobe light visualizations show side views of the forebody wake. The flow field on the side of the model closest to the camera is visualized in the "near side" photograph. The "far side" photograph is a visualization of the flow field on the side of the model farthest from the camera. The "sides" of the model are also labeled in the laser sheet visualization. The laser sheet visualization presents an axial view of the forebody wake. The laser sheet intersected the model axis at a Z/D of 3.04, which corresponded to the axial location of the pressure taps. The flow visualization photographs for the natural case clearly show that the vortices were asymmetric as suggested by the nonzero value of C_y. The primary vortex on the far side of the model separated close to the tip. The weaker vortex on the near side did not separate until $Z/D = 5.5$.

The pressure distribution and velocity map for the natural vortex configuration are presented in Figure 32(b) and Figure 32(c) respectively. For the pressure distribution, the azimuthal angle θ is measured from the forward stagnation point. The value of θ at the forward stagnation point is 0° and increases to 180° at the back of the cylinder. The azimuthal angle is positive for both the near and far sides, so that the pressure distributions on the two sides may be easily compared. The pressure data shows that the higher pressures occurred on the far side of the model (filled circles). The high pressure region created a side force that acted to the right as indicated by the arrow in Figure 32(a). The side force would yaw the model to the right if it was not rigidly attached to the wind tunnel mounting sting. The u-component velocity contours in Figure 32(c) clearly show the high-speed flow associated with the stronger primary vortex located on the far side of the model. The far side of the model is represented by negative Y/D values in the figure.

The results for the symmetric case are displayed in Figure 33. The symmetric vortex configuration was attained by applying the unsteady bleed through the far side control ports with $C_\mu = 0.002$. The value of C_y for this forcing amplitude was 0.01. The symmetric nature of the vortices can be seen in both the strobe light and laser sheet flow visualizations. In contrast to the natural case, the tip vortices did not separate from the model until $Z/D = 6.8$. The separation point may have been influenced by the pressure tap tubing at the base of the model. The pressure distributions on the near and far sides were almost identical resulting in a side force that was approximately zero. Thus, the vortices in the symmetric state are not capable of yawing the model to the left or right. The velocity contours indicate a symmetric vortex configuration and only minor distortions are noticeable.

When the control was activated on the far side with $C_\mu = 0.006$, the vortex system became asymmetric once again. The vortex configuration, however, was the reverse of the natural arrangement with $C_y = 0.47$. The data for this antisymmetric case is presented in Figure 34. It is evident from the flow visualization photographs that the vortex configuration was a mirror image of the configuration for the natural case. The stronger primary vortex on the near side separated close to the tip, while the weaker vortex on the far side did not separate until $Z/D = 5.4$. The vortex asymmetry is reflected in the pressure distribution, which shows that the higher pressures occurred on the near side of the model (open circles). The side force acted to the left as illustrated by the arrow in Figure 34(a), and has the capability to yaw the model in this direction. The velocity contours show the high-speed flow associated with the primary vortex. The high-speed flow can be seen at positive Y/D values in Figure 34(c).

The two vortex configurations for the bistable behavior at $\alpha = 55^\circ$ are shown in Figure 35 and Figure 36. The values of C_y for the natural (yaw left) and antisymmetric (yaw right) configurations were 0.58 and -0.52. For the natural case, the primary vortex formed on the near side of the model. The weaker vortex separated on the far side at a Z/D of approximately 4.0. The antisymmetric case was achieved by activating the unsteady bleed on the near side. The forcing amplitude was increased beyond the threshold value, and the vortices switched to the mirror image of their original configuration. As expected, the flow visualization photographs show that the primary vortex was now located on the far side of the model. The pressure distribution confirms this result, and is almost the reverse of the distribution for the natural case.

Spatial Instability Analysis

It is generally agreed upon that the vortex asymmetry originates in the tip region of the forebody model. The development of the vortex asymmetry is due to the amplification of the initial tip asymmetry by a spatial instability in the forebody wake. Despite careful machining of the forebody model, the cone tip always contains small geometric imperfections. These small imperfections are referred to as the "geometric asymmetry" of the cone. The geometric asymmetry produces the initial flow distortion in the tip region, and is responsible for the asymmetric vortex configuration. Experimental evidence that supports the spatial instability concept is presented in this section.

Symmetric Base Flow State   One important aspect of the instability analysis is the measurement of the base flow state. The base flow state is defined for the forebody wake as the state of the vortex system in the absence of any geometric asymmetry. Without the geometric asymmetry, the cone tip would be perfectly axisymmetric and the vortices would be arranged in the symmetric configuration. Consequently, the symmetric state of the vortex system is taken as the base flow state for the instability analysis.

The symmetric state was attained by balancing the geometric asymmetry with a controlled disturbance from the unsteady bleed. Mean and rms velocity profiles are plotted in Figure 37 and Figure 38 for $\alpha = 45^\circ$ and $Re = 6300$. The symmetric states shown in the figures were achieved with different levels of forcing. The symmetric state

was first reached by applying the unsteady bleed through the far side control ports with $C_\mu = 0.002$ (circles). Activating the control on the near side with $C_\mu = -0.005$ caused the vortex configuration to become asymmetric. Symmetry was restored by increasing the forcing amplitude on the far side to $C_\mu = 0.006$ (squares). This process of progressively increasing the forcing amplitude on both sides of the model was continued until a noticeable distortion in the velocity profiles occurred.

The symmetry of the velocity profiles can be clearly seen in the two figures. The velocity profiles display noticeable distortions only at the highest levels of forcing (stars). The distortions are especially evident in the rms velocity profile. At the highest levels of forcing, the nonlinear effects of the unsteady bleed have become significant. However, at lower forcing amplitudes the velocity profiles are not influenced by the nonlinearity of the control. These measured velocity profiles are equivalent to the symmetric base flow state.

Distortion Energy Measurements   Figure 39 shows a comparison between mean velocity profiles for the natural and symmetric cases at Z/D locations of 0.17, 1.6, 3.0, and 35. The velocity profiles were measured at a X/D_1 of 1.0, where D_1 is the local diameter of the forebody model. By using the local diameter to nondimensionalize the distance X, all of the velocity profiles were acquired at the same relative distance from the model axis.

The difference between the natural and symmetric profiles is a measure of the distortion at the corresponding axial location. It is apparent from Figure 39 that the distortion grows with increasing Z/D. The amount of distortion at a particular axial position can be quantified by defining a distortion energy as follows:

$$E_d = \int_{-l/2}^{l/2} \frac{(U_a - U_s)^2}{U_o^2} \, d(Y/D),$$

where U_a is the asymmetric mean velocity and U_s is the symmetric mean velocity. The quantity l represents the range of the velocity measurements in the y-direction.

The growth of the distortion energy is plotted on semilog coordinates in Figure 40. The data indicates exponential growth from the tip of the model until $Z/D = 4.5$, at which point the distortion energy saturates. The following equation can be used to find a least-squares curve fit to the experimental data:

$$E_d = E_o \exp(C \ Z/D).$$

The spatial growth rate C and the initial distortion energy at the tip E_o were found to be:

$$C = 2.1 \quad \text{and} \quad E_o = 8.9 \times 10^{-5}.$$

Wave Propagation Speed   When the forcing is applied to the tip region, it takes a finite amount of time before the flow downstream of the tip responds. The time delay t_d between the application of the control and the response of the flow is shown in Figure 41 for $\alpha = 45^o$ and 55°. The delay time was measured at $\alpha = 45^o$ with a hot-wire probe

located at $X/D_1 = 0.5$, $Y/D_1 = -0.4$. For 55° angle of attack, LDV measurements were acquired at $X/D_1 = 0.5$, $Y/D_1 = -0.5$. The figures show that the delay increased linearly with distance from the tip.

The controlled disturbance placed into the flow near the tip propagates downstream along the axis of the model as shown by the data in Figure 41. The wave propagation speed is the speed at which the controlled disturbance travels through the forebody wake. The slopes of the lines drawn in Figure 41 can be used to determine the wave propagation speeds along the model axis. The wave propagation speeds at $\alpha = 45^o$ and 55° were calculated to be 3.08 m/s (10.1 ft/s) and 2.50 m/s (8.2 ft/s) respectively. A nondimensional wave speed can be computed by dividing the wave propagation speed U_{ws} by the component of the freestream velocity parallel to the model axis. The nondimensional wave speed C_{ws} can be expressed as,

$$C_{ws} = \frac{U_{ws}}{U_o \cos\alpha},$$

where α is the angle of attack. For both angles of attack, the nondimensional wave speed was 1.32.

Effect of Reynolds Number on Vortex Asymmetry

For $\alpha > 50^o$, significant differences have been observed in the response of the vortex system to changes in the tip conditions. By using a moving wire to control the geometric asymmetry at the tip, Degani and Tobak (1991) showed that the vortex system always returned to its original state when the wire was removed from the flow. However, Williams and Bernhardt (1990) using the unsteady bleed technique found that the vortex system could be switched between two stable states. The original state of the vortex system was not recovered when the control was turned off. A similar bistable behavior was observed in experiments by Ng and Malcolm (1991). These fundamental differences in behavior can be resolved by examining the influence of Reynolds number on the vortex asymmetry.

Sectional Side-Force Measurements   The effect of Reynolds number on the sectional side-force coefficient is shown in Figure 42 for $\alpha = 55^o$. Small amounts of suction were applied through the control ports in order to manipulate the vortex asymmetry. At $Re = 6200$, the vortex system clearly exhibited a bistable behavior. Initially, the vortex asymmetry produced a C_y value of -0.57 (lower filled symbol). The first transition point occurred at $C_\mu = 1.47 \times 10^{-10}$, where the vortices rapidly switched to a mirror image of their original configuration with $C_y = 0.59$. No intermediate states could be attained with the forcing system at this Reynolds number. The vortices did not return to their original configuration when the control was turned off. Instead, the side-force coefficient remained at $C_y = 0.59$ (upper filled symbol).

The original state of the flow was recovered by applying suction to the opposite

side ($C_\mu < 0$). The transition point occurred at $C_\mu = -1.12 \times 10^{-10}$. When the control was switched off, the vortex system returned to its original configuration with $C_y = -0.57$. The arrows in Figure 42(a) indicate the path traveled around the hysteresis loop.

Increasing the Reynolds number to 12000 produced a different behavior as shown in Figure 42(b). The transition point from negative to positive C_y occurred at $C_\mu = 3.04 \times 10^{-9}$. Further increases in C_μ beyond the transition value had only a minor effect on the side force. Reducing the magnitude of C_μ toward zero resulted in a switch back to the original vortex configuration just before the suction was completely turned off. Forcing with $C_\mu < 0$ had no significant effect on the side-force coefficient. Once again, a hysteresis loop can be seen in the figure. It is important to note, however, that the flow had only one stable vortex configuration with two saturated states. This response of the vortex system is referred to as "two-state" behavior.

The hysteresis loop is no longer observed at Re = 18100 as shown by the data plotted in Figure 42(c) (solid line). The transition bleed coefficient at this Reynolds number was 0.85×10^{-8}. Within the resolution of the forcing system, no intermediate states could be achieved. A similar response of the vortex system was found at Re = 24000 (dashed line). For this Reynolds number, the transition bleed coefficient was 2.36×10^{-8}.

Increasing the Reynolds number to 30000 resulted in a fundamentally different behavior, i.e., intermediate values of the side-force coefficient appeared. The data plotted in Figure 42(d) shows the continuous variation of C_y with increasing C_μ, which is the type of behavior observed by Degani and Tobak (1991). This behavior is associated with a continuous change in the position of the vortices as documented by Bridges and Hornung (1992). Because of the continuous variation in vortex position, it was possible to obtain proportional control of the side force. For $C_\mu = 0.65 \times 10^{-7}$, the symmetric state of the vortex system was achieved with $C_y = 0.03$.

Proportional control of the side force was also demonstrated for Reynolds numbers of 36000, 42000, and 48100. Side-force measurements acquired at each Reynolds number are presented in Figure 42(e). For all three cases, the continuous variation of the side-force coefficient closely resembled the vortex system response at Re = 30000. Increasing the Reynolds number beyond 30000 did not cause any major changes in the vortex system response. An asymptotic behavior of the vortex system has been reached at these Reynolds numbers.

The behavior of the vortex system is summarized in Figure 43, which shows the sectional side-force coefficient for the natural case plotted versus the Reynolds number. Bistable behavior was observed at low Reynolds numbers up to 12000, while two saturated states occurred between 12000 < Re < 24000. The continuous variation of C_y was found at 30000 < Re < 48100.

<u>Critical Bleed Coefficient and System Gain</u>   The effect of Reynolds number on the forcing amplitude must be studied in order to determine general scaling relations for the suction control. An important quantity that represents the level of forcing at a particular Reynolds number is the critical bleed coefficient C_μ^*. For the bistable and two-state behavior of the vortex system, the critical bleed coefficient is defined as the forcing amplitude required to cause a jump from negative to positive C_y. The level of forcing necessary to achieve the symmetric vortex configuration is taken as the critical bleed coefficient for the continuous case.

The dependence of the critical bleed coefficient on the Reynolds number is shown in Figure 44. The data covers the Reynolds number range from 6200 to 42000. Regression analysis performed on the data suggests that the critical bleed coefficient is proportional to $Re^{3.9}$. Expressing this relationship in terms of velocities, the critical suction speed U_p^* is approximately proportional to U_0^3.

The previous results demonstrate that control of the side force can be accomplished with low forcing amplitudes and input power levels. The ratio of the side-force thrust power output to the actuator power input can be defined as the gain for the vortex system. The system gain G_s evaluated at the symmetric state is given by,

$$G_s = \frac{1}{2} \frac{U_0}{U_p^*} \frac{C_{yn}}{C_\mu^*},$$

where C_{yn} is the sectional side-force coefficient for the natural vortex configuration. Due to the spatial instability characteristics of the forebody wake, the system gain is on the order of 10^8 at a Reynolds number of 30,000. The implication of this result for control experiments is that extremely low levels of power to the actuator will produce large changes in the external flow field and side force.

Additional Flow Field Properties

The results described in this section focus on several additional features of the forebody wake investigated during the course of the research. Results are presented from experiments using the three vortex control techniques to compare differences in forcing amplitudes and vortex system behavior. Data acquired from the two-component external balance and the four-component internal balance shows interesting characteristics of the flow field as the total side force acting on the model approaches zero.

<u>Comparison of Vortex Control Techniques</u>   Control of the forebody flow asymmetry using suction, blowing, and unsteady bleed is compared in Figure 45 for $\alpha = 55^o$ and $Re = 6200$. The vortex system exhibits a bistable behavior for each of the three control techniques. However, the direction around the hysteresis loop depends on the type of forcing as illustrated by the arrows. The path traveled around the hysteresis loop is in the counterclockwise direction for both the unsteady bleed and suction control methods. In contrast, the path for steady blowing is exactly opposite and is in the clockwise direction.

The vortices can be switched from their natural configuration (filled circle) by applying unsteady bleed or suction through the far side control ports. The application of blowing through the near side control ports will also change the vortex configuration.

A comparison of the forcing amplitudes shows that bleed coefficients for steady suction are significantly smaller than C_μ values for either the unsteady bleed technique or steady blowing. Values of C_μ for unsteady bleed and blowing are on the order of 10^{-3} and 10^{-5} respectively. For steady suction, C_μ is on the order of 10^{-10}. Therefore, steady suction is more efficient than blowing or unsteady bleed for controlling the vortex asymmetry at low Reynolds numbers.

Side-Force Measurements Using the External Balance   One interesting characteristic of the flow field can be seen by examining measurements of the total side force obtained from the two-component external balance. Mean and rms values of the side-force coefficient C_Y are displayed in Figure 46 for the sharp-tip tangent-Ogive model positioned at $\alpha = 45^\circ$. The data was acquired at a Reynolds number of 30000 using steady suction to control the side force. Figure 46(a) shows a continuous variation of C_Y, which indicates proportional control of the forebody vortices. At a forcing amplitude of $C_\mu = 0.37 \times 10^{-5}$, the side force acting on the model was approximately zero with $C_Y = -0.12$.

The rms value of C_Y increased substantially as the side force approached zero. Figure 46(b) clearly shows this sudden jump in the rms value. The rms value started at 0.63 for the natural case (filled circle) and rapidly increased to a maximum of 1.36. After the side force passed through zero, the rms value quickly decreased to 0.61 for $C_\mu = 0.67 \times 10^{-5}$. The jump in the rms value can be attributed to an increase in the unsteadiness of the flow field due to vortex shedding.

Force and Moment Measurements with the Internal Balance   The pressure coefficient measurements indicate the state of the vortex system, but are only local measurements in space. Variables that measure the flow asymmetry on a global scale must also be considered. These important variables include the side and normal forces as well as the yawing and pitching moments. Force and moment measurements are presented in Figure 47 and Figure 48 for the round-tip tangent-Ogive model. The data was acquired using the four-component internal balance and the two Kulite pressure transducers. For $\alpha = 40^\circ$ and $Re = 40000$, the pressure coefficient was varied over its entire range of values and the balance readings were recorded.

Figure 47 shows the side-force coefficient C_Y and the normal-force coefficient C_N plotted versus C_p. It is interesting to note that as C_Y passed through zero, C_N reached a minimum value. This minimum value occurred at $C_p = -0.23$. The percentage decrease in C_N referenced to its value for the natural case was 17 %.

The C_p value of -0.23 is also important when considering the pitching-moment coefficient C_m and the yawing-moment coefficient C_n. These two coefficients are shown in Figure 48. For a C_p value of -0.23, C_n was approximately zero and C_m reached a local maximum value. The percentage increase in C_m was 22 %.

Control Maps for the Tangent-Ogive Models

Feedback control systems were developed for the two tangent-Ogive forebody models. The systems were designed to control the forebody flow asymmetry during an unsteady pitching maneuver. The unsteady maneuver consisted of a pitch-up motion where the angle of attack varied from 20° to 70°. The angle of attack history had the form of a cosine function. The control map represents the set of all attainable states that the control system can achieve during the unsteady pitching maneuver. For the results presented in this section, the region of control expressed in terms of C_p versus α defines the control map.

Control Maps   Figure 49 shows the control map for the sharp-tip cone at $Re = 60000$ and $\dot{\alpha} = 5^o / s$. The control map for the round-tip cone with $Re = 40000$ and $\dot{\alpha} = 5^o / s$ is shown in Figure 50. The differential pressure coefficient C_p is plotted on the ordinate and the angle of attack α is shown on the abscissa. Each curve is labeled with an actuator setting measured in steps of the stepper motor. Actuator positions range from -125 to $+125$ in increments of 25. The curves labeled with a zero represent the natural case, i.e., the case where no control was applied. A positive value of the actuator position designates suction applied through the far side control port, while a negative value denotes forcing through the near side control port. The actuator setting was fixed for each curve, so that the amount of suction at the tip remained constant during the pitch-up motion. The response of the vortex system to the control was measured in terms of C_p.

The control maps clearly show several important features of the flow field. For angles of attack from 20° to 30°, all of the curves are coincident. The value of the pressure coefficient is approximately zero, which corresponds to the symmetric vortex configuration. As the angle of attack is increased beyond 30°, the range of C_p values that can be achieved also increases. For instance, the pressure coefficient range at $\alpha = 50^o$ is near maximum and is certainly much greater than at 30°. In addition, the curves have spread apart indicating an increased sensitivity of C_p to the applied control. As the angle of attack approaches 55°, the pressure coefficient values converge to one of two possible curves. The convergence of the pressure coefficient indicates that only two vortex configurations are possible. This type of vortex behavior is referred to as a two-state condition.

As the actuator position increases, the pressure coefficient curves tend to reach the limiting curves. The limiting curves correspond to actuator positions of ± 125 in both

Figure 49 and Figure 50. The limiting curves define the outer envelope of the control region. The control system must operate within the region defined by the limiting curves.

Control of Forebody Flow Asymmetry

The results presented in this section concentrate on the closed-loop control systems designed for the two tangent-ogive models. The control objective was to manipulate the forebody flow asymmetry during an unsteady pitching maneuver. Both linear and nonlinear control laws were developed and evaluated for this study. The linear controllers employed a PID control law to determine the actuating signal. The nonlinear controller consisted of a neural network in combination with a PD control law. The implementation of the different control laws provided a better understanding of the important fluid physics of the control problem that would be generic to any flight vehicle.

PID Control Laws   A linear PID control law was developed for both tangent-ogive models. A detailed discussion of the procedure for setting the control law gains can be found in the Ph.D. dissertation by Bernhardt (1996). The desired value of the pressure coefficient was selected to be zero, which corresponded to a symmetric vortex configuration. Since the pressure coefficient had only one value at low angles of attack, the PID control laws were not activated until α reached 25°.

A comparison between the natural case (dotted line) and the controlled case (solid line) is shown in Figure 51(a) for the sharp-tip cone with $\dot{\alpha} = 5^{\circ}/s$ and $Re = 60000$. It is clearly seen from the figure that the PID controller was able to modify the pressure coefficient during the pitching maneuver. In addition, the PID controller was able to maintain C_p close to the desired value of zero for angles of attack up to 49°. At $\alpha = 49^{\circ}$, a sudden jump in C_p occurred from 0.05 to 0.34. The controller applied a corrective action to drive the pressure coefficient toward zero, but eventually an oscillation developed. The amplitude of the oscillation increased with angle of attack and the controller could no longer maintain the pressure coefficient near zero. Figure 51(b) presents the results for the same PID controller where the pitch rate has been increased to $10^{\circ}/s$. It can be seen from the figure that the controller had more difficulty keeping C_p near zero, especially in the range $40^{\circ} < \alpha < 50^{\circ}$.

A linear PID control law was also developed for the round-tip model. The results for this controller with $Re = 40000$ are displayed in Figure 52. The pressure measurements presented in Figure 52(a) show a comparison between the natural case and the controlled case for $\dot{\alpha} = 5^{\circ}/s$. The data indicates that the controller was effective up to $\alpha = 50^{\circ}$. Beyond this angle of attack, the controller was unable to damp the oscillations in the pressure coefficient. Increasing the pitch rate to $10^{\circ}/s$ produced the results shown in Figure 52(b). The controller had difficulty in maintaining the pressure coefficient near zero particularly around $\alpha = 40^{\circ}$.

Neural Network - PD Controller   The second controller designed and analyzed for the experiments was a nonlinear controller consisting of a neural network in combination

with a PD control law. This controller was exclusively developed for the sharp-tip cone. Comparisons between the natural and controlled cases are shown in Figure 53 for a Reynolds number of 60000 and pitch rates of $5^o / s$ and $20^o / s$. By comparing these two cases in Figure 53(a), it is apparent that the controller was able to modify the pressure coefficient and maintain C_p close to the desired value of zero up to $\alpha = 49^o$. For angles of attack greater than 49°, an oscillation in C_p occurred and the controller was no longer able to maintain the pressure coefficient near zero. Figure 53(b) shows a similar result for the higher pitch rate of $20^o / s$. The controller was again effective up to $\alpha = 49^o$, at which point oscillations in the pressure coefficient appeared.

Time Delay Measurements   The control systems used to manipulate the forebody flow asymmetry include a time delay between the actuator and the pressure transducers. It takes a finite amount of time for the forcing to travel from the valve to the control port. In addition, a finite time is required for the control applied at the tip to convect along the model axis and reach the location of the pressure transducers. These two times added together comprise the time delay for the control systems.

The time delay t_d was estimated for the sharp-tip model at $\alpha = 40^o$ and $Re = 30000$. Figure 54 shows the time delay measured using the Kulite pressure transducers. The time delay was found to be 0.015 s. The convective time scale L / U_o can be used to define a normalized time delay τ_d in the following manner:

$$\tau_d = \frac{t_d}{(L / U_o)},$$

where L is the length of the forebody model. For the sharp-tip cone, the normalized time delay was 0.78.

5. Conclusions

These experiments indicate that controlled leading-edge suction can be used in principle as an effective tool to control or modify the dynamic-stall vortex over the suction surface of a two-dimensional, pitching airfoil. The suction required for complete suppression of the vortex depends on pitch rate, airfoil angle of attack, and Reynolds number. Complete suppression is possible over a defined domain of parameter space. The pitch rate is the primary factor that determines suction requirements. The Reynolds number becomes an increasingly important factor as the pitch rate decreases, and transition to turbulence in the shear layer increases the complexity of the flow field. Under these conditions, the limitations described restrict the use of leading-edge suction for a complete suppression of the DSV. However, when the objective of flow control is partial suppression, leading-edge suction can be used effectively over a wider domain of parameters. This may be a useful approach, for instance, to delay detachment of a formed DSV. Since the formation of the DSV results in increased lift, a delay in the detachment of the DSV could be utilized to get increased lift for a longer period of time, and push the

occurrence of dynamic stall to higher angles of attack. Metwally showed that for one set of conditions he examined, suction control delayed the events in the DSV formation and detachment by 40% of the pitch-up period relative to the natural case.

The experiments have also provided useful information on the behavior of the unsteady pressure field over pitching airfoils with the application of leading-edge suction for flow control. The optimum suction flow rates required to meet three different control objectives were determined, and specifications for the flow state over the airfoil surface to satisfy these objectives were developed. The data were also very useful in the development of a neural-network controller that can be used to determine any change required in the suction to maintain a suppressed vortex. In the near future, these results will be used to develop a prototype for an on-line control system for flow management over two-dimensional pitching airfoils.

The forebody experiments have demonstrated the feasibility of an active closed loop control system to maintain a desired side force during pitch up and pitch down maneuvering. Very low power input was required to modify the forebody vortices. The implication to prototype aircraft is that similar control systems can be used to enhance the maneuverability at angles of attack up to 55 degrees, where conventional control authority is not effective. The linear PID control algorithms were as effective as the neural network approach, suggesting that very fast time response of the controller can be achieved.

Demonstration experiments are continuing on a coning motion model. The coning motion model is free to rotate about a sting, due to yaw moments produced by the forebody vortex system. Using a simple PC-computer it has been possible to control the yaw angle of the model, its rotation rate and the direction of rotation. This provides a clear indication of the power of the control techniques.

6. References

Abbott, I. H., and von Doenhoff, A.E., Theory of Wing Sections, Dover, New York, 1959.

Acharya, M., Karim M. A. and Metwally M. H., "Development of the Dynamic-Stall Vortex over a Pitching Airfoil," 1995, submitted for publication.

Acharya, M., and Metwally, M.H., "Unsteady Pressure Field and Vorticity Production over a Pitching Airfoil," *AIAA Journal*, Vol. 30, No. 2, 1992, pp.403-411.

Alrefai, M., The Unsteady Pressure Field and Flow State over a Pitching Airfoil with Leading-Edge Suction, M. S. Thesis, MAE Dept., Illinois Institute of Technology, Chicago, Illinois, August 1995.

Alrefai, M., and Acharya, M., "Controlled leading-Edge Suction for the Management of Unsteady Separation over Pitching Airfoils," AIAA Paper 95-2188, June 1995.

Anderson, S.R., Feedback Control of Flow Separation and Transition to Turbulence in Unsteady Boundary Layers, Ph.D Thesis, Illinois Institute of Technology, Chicago, May 1992.

Anderson, S. R., and D'Souza, "Feedback Control of Separation and Transition to Turbulence in Unsteady Flow", submitted to the Journal of Fluid Mechanics for publication.

Balas, M.J., "Nonlinear State Estimation and Feedback Control of Nonlinear and Bilinear Distributed Parameter Systems," Transactions of the ASME, Journal of Dynamical Systems, Measurement and Control, Vol. 102, June 1981, pp. 78-83.

Bernhardt, J. E., "Closed-Loop Control of Forebody Flow Asymmetry," Ph.D. Dissertation, MMAE Dept., Illinois Institute of Technology, Chicago, Illinois, (to appear 1996).

Bisplinghoff, R.L., Ashley, H., and Halfman, R.L., Aeroelasticity, Addison-Wesley, Reading, Mass., 1957.

Brogan, W. L., "Optimal Control Theory Applied to Systems Described by Partial Differential Equations," in Advances in Control Systems, Vol. 6, Leondes, C. T., editor, Academic Press, New York, N. Y., 1968, pp. 221-316.

Dowell, E. H., Editor, Curtis, H. C., Scanlan, R. H. and Sisto, F. A Modern Course in Aeroelasticity, Second Edition, Kluwer Academic Publishers, the Netherlands, 1989.

Ericsson, L. E., and Reding J. P., "Fluid Dynamics of Unsteady Separated Flow. Part II. Lifting Surfaces," *Progress in Aerospace Sciences,* Vol. 24, 1987, pp. 249-356.

Franke, D. Adaptive and robustness properties of certain bilinear distributed parameter control systems. Distributed Parameter Control Systems - Theory and Applications, Tzafestas, S. G., ed., Pergamon Press, 1982, pp. 179-212.

Gad-el-Hak, M., Unsteady Separation on Lifting Surfaces, Applied Mechanics Review, Vol. 40, No. 4, April 1987, pp.441-453.

Gad-el-Hak, M., Bushnell, D. M., "Separation Control," Review, Journal of Fluids Engineering, Vol. 113, March 1991, pp.5-29.

Greenberg, M.D., Applications of Green's Functions in Science and Engineering, Prentice-Hall, Inc., Englewood Cliffs, N.J., 1971.

Herbst, W. B., "Supermaneuverability," Joint Automatic Control Conference, University of Virginia, Charlottville, Va, June 17-19, 1981.

Karim, M., A., "Experimental Investigation of the Formation and Control of the Dynamic-Stall Vortex Over a Pitching Airfoil," M. S. Thesis, MAE Dept., Illinois Institute of Technology, Chicago, Illinois, 1992.

Karim, M. A. and Acharya, M., "Suppression of Dynamic-Stall Vortices over Pitching Airfoils by Leading-Edge Suction," *AIAA Journal*, Vol. 32, No. 8, August 1994, pp. 1647 -1655.

Karim, M.A., and Acharya, M. "Control of the Dynamic Stall Vortex over a Pitching Airfoil by Leading-edge Suction," AIAA paper 93-3267, AIAA Shear Flow Conference, July 6-9, 1993, Orlando, Florida.

Katz, J. and Plotkin, A. Low-Speed Aerodynamics (From Wing Theory to Panel Methods), McGraw-Hill, 1991.

Kawthar-Ali, M. H. and Acharya, M., "Artificial Neural Networks for Suppression of the Dynamic-Stall Vortex over Pitching Airfoils," AIAA Paper 96-0540, 34th AIAA Aerospace Sciences Meeting, Reno, NV, January 1996.

Lighthill, M.J., "On Displacement Thickness," Journal of Fluid Mechanics, Vol. 4, 1958, pp. 383-392.

Mansy, H. and Williams, D. R., "Flow Meter Based On The Trapped Vortex Pair Fluidic Oscillator," *Rev. of Scientific Ins.*- Pub. of : American Inst. of Physics, Vol. 60, No. 5, 1989, pp. 935-938.

McCroskey, W.J., "Inviscid Flowfield of an Unsteady Airfoil," AIAA Journal, Vol. 11, No. 8, August 1973, pp. 1130-1136.

McCroskey, W. J., "Unsteady Airfoils," Annual Review of Fluid Mechanics, Vol. 14, 1982, pp. 285-311.

Metwally, M. H., Investigation and Control of the Unsteady Flowfield over a Pitching Airfoil, Ph.D Thesis, Illinois Institute of Technology, Chicago, December 1991.

Nagib, H.M., Reisenthel, P.H., and Koga, D.J., "On the Dynamical Scaling of Forced Unsteady Separated Flows," AIAA paper 85-0553, AIAA Shear Flow Control Conference, March 12-14, 1985, Boulder, Colorado.

Ramirez-Serrano, A., Neural Network for Flow Field over Unsteady Airfoils, M.S. Thesis, Illinois Institute of Technology, Chicago, October 1993.

Rao, P.S., <u>Control of Distributed Parameter Systems with State Estimation</u>, M.S. Thesis, Illinois Institute of Technology, Chicago, December 1988.

Reisenthel, P.H., Nagib, H.M., and Koga, D.J., "Control of Separated Flows Using Forced Unsteadiness," <u>AIAA paper 85-0556</u>, AIAA Shear Flow Control Conference, March 12-14, 1985, Boulder, Colorado.

St. Hilaire, A.O. and Carta, F. O. "Analysis of unswept and swept wing chordwise pressure data from an oscillating NACA 0012 airfoil." Experiment, Vol. II-Data Report, CR-165972, NASA, 1972.

Sakawa, Y. , "Optimal filtering in distributed parameter systems," *Int. Journal of Control* Vol. 16, 1972, pp 115-127.

Saxena, L. S., <u>An Experimental Investigation of Oscillating Flows over Airfoils</u>, Ph.D Thesis, Illinois Institute of Technology, Chicago, May 1977.

Schlichting, H., <u>Boundary Layer Theory</u>, McGraw Hill Book Company, New York, N.Y, 1979.

Sears, W.R., and Telionis, D.P., "Boundary Layer Separation in Unsteady Flow," *SIAM Journal of Applied Mathematics*, 28, 1975, pp. 215-235.

Tzafestas, S.G., editor, <u>Distributed Parameter Control Systems, Theory and Applications,</u> Pergamon Press, 1982.

Von Karman, T. and Sears, W. R. "Airfoil theory for nonuniform motion," *Journal of the Aeronautical Sciences* Vol. 5, 1930, pp.379-390.

Visbal, M.R., "On the Formation and Control of the Dynamic Stall Vortex on a Pitching Airfoil," <u>AIAA Paper 91-0006</u>, 29th Aerospace Science Meeting, January 7-10, 1991, Reno, Nevada.

Visbal, M.R., and Shang, J.S., "Numerical Investigation of the Flow Structure Around a Rapidly Pitching Airfoil," <u>AIAA paper 87-1424</u>, AIAA 19th Fluid Dynamics, Plasma Dynamics and Lasers Conference, June 8-10, 1987, Honolulu, Hawaii.

Wang, P. K. C., "Control of Distributed Parameter Systems," in <u>Advances in Control Systems</u>, Vol. 1, Leondes. C. T., editor, Academic Press, New York, N. Y. 1964, pp. 75-174.

Williams, J. C., "Incompressible Boundary-Layer Separation," <u>Annual Review of Fluid Mechanics</u>, Vol. 9, 1977, pp. 113-144.

Yang, J., Ghia, K. N., Ghia, U. and Osswald, G. A., "Management of Dynamic Stall Phenomenon Through Active Control of Unsteady Separation," AIAA Paper 93-3284, Orlando, FL, July 1993.

7. Theses and Publications

Theses

Alrefai, M., "The Unsteady Pressure Field and Flow State over a Pitching Airfoil with Leading-Edge Suction," M. S. Thesis, MAE Dept., Illinois Institute of Technology, Chicago, Illinois, August 1995.

Karim, M. A., "Experimental Investigation of the Formation and Control of the Dynamic-Stall Vortex Over a Pitching Airfoil," M. S. Thesis, MAE Dept., Illinois Institute of Technology, Chicago, Illinois, 1992.

Rao, P. S., "Feedback Control of Unsteady Flow Separation over Airfoils," Ph.D. Dissertation, MAE Dept., Illinois Institute of Technology, Chicago, Illinois, May 1994.

Bernhardt, J. E., "Closed-Loop Control of Forebody Flow Asymmetry," Ph.D. Dissertation, MMAE Dept., Illinois Institute of Technology, Chicago, Illinois, (to appear 1996).
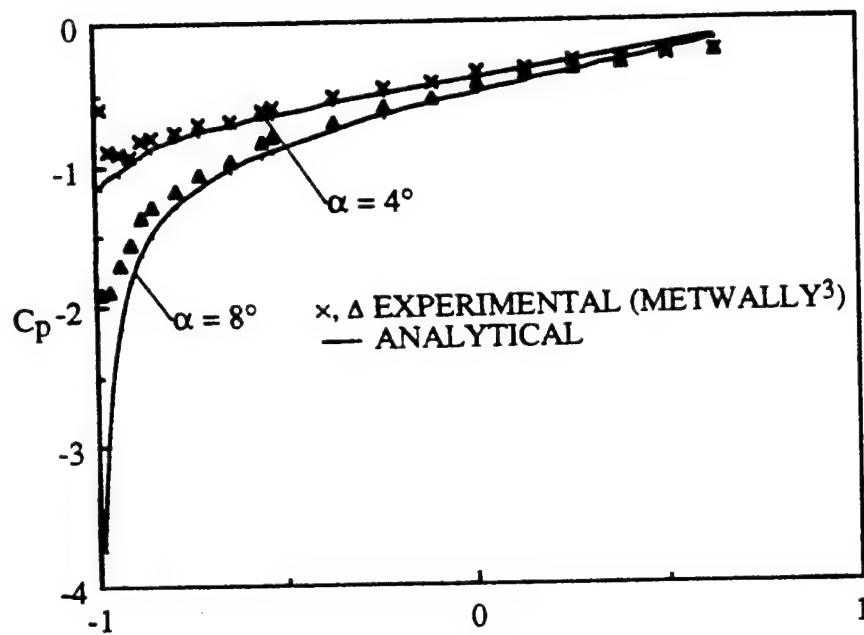
Figure 1.　Pressure coefficient for $\dot{\alpha}^+ = 0.036$
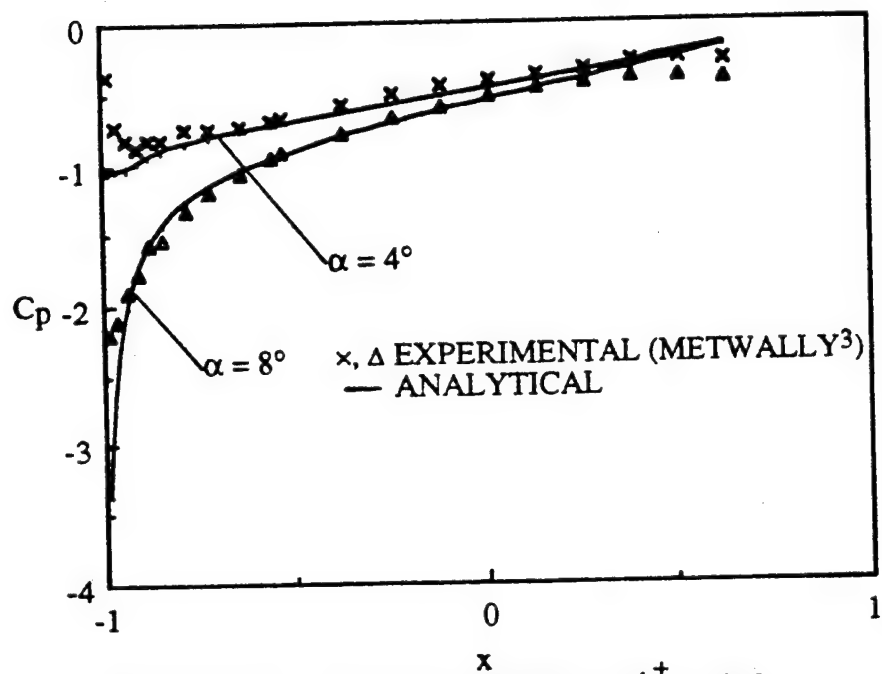
Figure 2.   Pressure coefficient for $\dot{\alpha}^+ = 0.072$
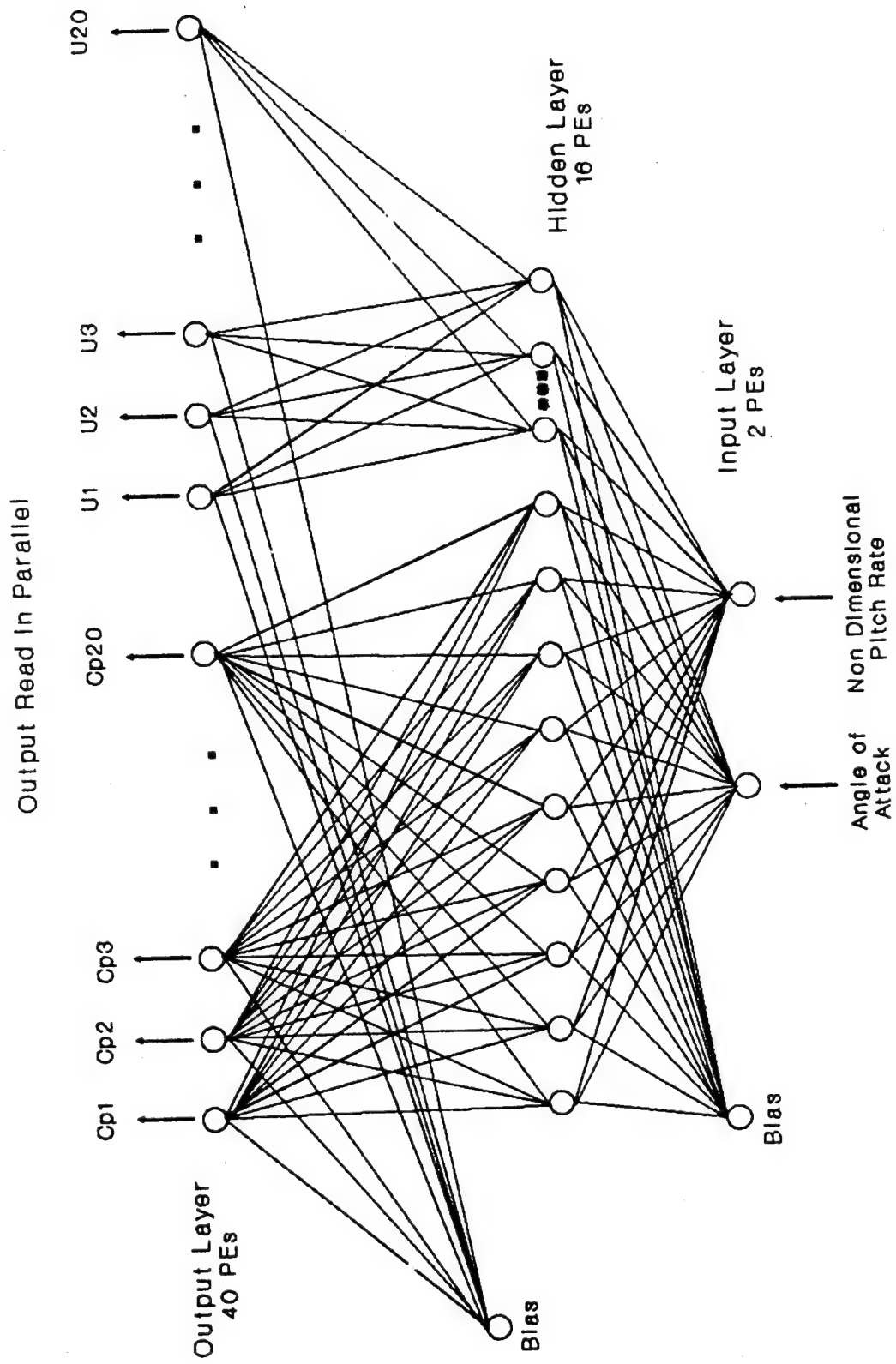
Figure 3. Schematic Representation of the Back Propagation Network
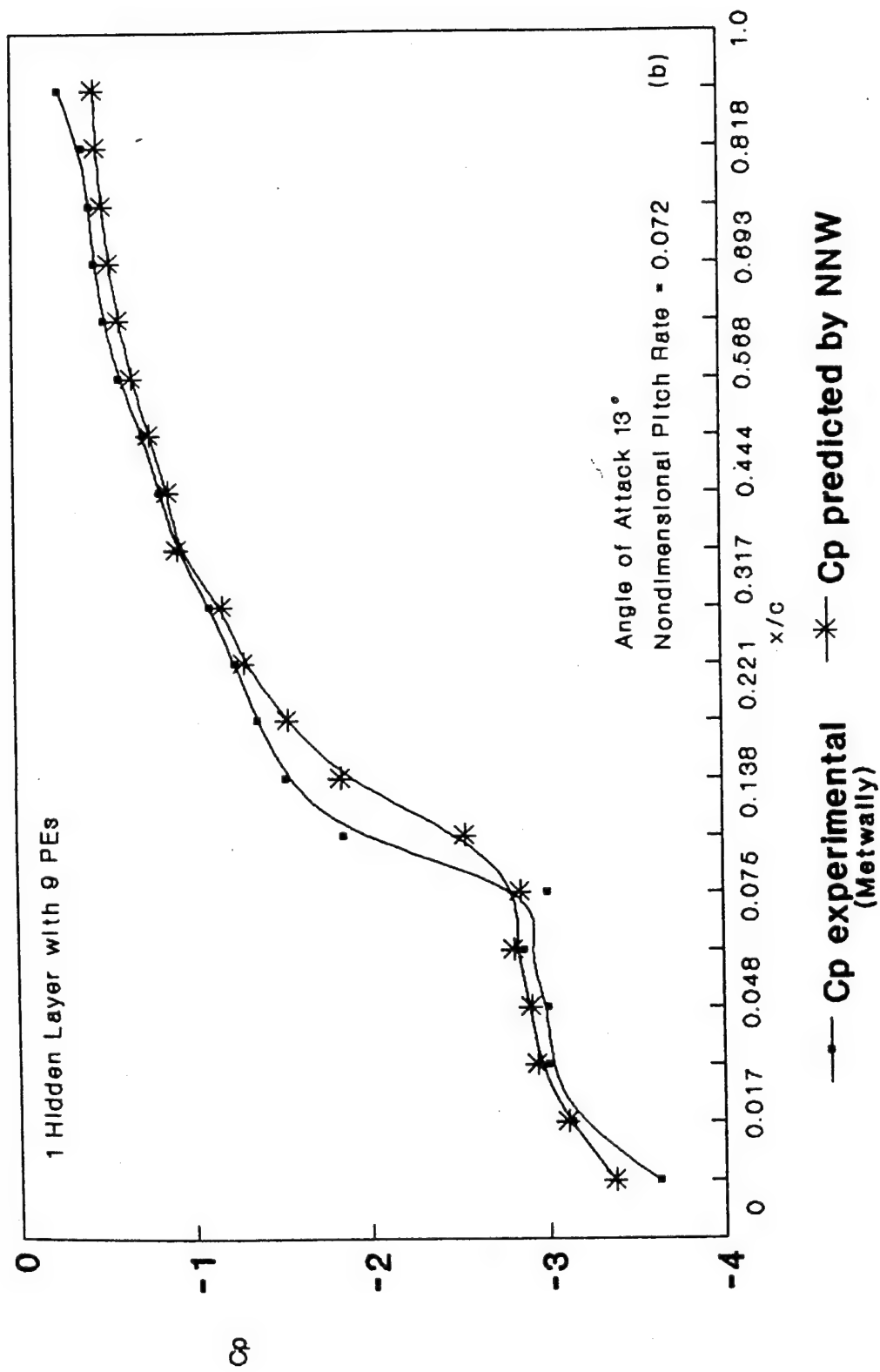
Figure 4. Pressure Coefficient
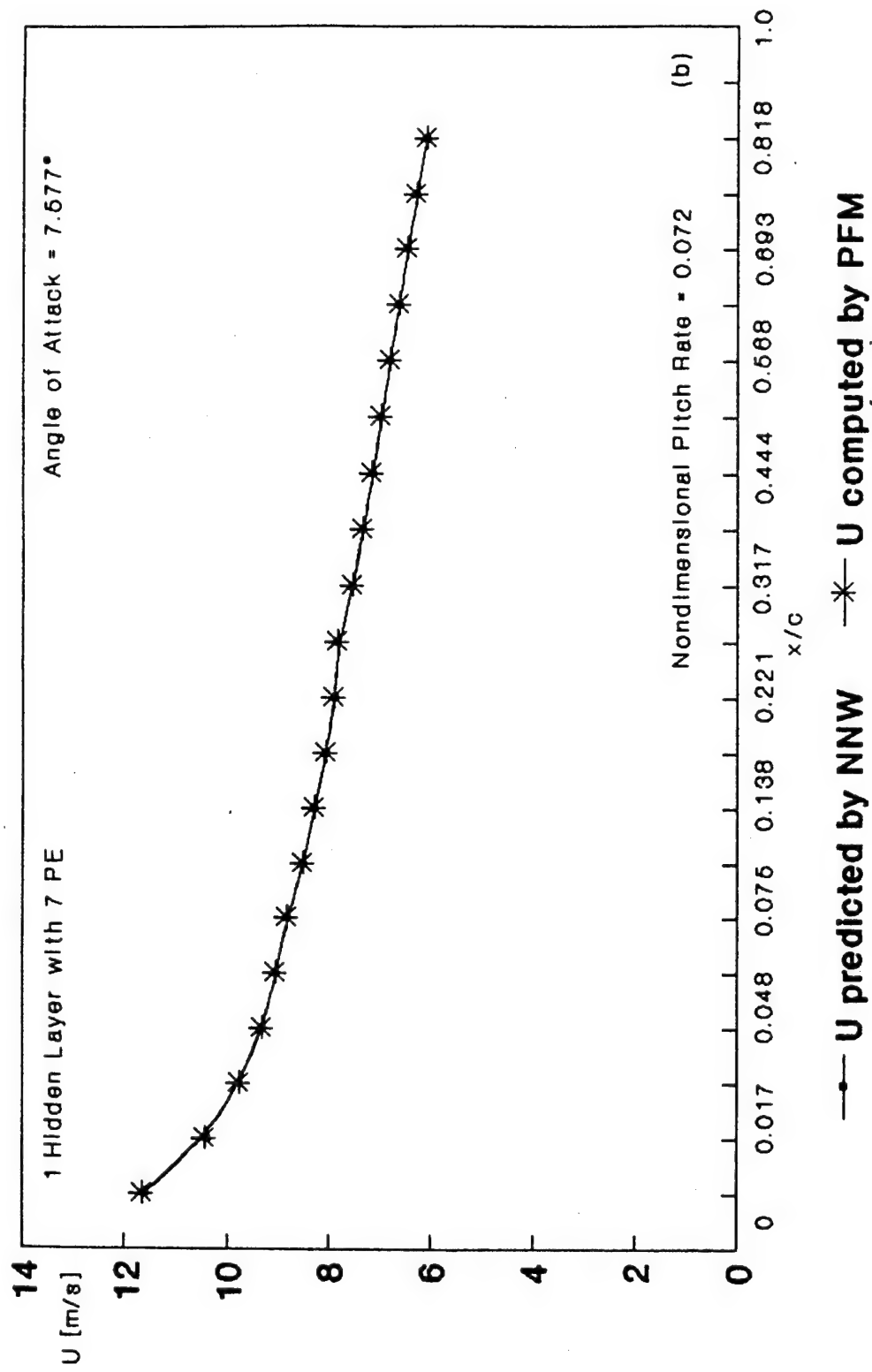
Figure 5. Tangential Velocity
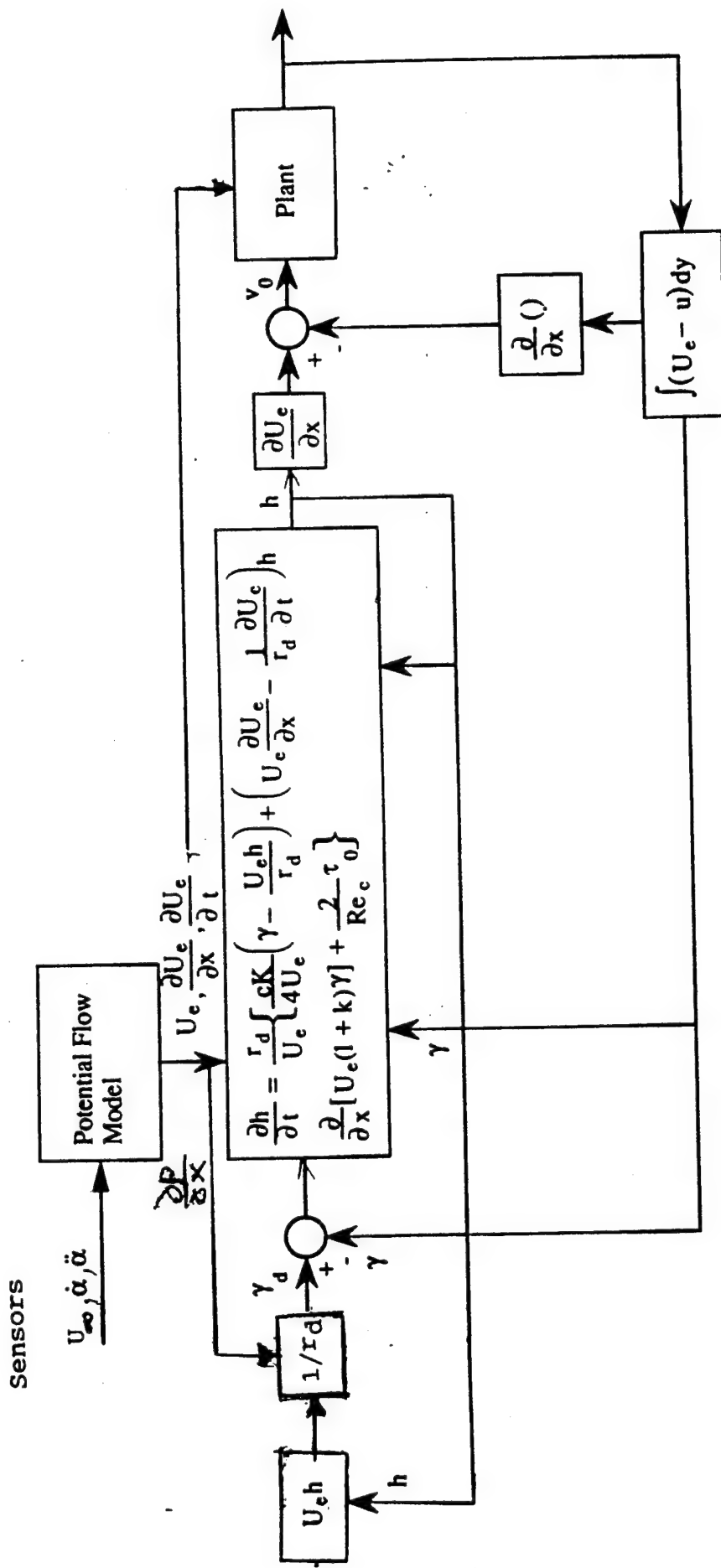
Figure 6. Block Diagram of the Control System
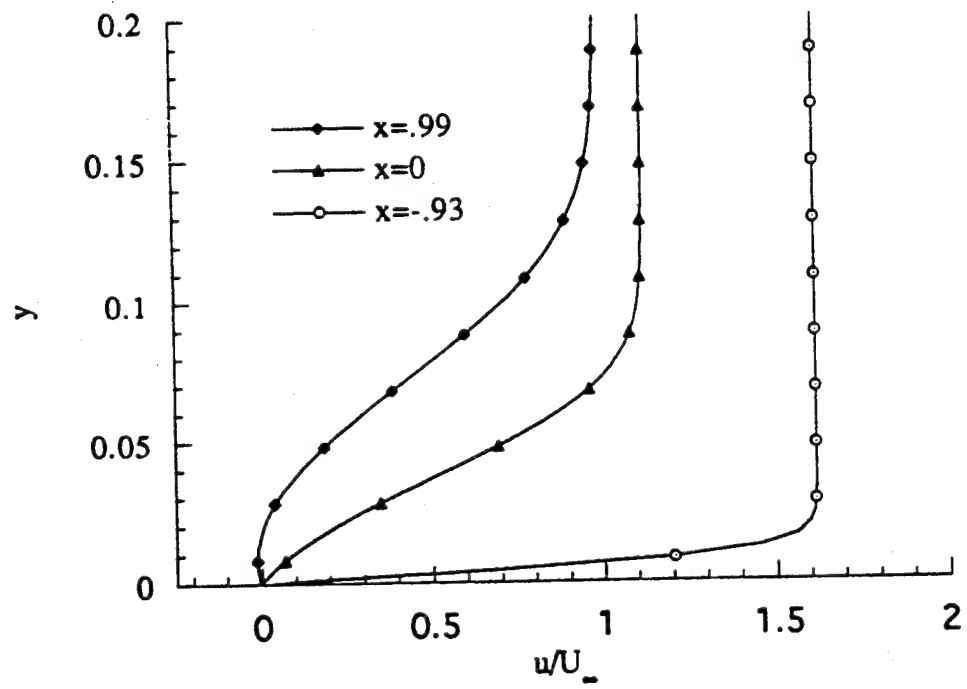
Figure 7. Velocity Profiles at Separation for $\dot{\alpha}^+ = 0.072$
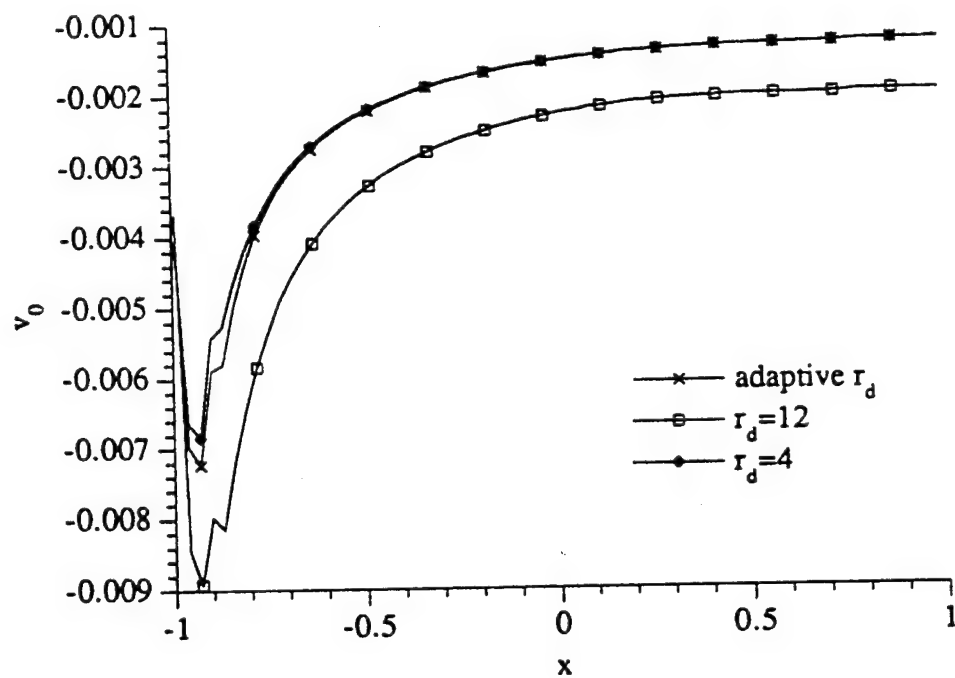
(a) $\alpha = 8°$

Figure 8. Suction Velocity Distribution for $\alpha^+ = 0.036$

(b) $\alpha=14°$

Figure 8. (concluded)

(a) $\alpha = 14^{0}$ (b) $\alpha = 16^{0}$

view: 25% of chord

(c) $\alpha = 18^{0}$ (f) $\alpha = 25^{0}$

(d) $\alpha = 20^{0}$ (g) $\alpha = 26^{0}$

(e) $\alpha = 24^{0}$ (h) $\alpha = 27^{0}$
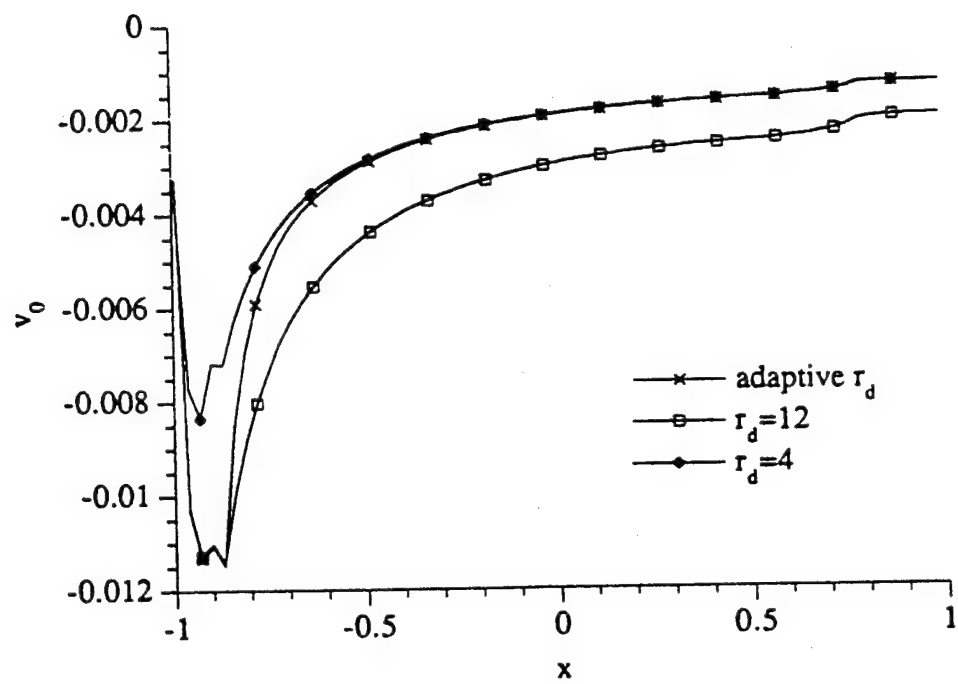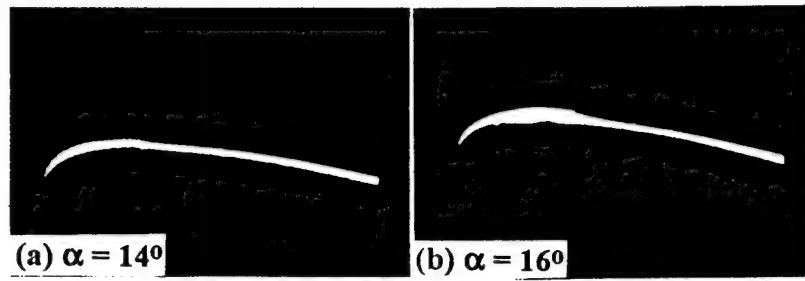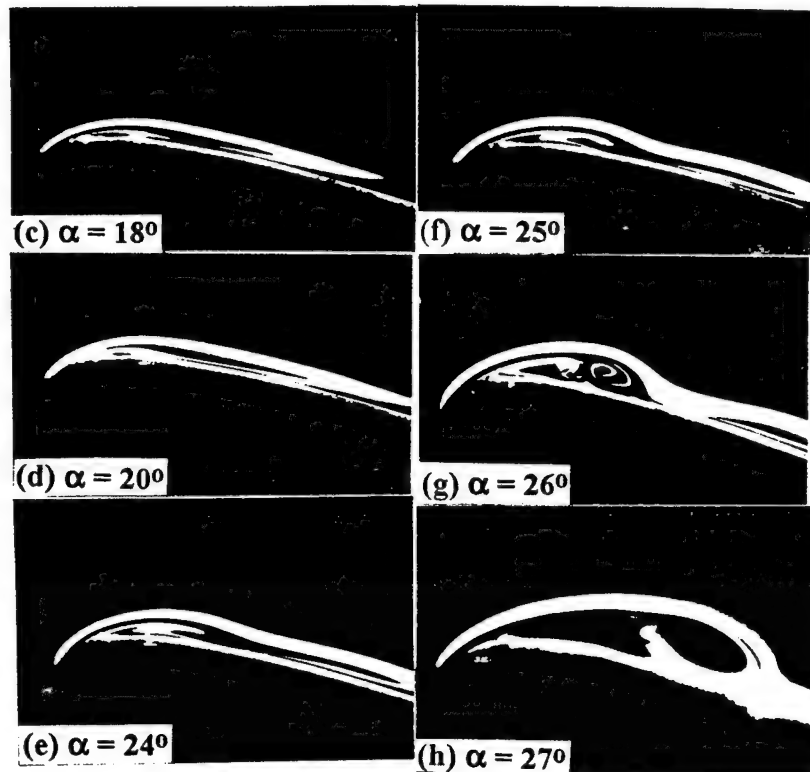
view: 12% of chord

Fig. 9   Flow-visualization records showing development of the DSV over a pitching airfoil ($\alpha^{+} = 0.31$, $Re_{c} = 30{,}000$).
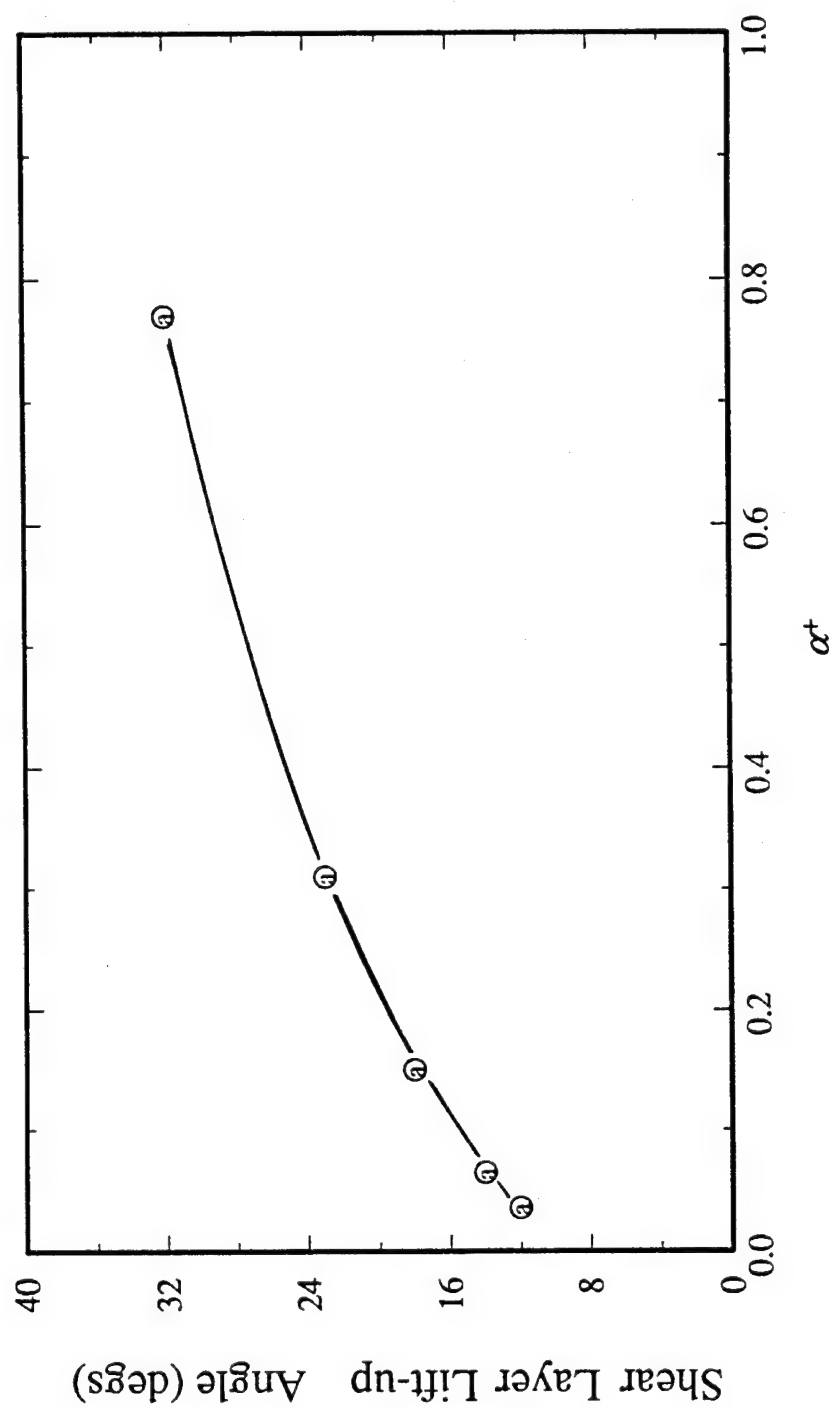
Fig. 10 Variation of shear-layer lift-up angle with pitch rate.

Natural case   Controlled case
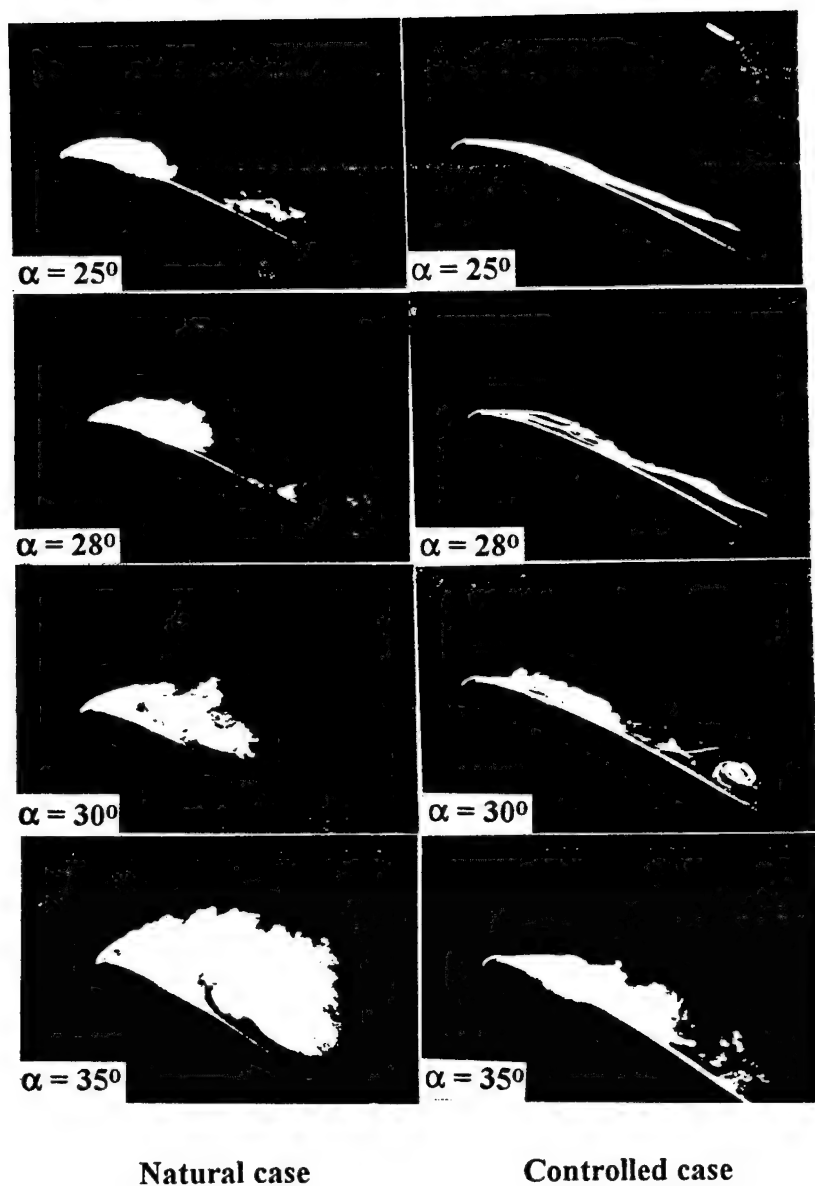
Fig. 11   Effect of suction on flow development during pitch-up of airfoil ($\alpha^+ = 0.15$, $Re_c = 30,000$, $Q_{nd}=0.0127$, view shown 67% of airfoil suction surface).
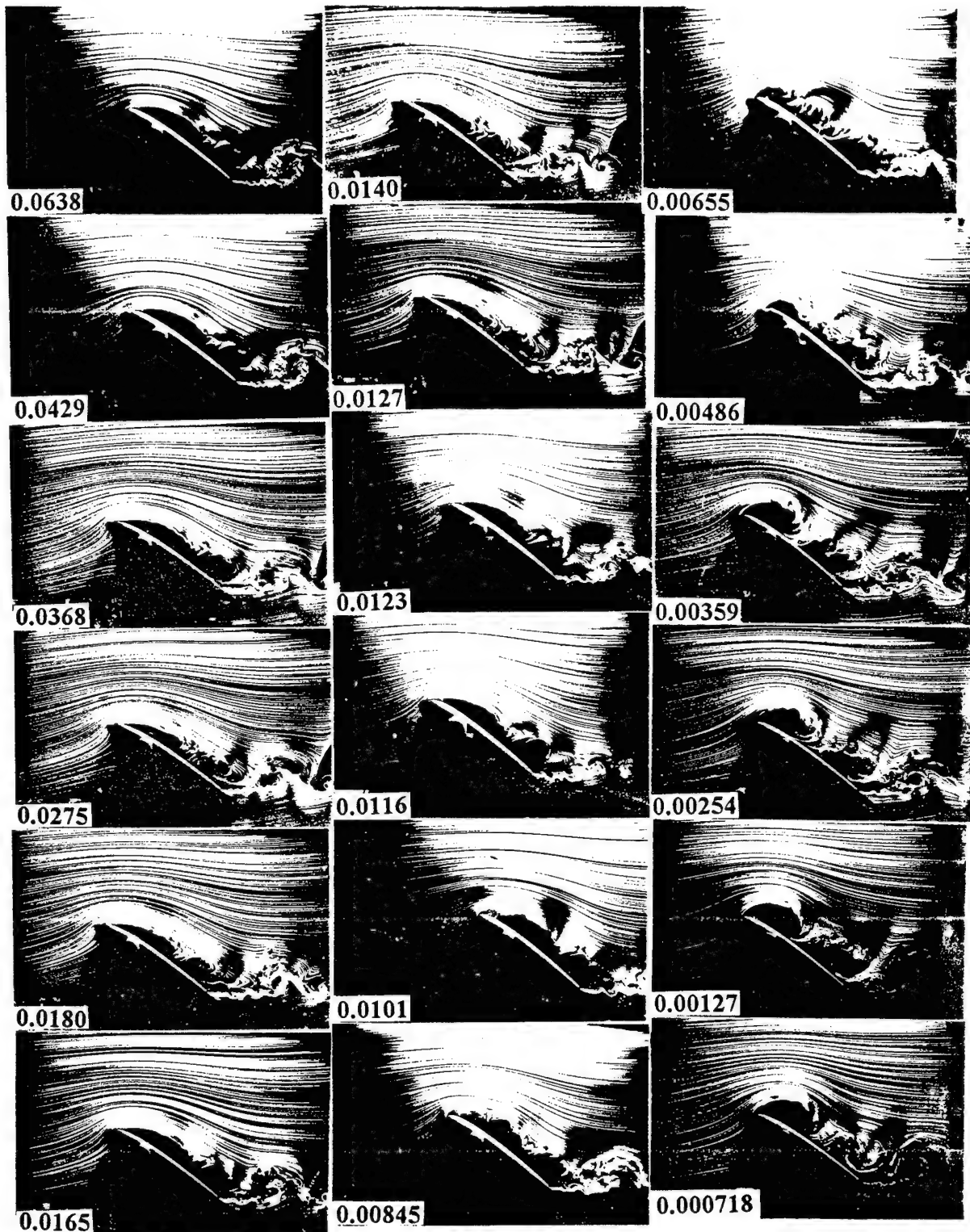
Fig. 12   Influence of suction flow rate on the development of the DSV ($\alpha^+ = 0.15$, $Re_c = 30,000$, $\alpha = 35^o$).
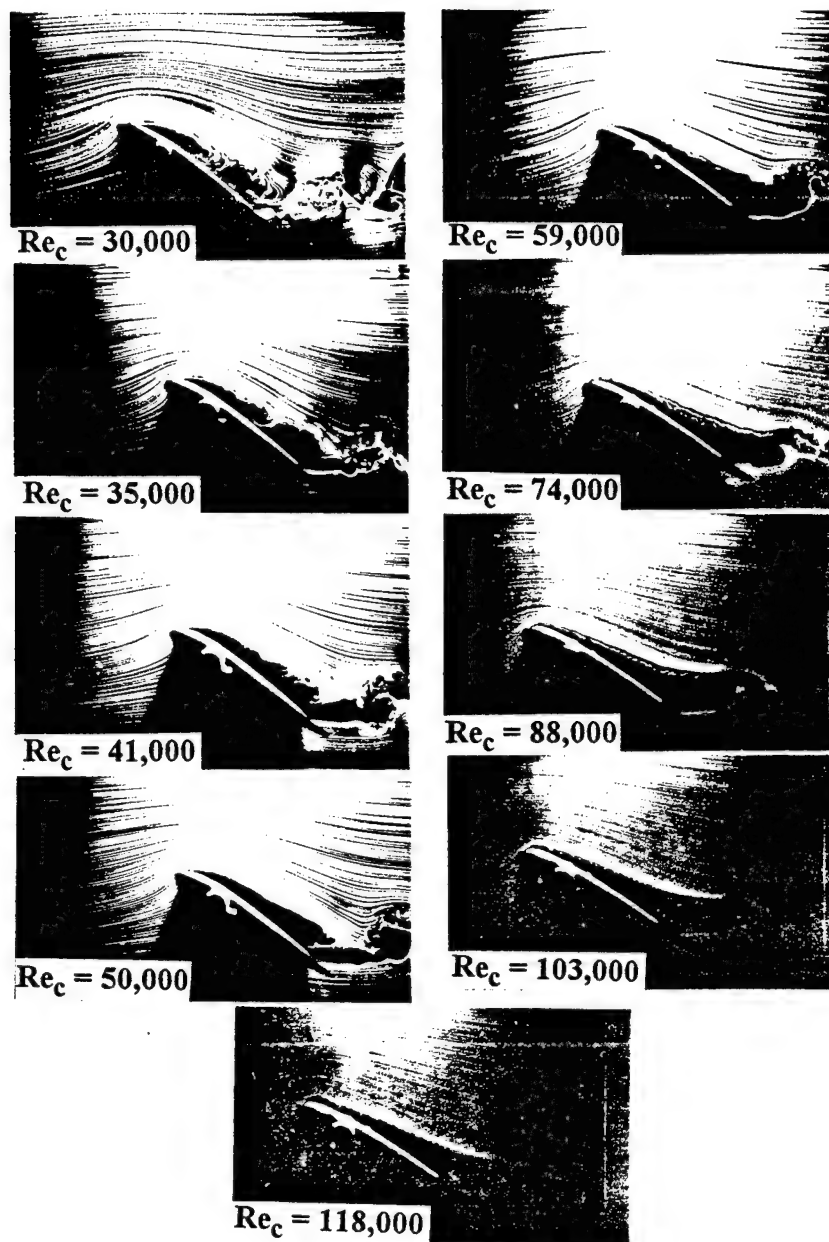
Fig. 13 State of flow field over a pitching airfoil ($\alpha^+ = 0.15$, $\alpha = 35^o$) for different Re_c, with a dimensionless suction flow rate of 0.0127.
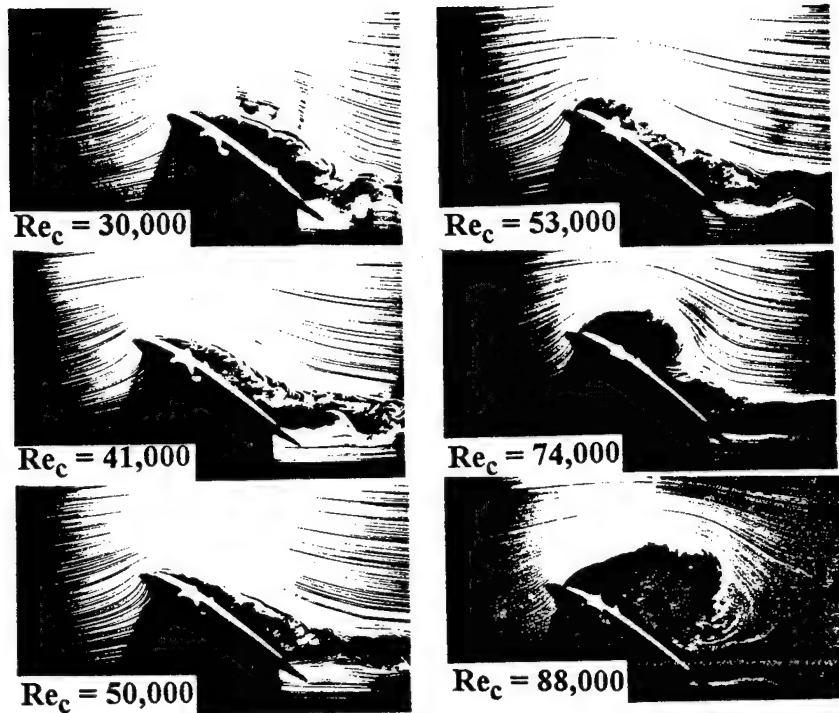
Fig. 14 State of flow field over a pitching airfoil ($\alpha^+ = 0.072$, $\alpha = 35^\circ$) for different Re_c, with a dimensionless suction flow rate of 0.109.
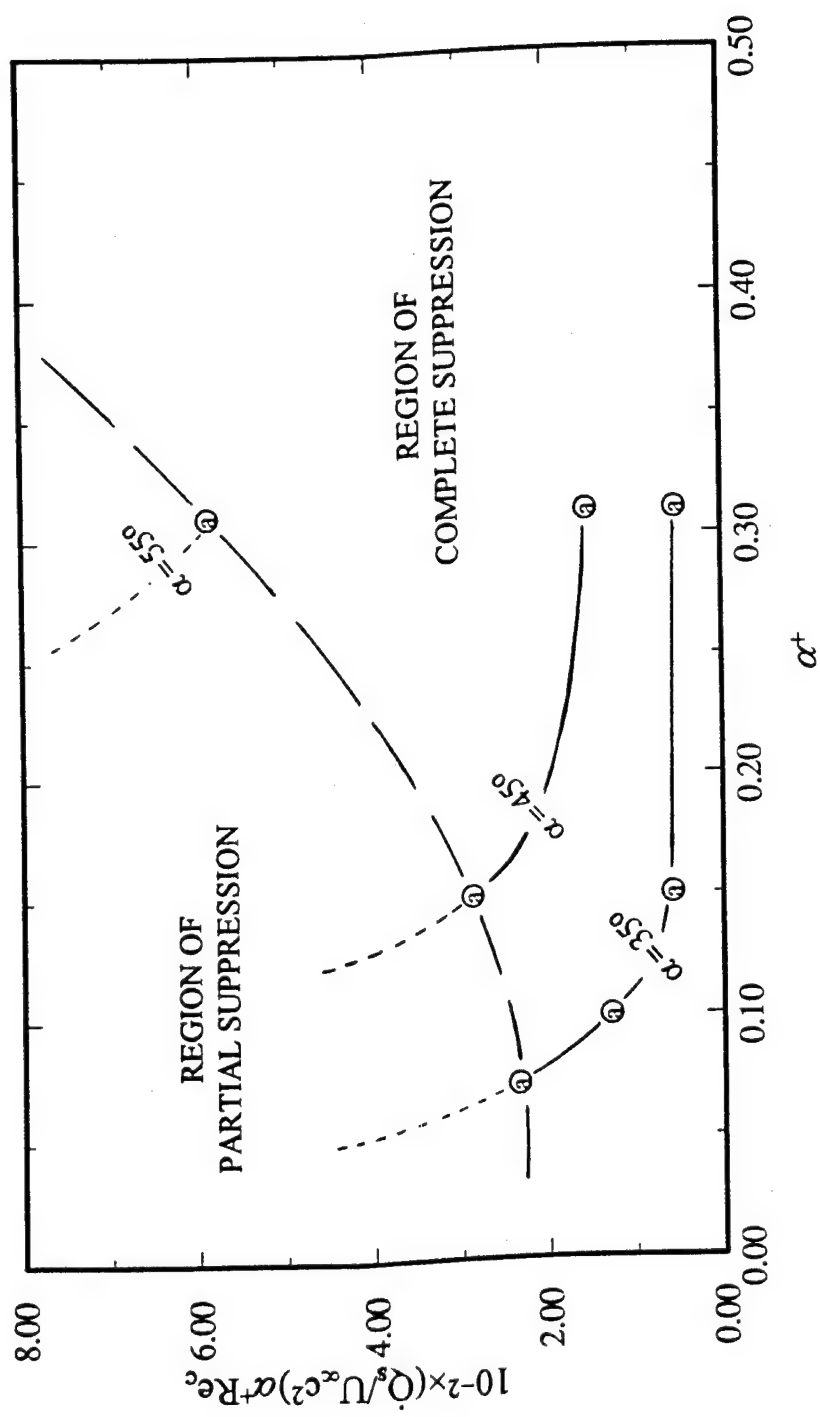
Fig. 15 Variation of suction flow rate for complete suppression of the DSV with pitch rate, at different angles of attack during the airfoil pitch-up.
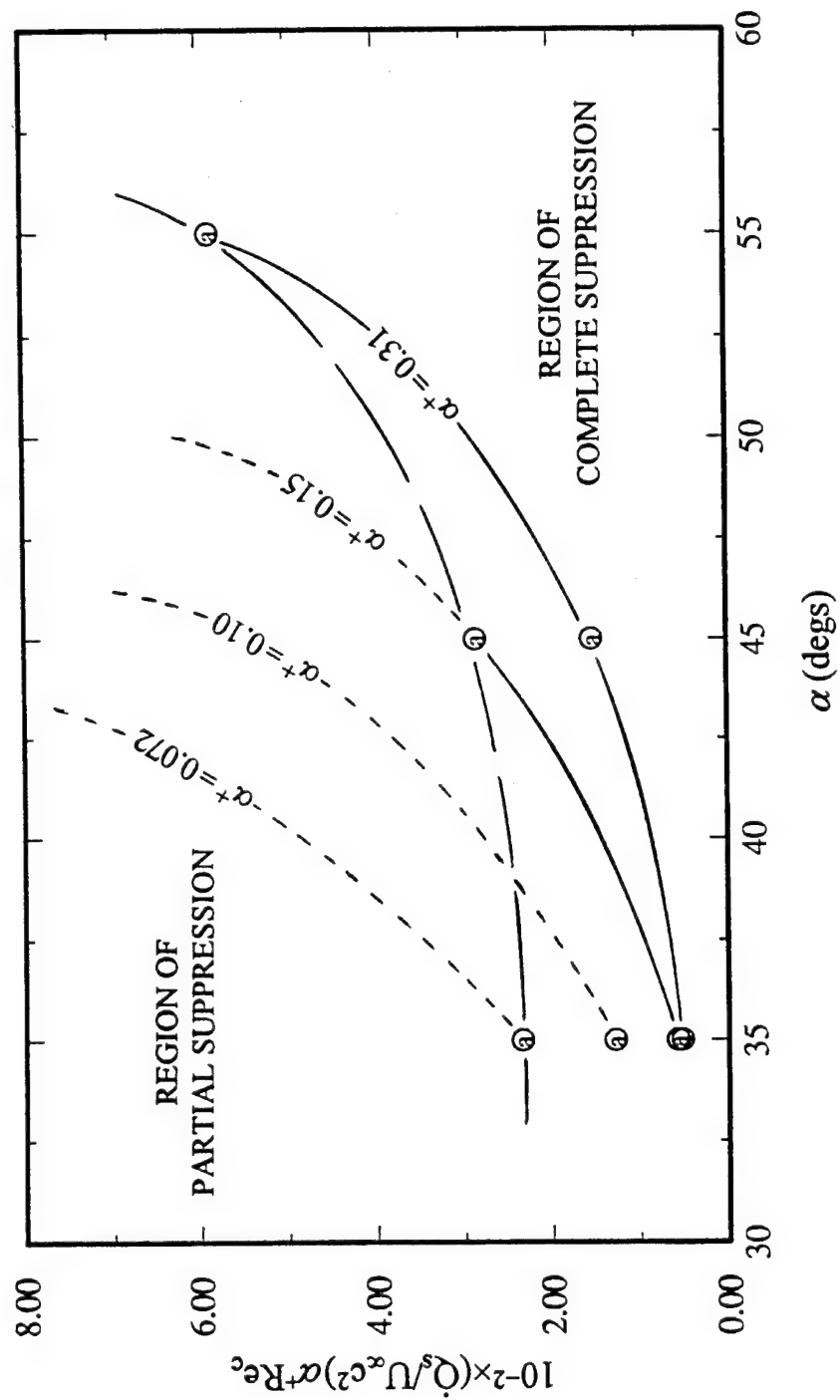
Fig. 16 Variation of suction flow rate for complete suppression of the DSV with angle of attack, for different pitch rates.

(a) $\alpha = 35^o$

$\triangledown - \alpha^+ = 0.072 - \triangledown$

REGION OF
COMPLETE SUPPRESSION

$\triangle - \alpha^+ = 0.10 - \triangle$

$\alpha^+ = 0.15$
$\alpha^+ = 0.31$

REGION OF
PARTIAL SUPPRESSION

$10^6 \times 1/Re_c$

$10^{-2} \times (\dot{Q}_s/U_\infty c^2)\alpha^+ Re_c$

0.00   8.00   16.00   24.00   32.00   40.00

0.00   0.60   1.20   1.80   2.40   3.00
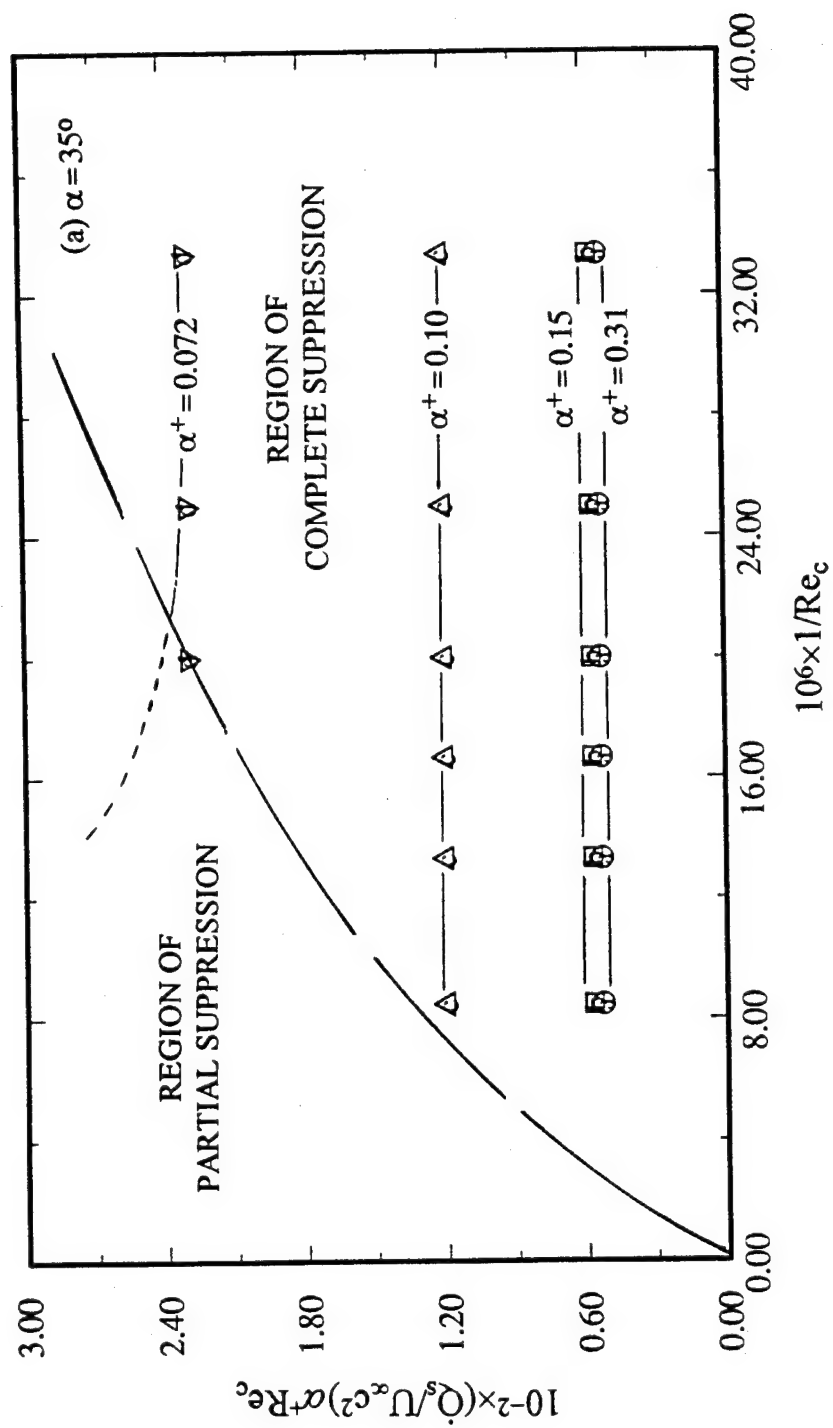
Fig. 17a   Variation of suction flow rate for complete suppression of the DSV with
Reynolds number, for different pitch rates ($\alpha = 35^o$).
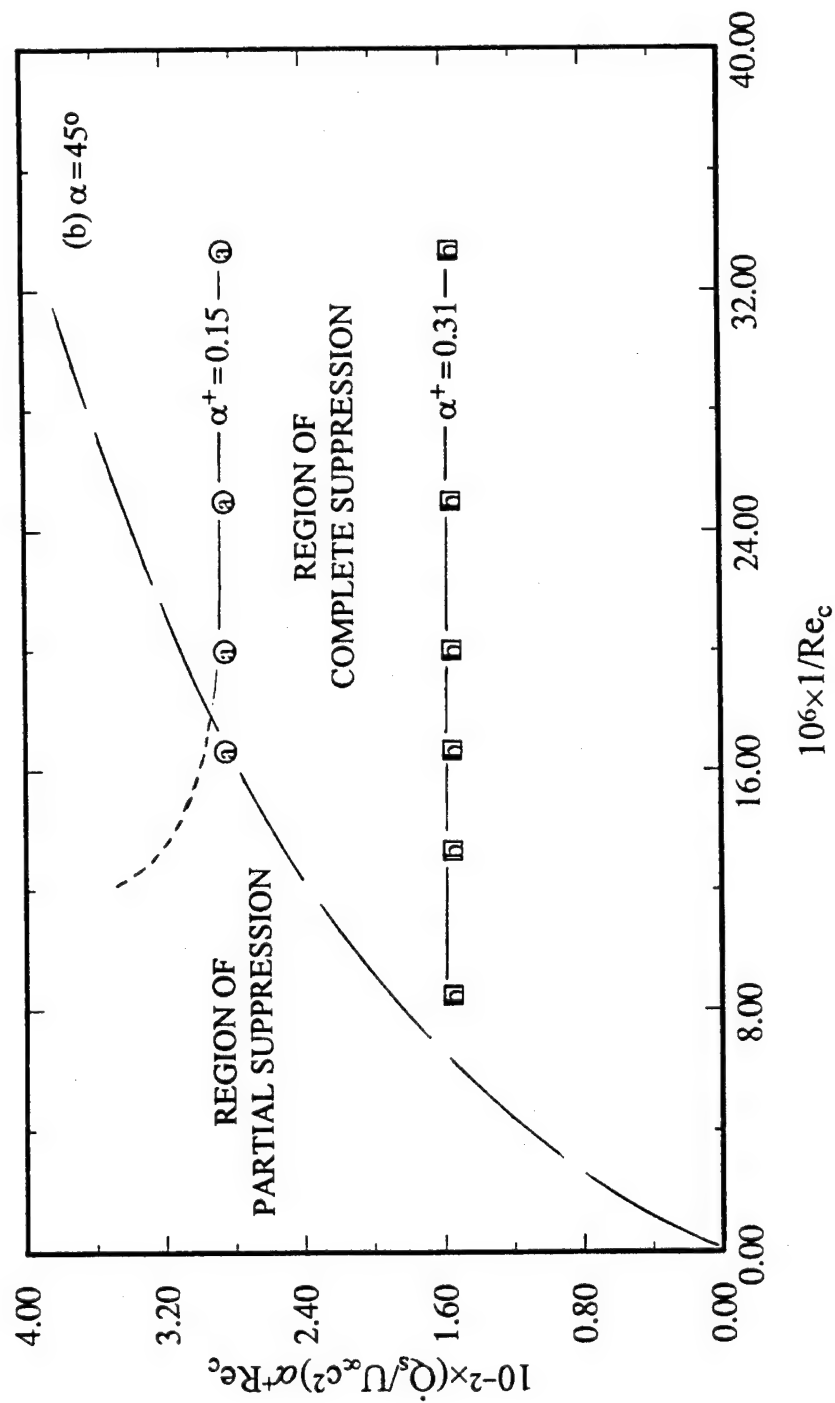
Fig. 17b Variation of suction flow rate for complete suppression of the DSV with Reynolds number, for different pitch rates ($\alpha = 45°$).
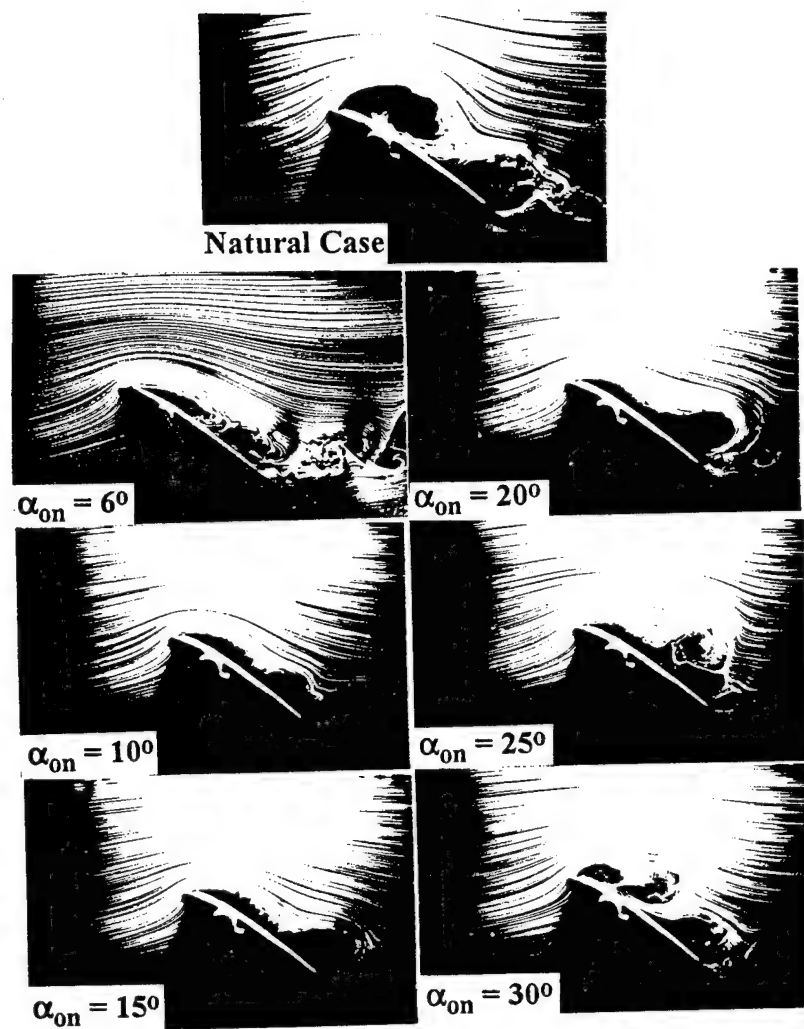
Fig. 18   Effect of suction activation time on flow development during airfoil pitch-up ($\alpha^+ = 0.15$, $Re_c = 30{,}000$, $Q_{nd} = 0.0127$, $\alpha = 35^o$, $\alpha_{off} = 38^o$).
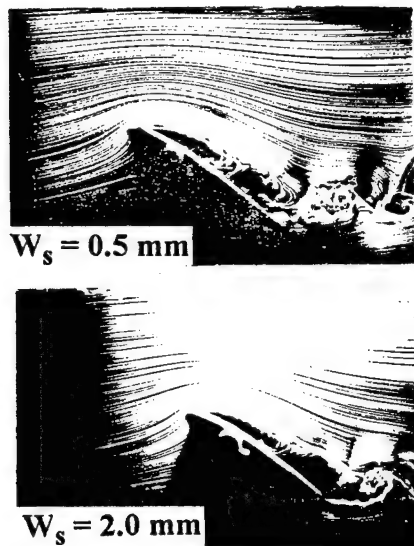
Fig. 19   Effect of suction slot width on suppression of the DSV (slot location 2% chord, $\alpha^+ = 0.15$, $Re_c = 30,000$, $Q_{nd}=0.0127$, $\alpha = 35^o$, $\alpha_{on} = 6^o$, $\alpha_{off} = 38^o$).
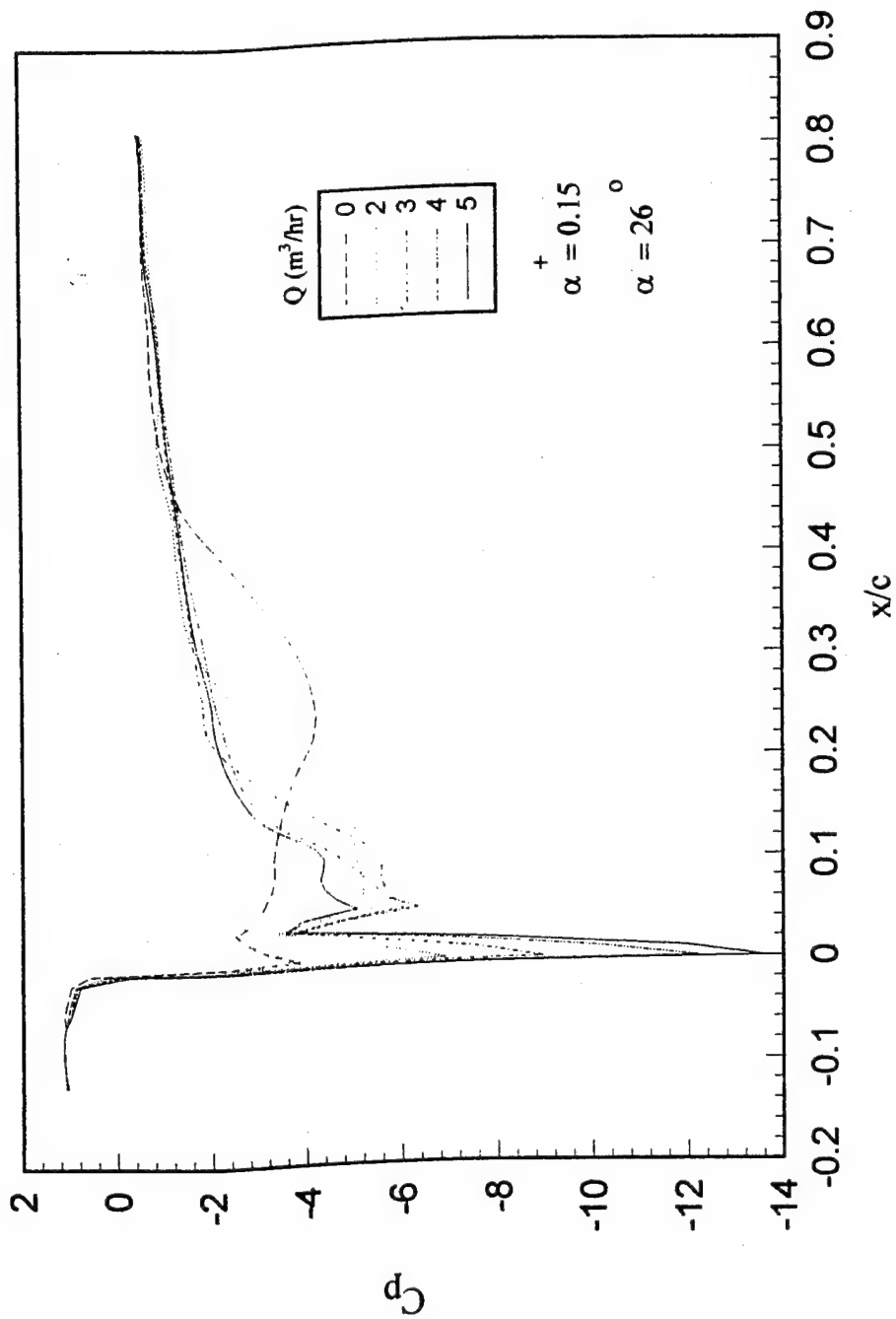
Fig. 20 Variation of chordwise surface-pressure coefficient with suction ($\alpha^+ = 0.15$, $\alpha = 26°$)
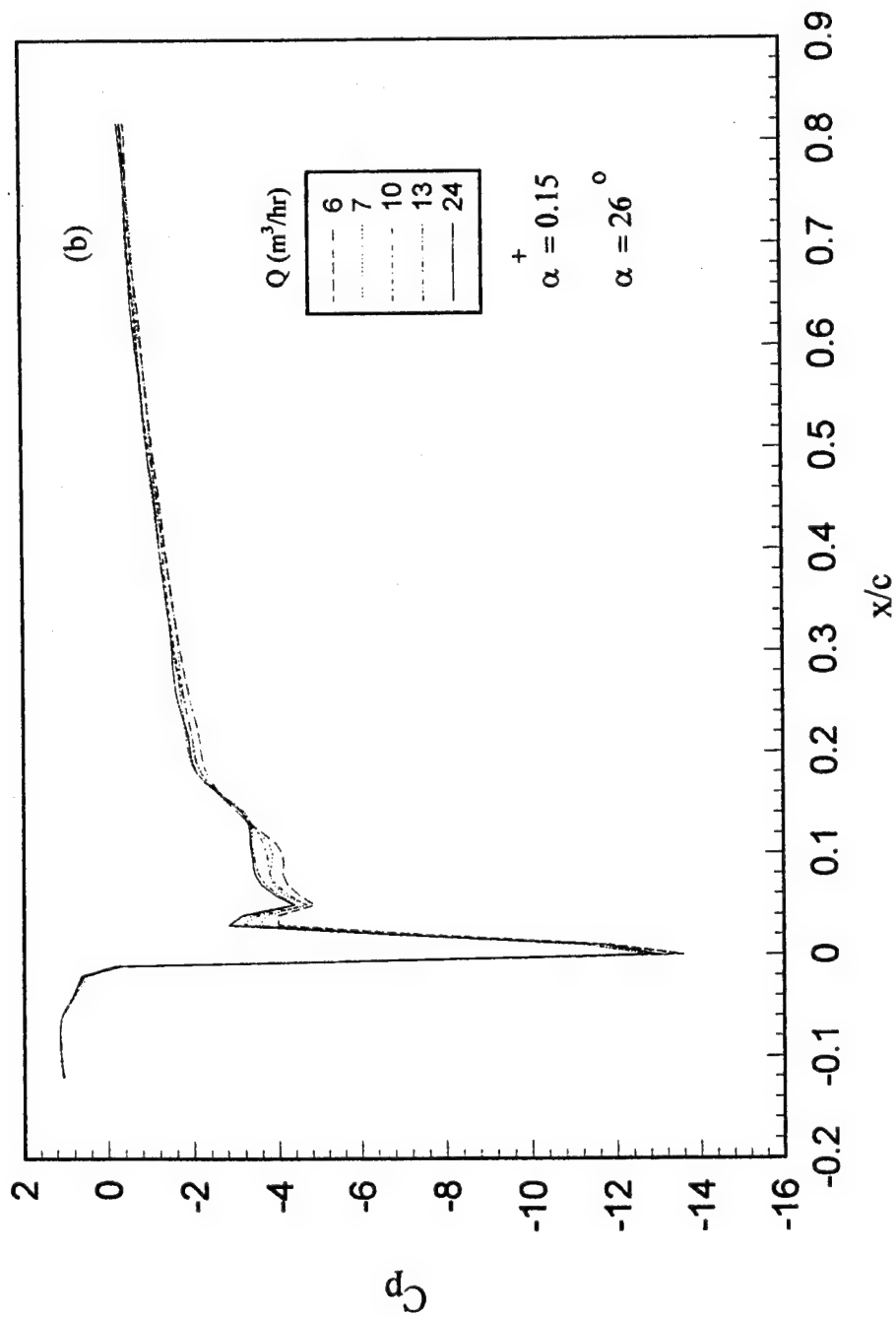
Fig. 20 (cont.) Variation of chordwise surface-pressure coefficient with suction ($\alpha^+ =$ 0.15, $\alpha = 26°$)
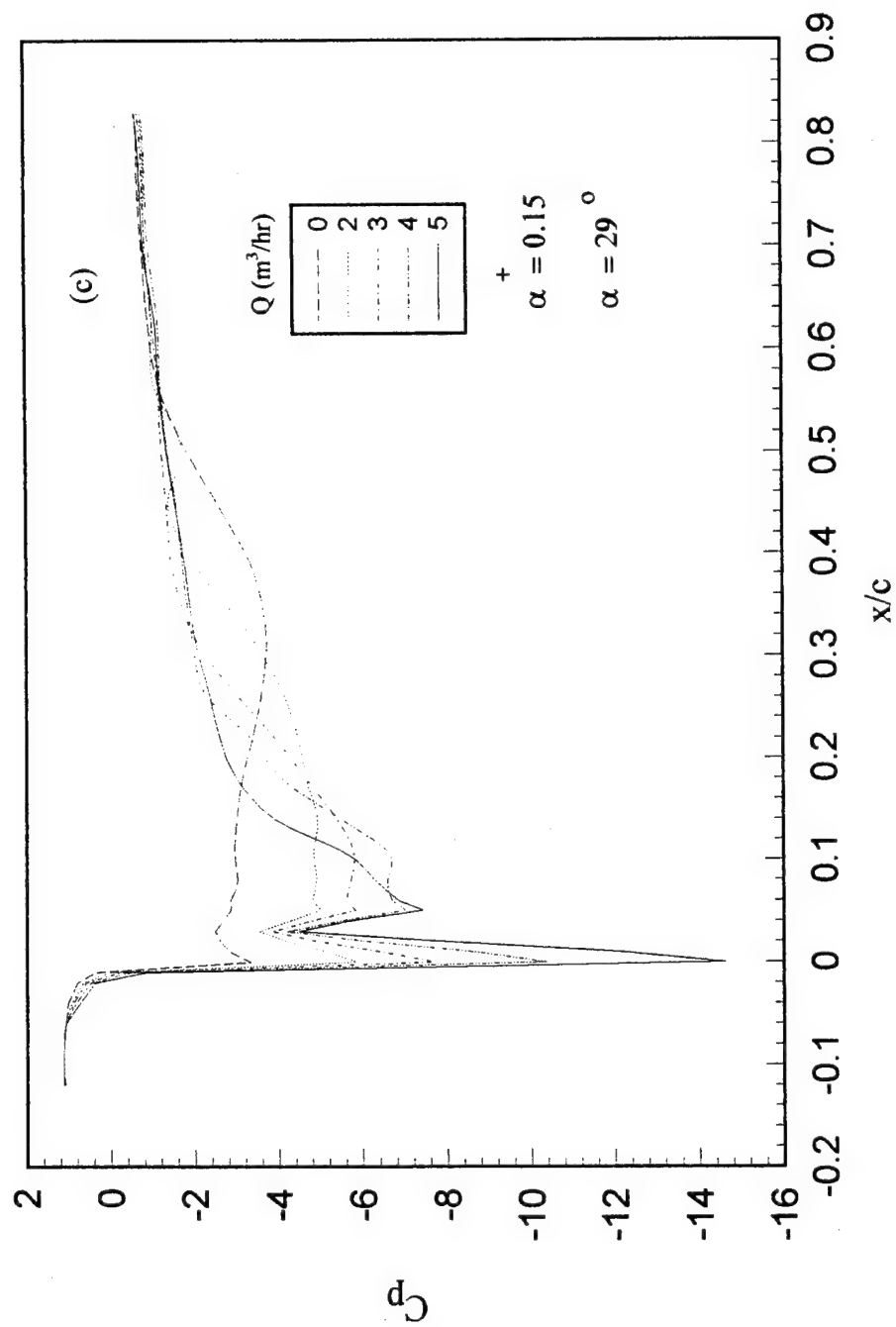
Fig. 21 Variation of chordwise surface-pressure coefficient with suction ($\alpha^+ = 0.15$, $\alpha = 29°$)
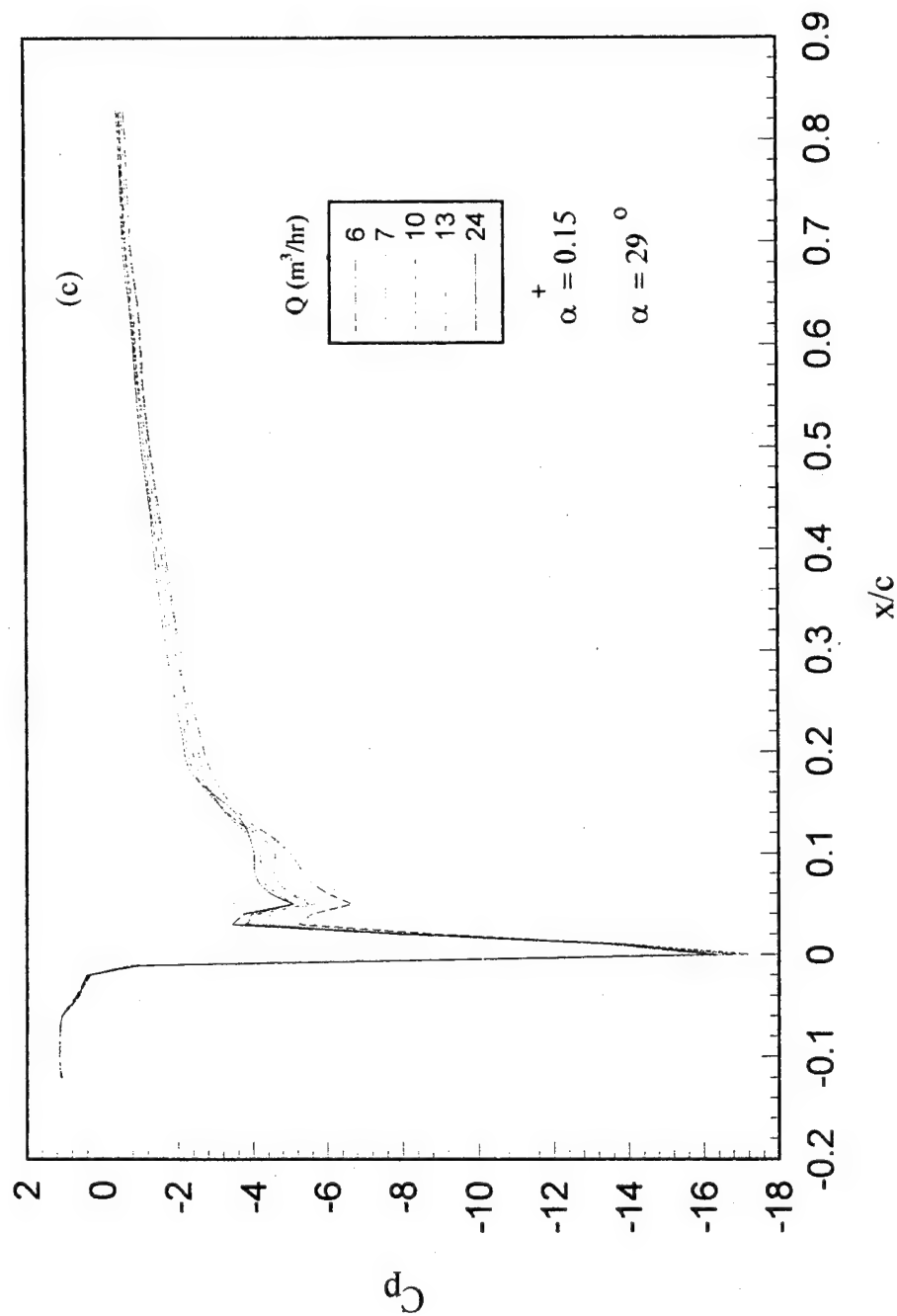
Fig. 21 (cont.) Variation of chordwise surface-pressure coefficient with suction ($\alpha^+ =$ 0.15, $\alpha = 29°$)
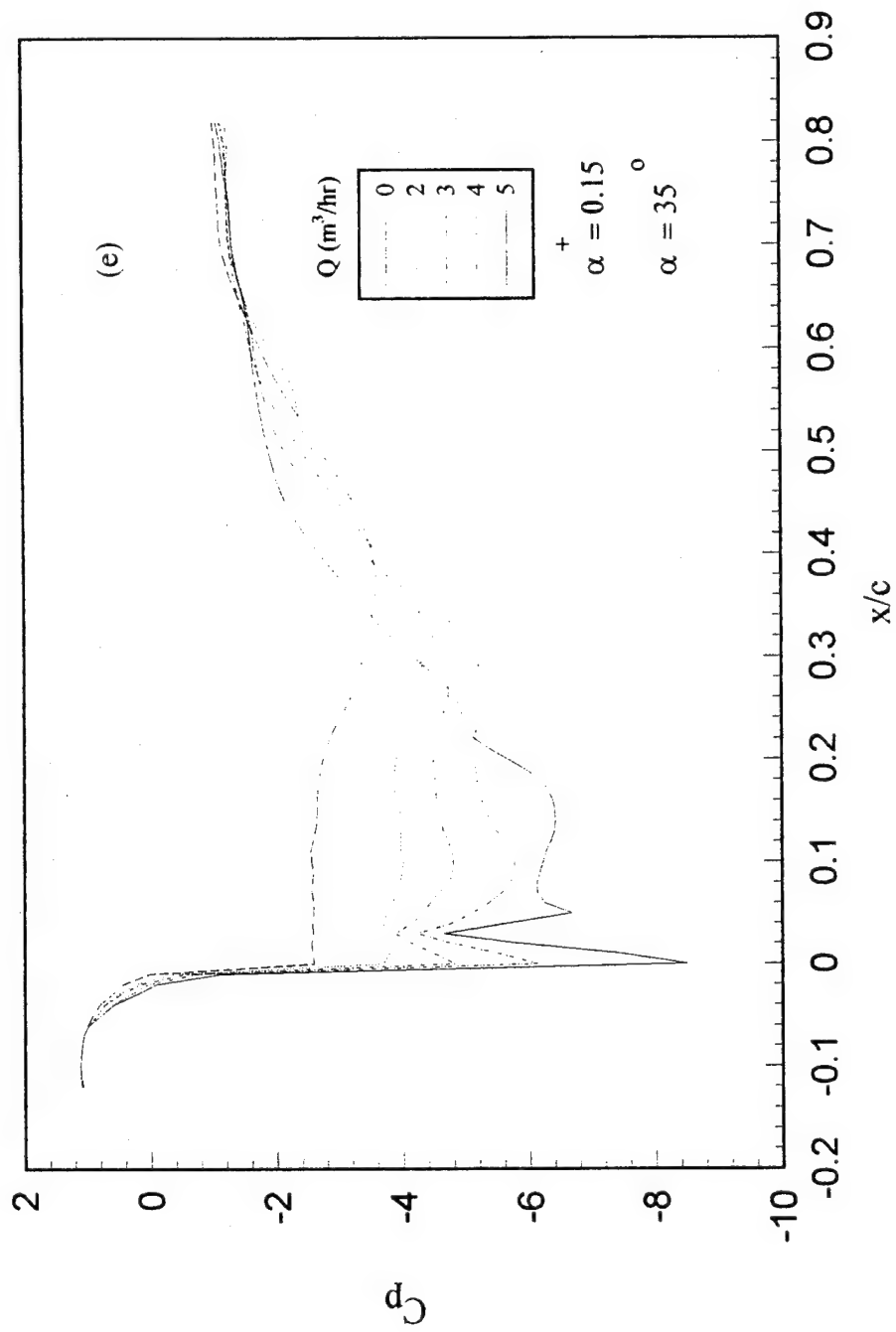
Fig. 22 Variation of chordwise surface-pressure coefficient with suction ($\alpha^+ = 0.15$, $\alpha = 35°$)
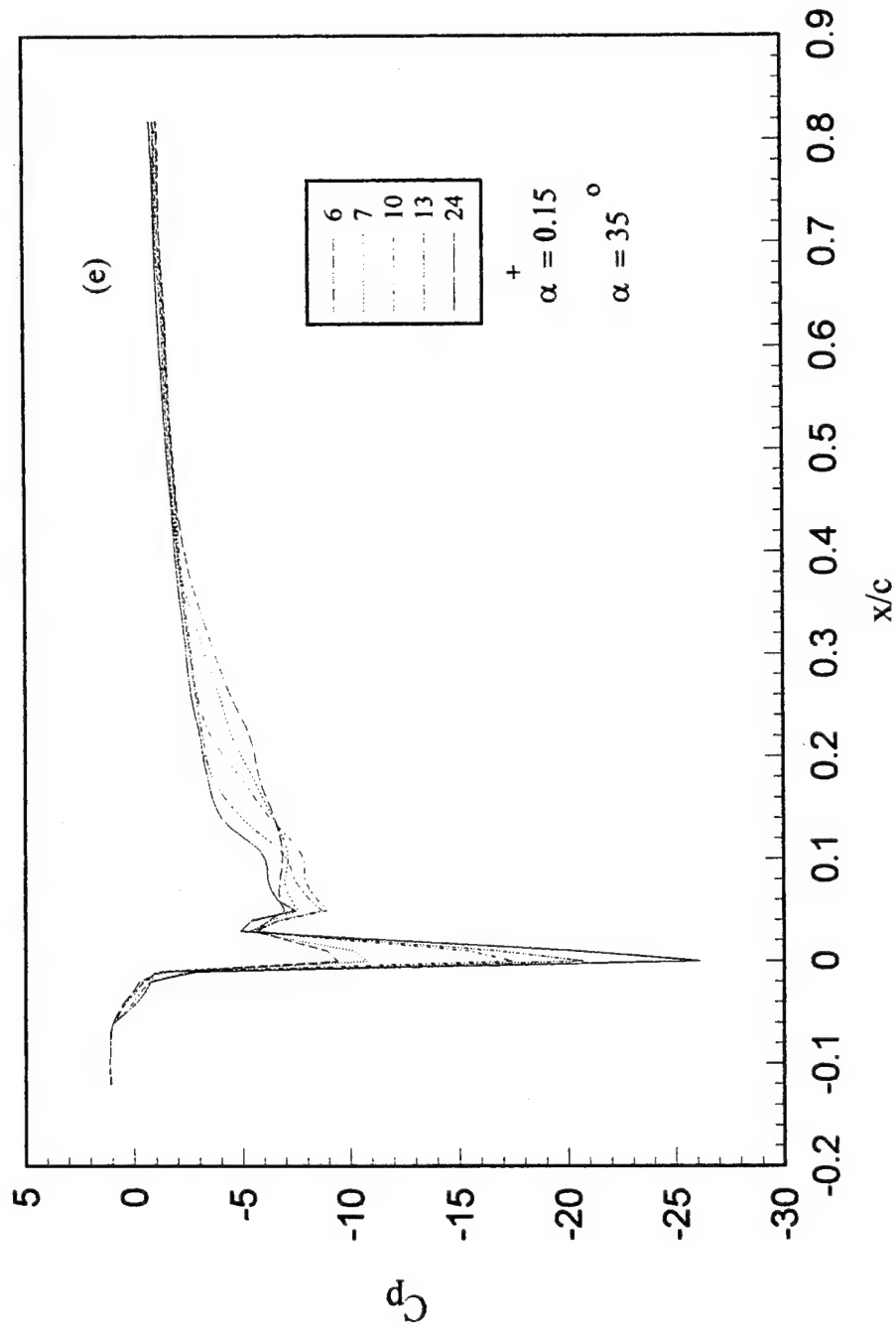
Fig. 22 (cont.) Variation of chordwise surface-pressure coefficient with suction (α^+ = 0.15, $\alpha = 35°$)
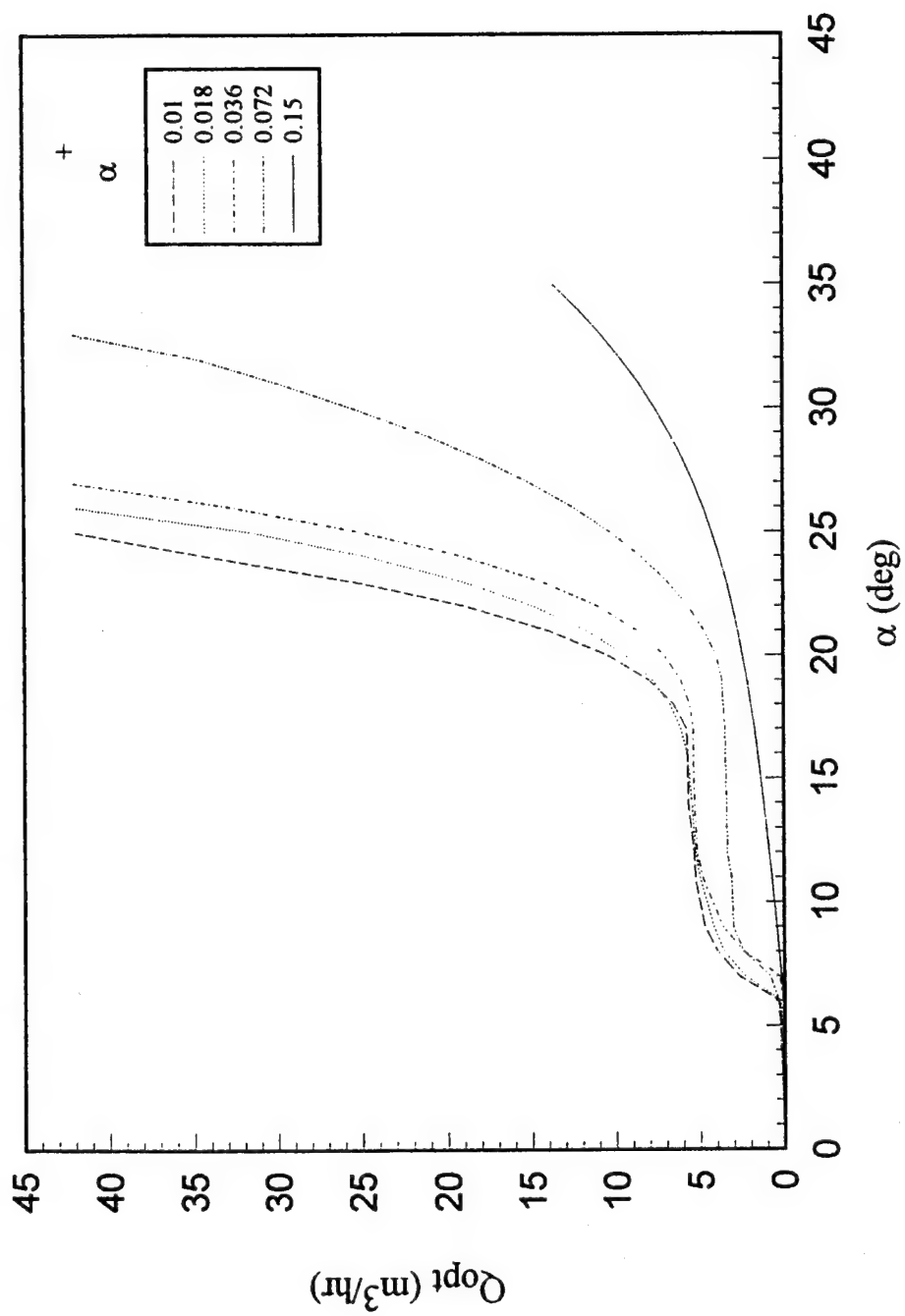
Fig. 23 Variation of optimum suction for suppression of the dynamic-stall vortex
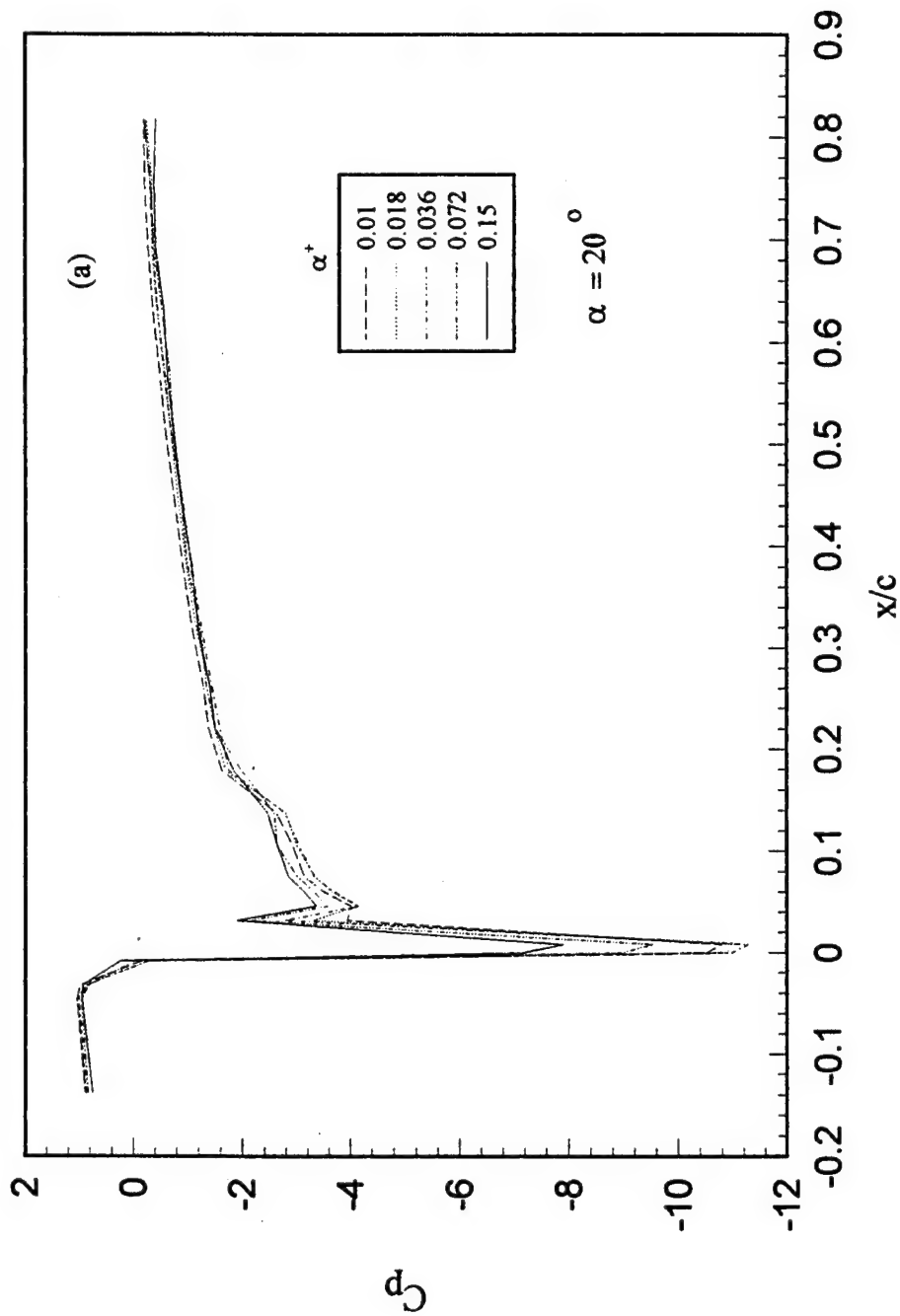
Fig. 24 Pressure distributions at different pitch rates with a suppressed dynamic-stall vortex
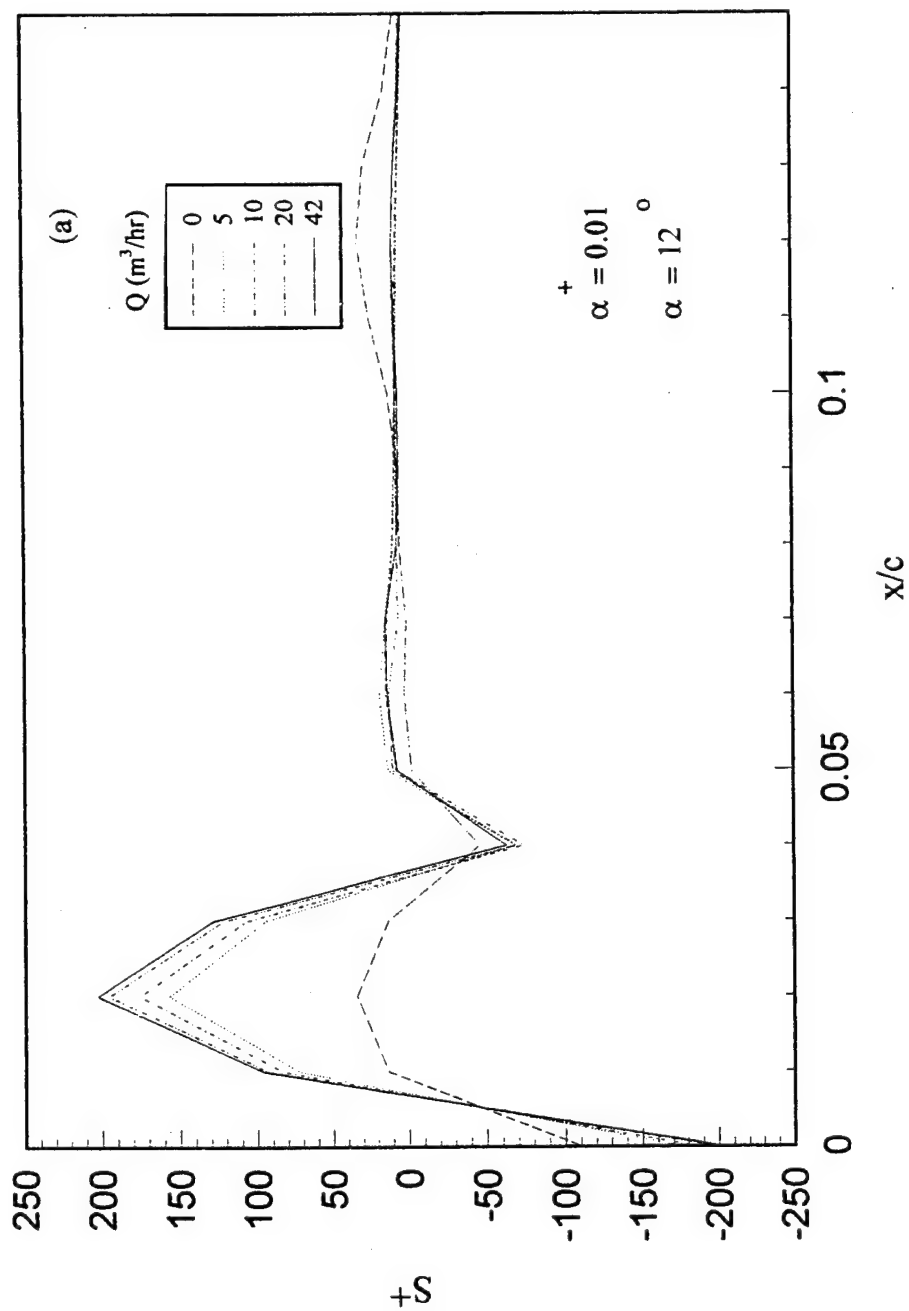
Fig. 25(a) Vorticity-flux distributions at different suction flow rates, $\alpha^+ = 0.01$ and $\alpha = 12°$
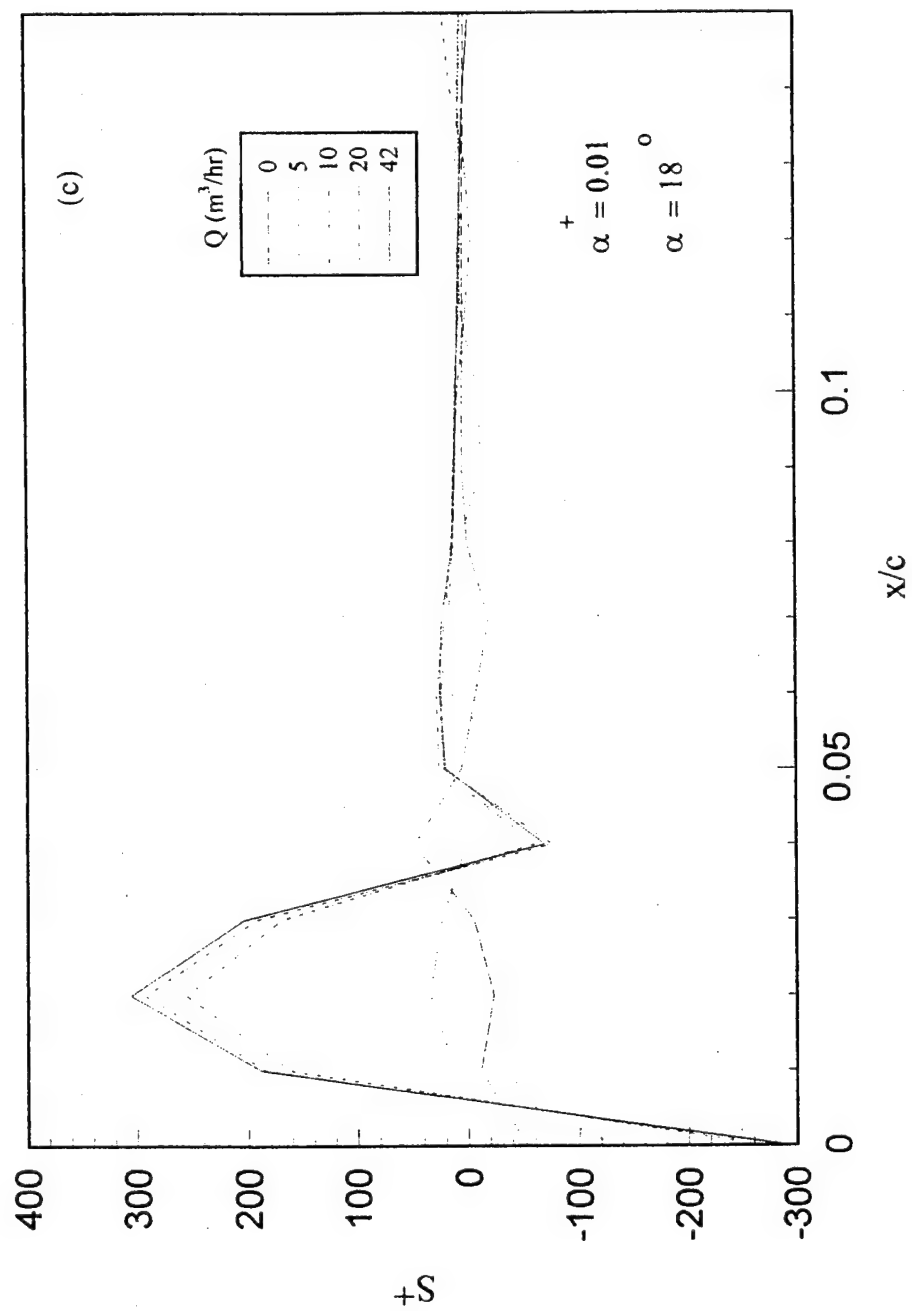
Fig. 25(b) Vorticity-flux distributions at different suction flow rates, $\alpha^+ = 0.01$ and $\alpha = 18°$

(a)

Static Stall

α^+

△ 0.01
○ 0.018
▽ 0.036
⋄ 0.072
□ 0.15
── steady

C_l

α (deg)
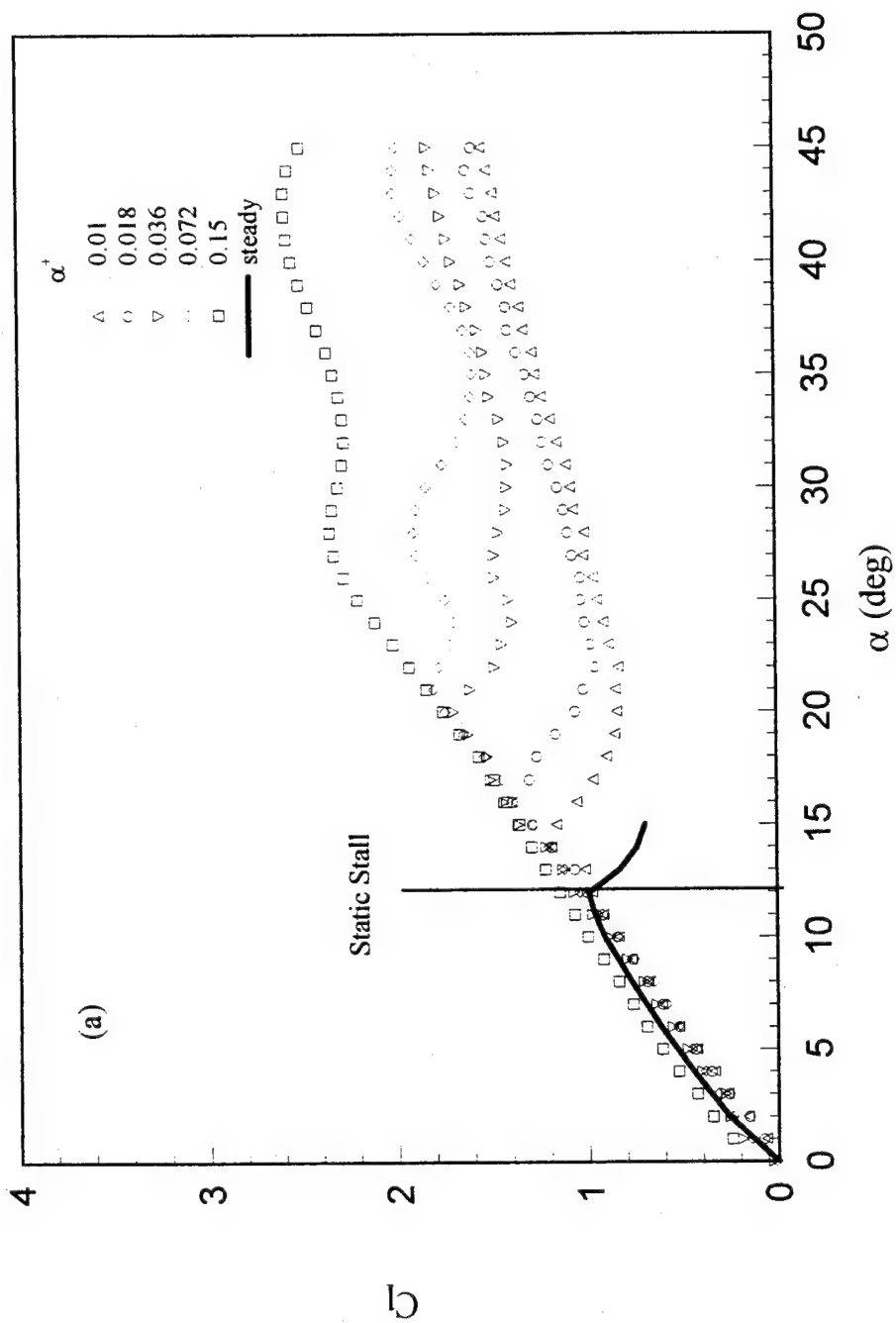
Fig. 26 Variation of lift coefficient with pitch rate
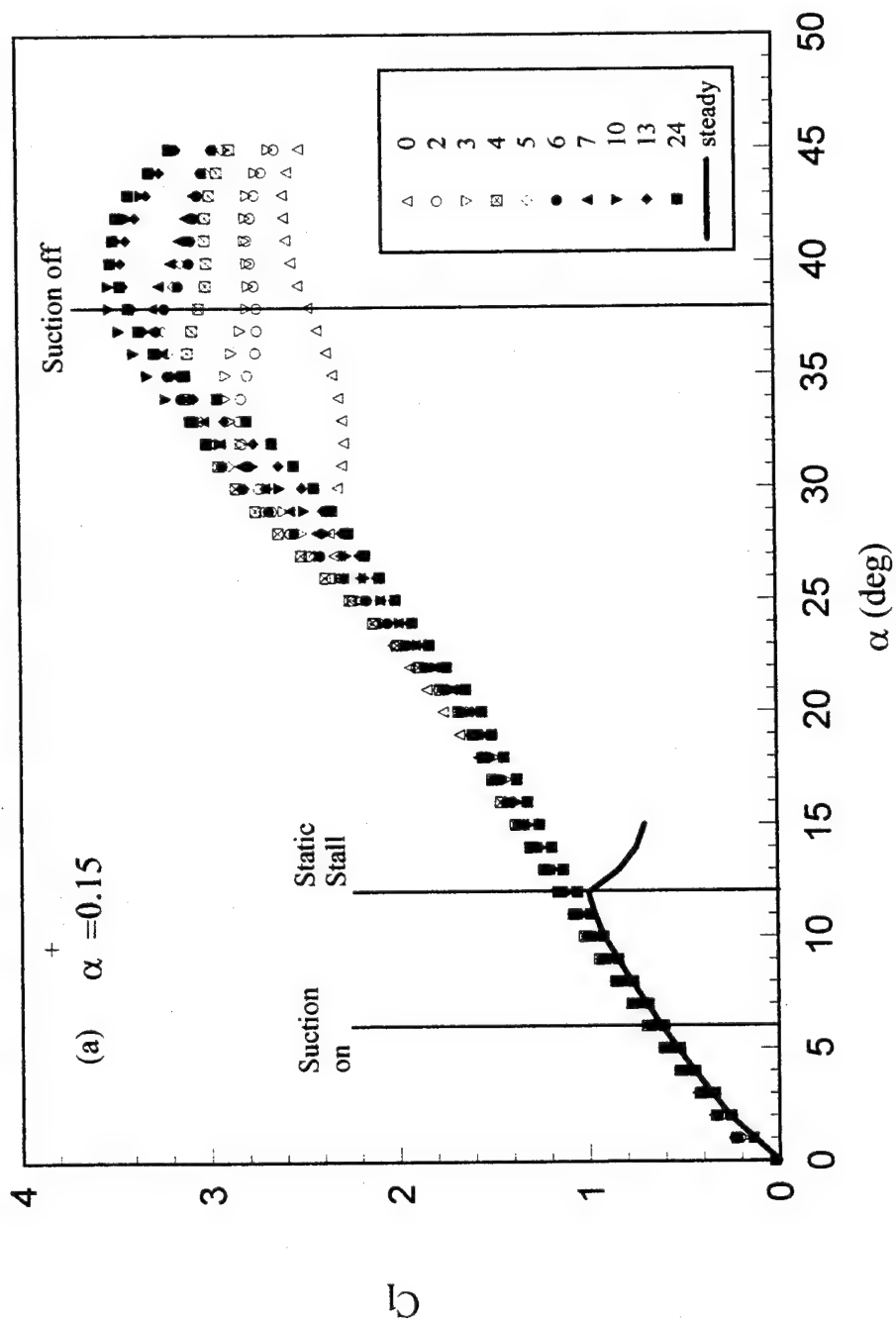
Fig. 27(a) Effect of suction on the lift coefficient $\alpha^+ = 0.15$
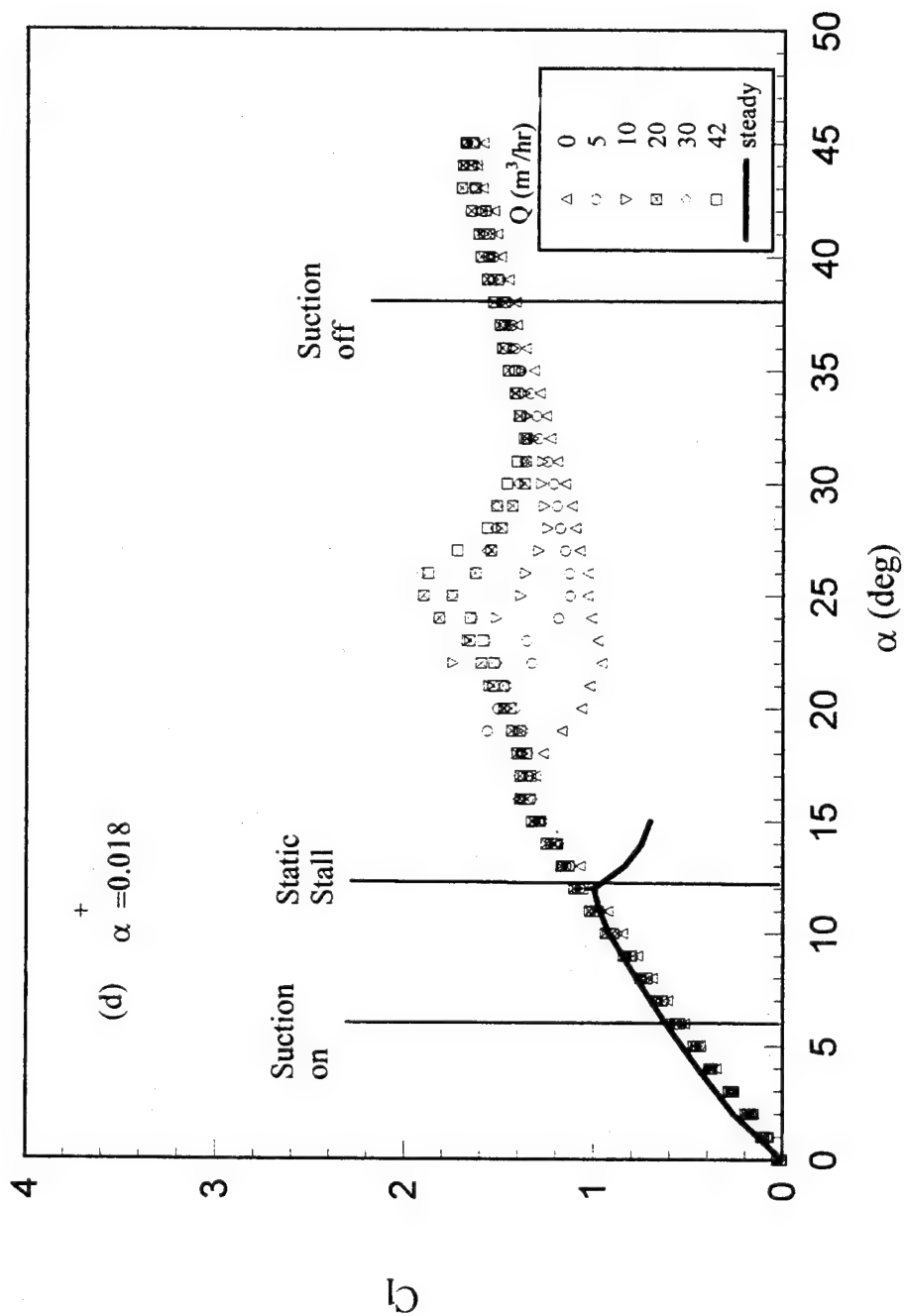
Fig. 27(b) Effect of suction on the lift coefficient $\alpha^+ = 0.018$
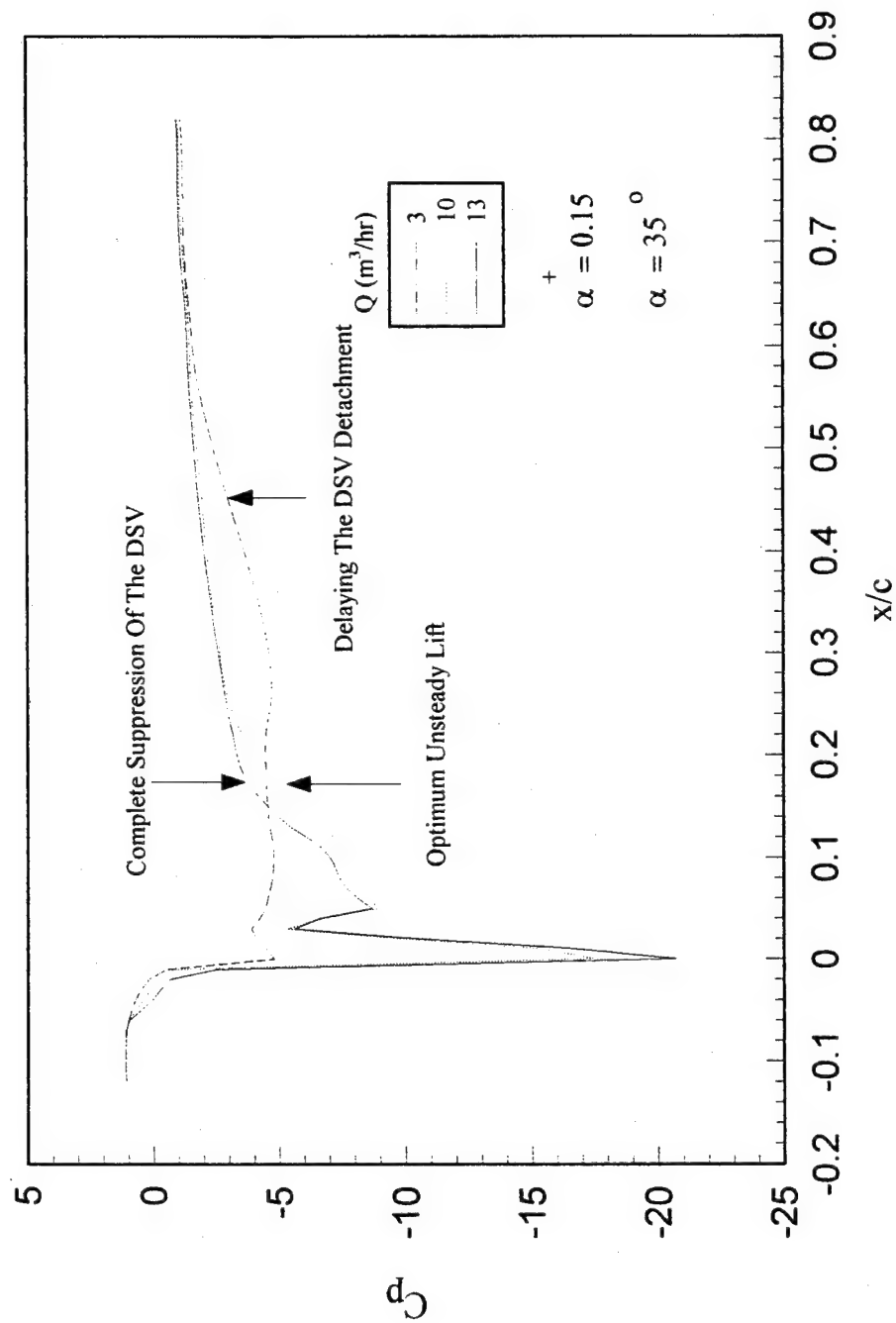
Fig. 28 Surface-pressure distributions for optimum flow state, $\alpha^+ = 0.15$, $\alpha = 35°$
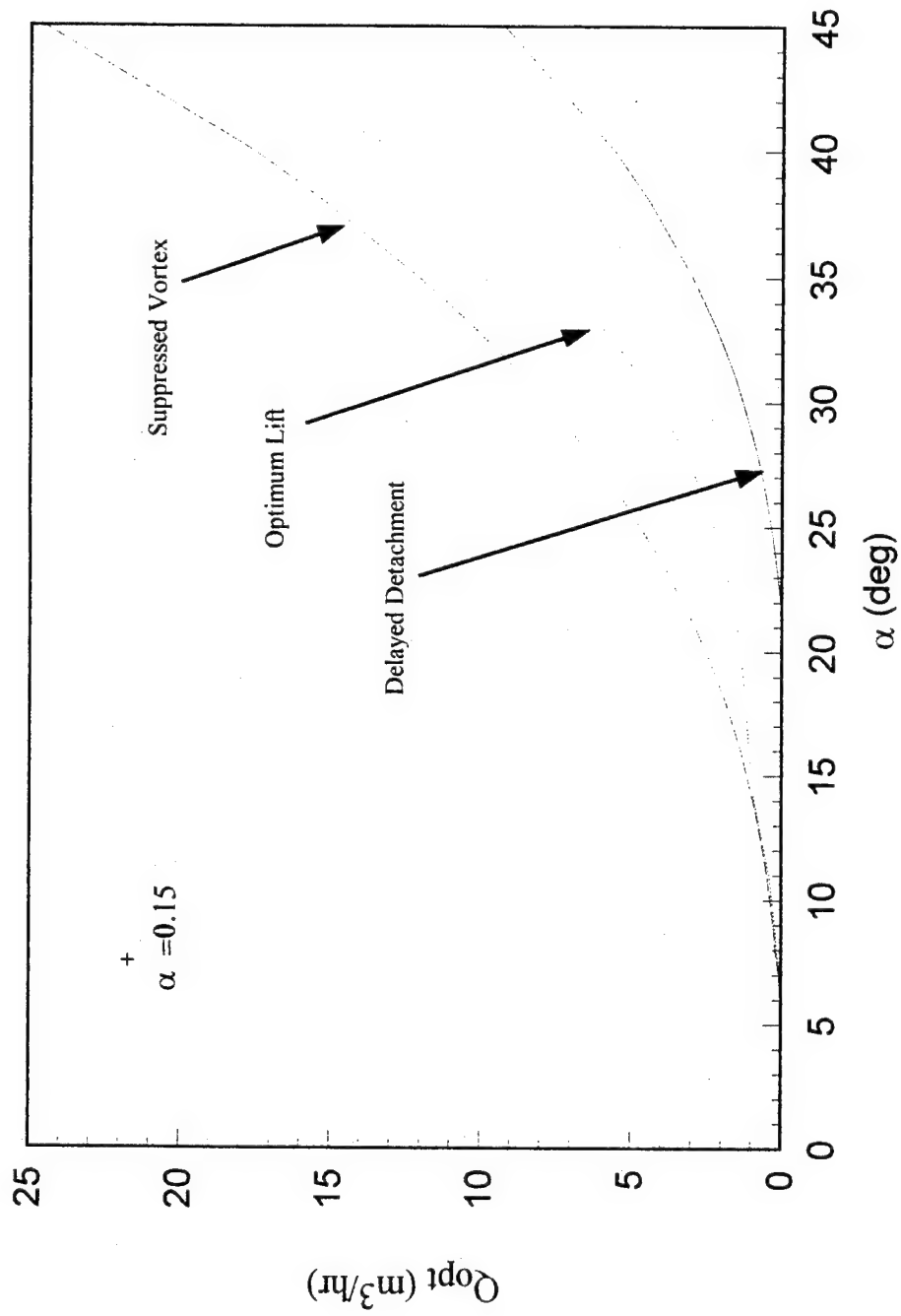
Fig. 29 Optimum suction flow rates for different objectives, $\alpha^+ = 0.15$
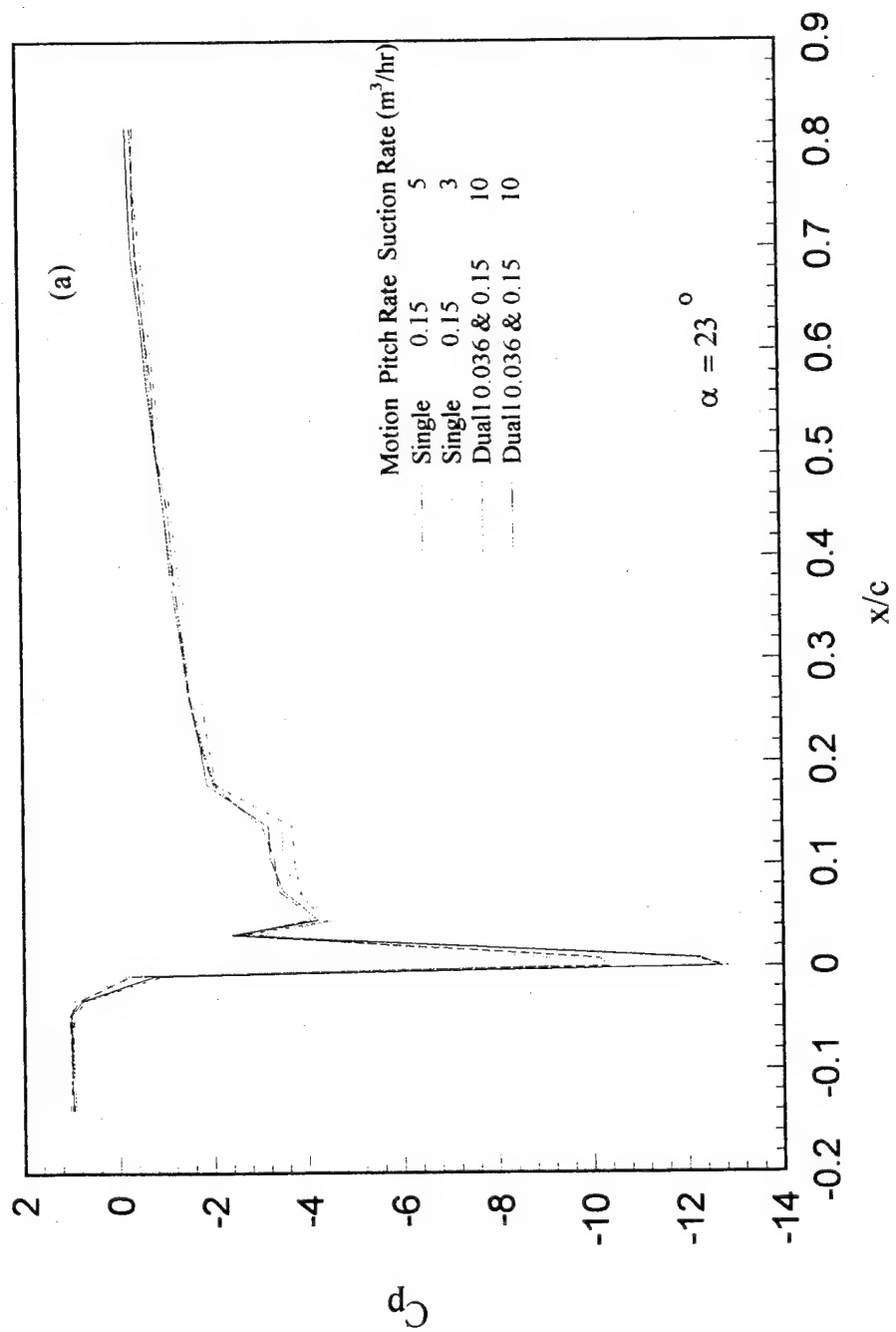
Fig. 30(a) Surface-pressure distributions for dual-ramp and single ramp motions, α = 23°
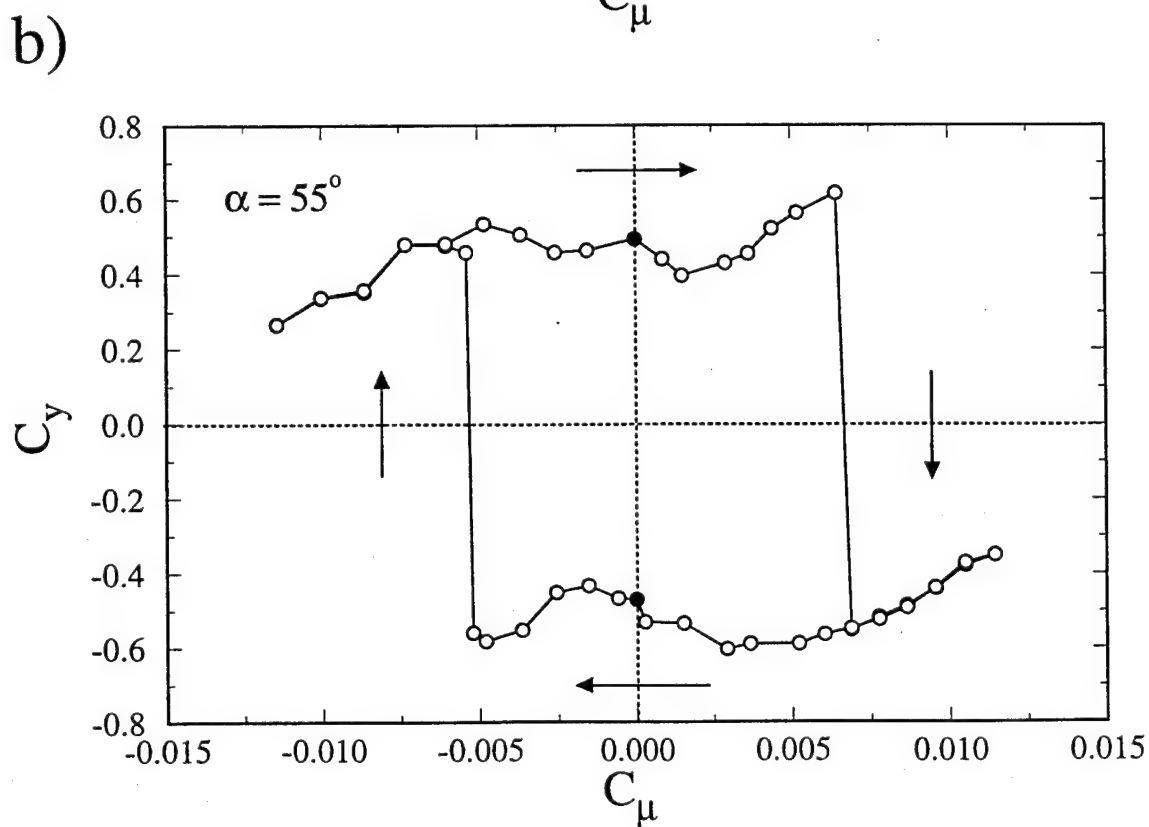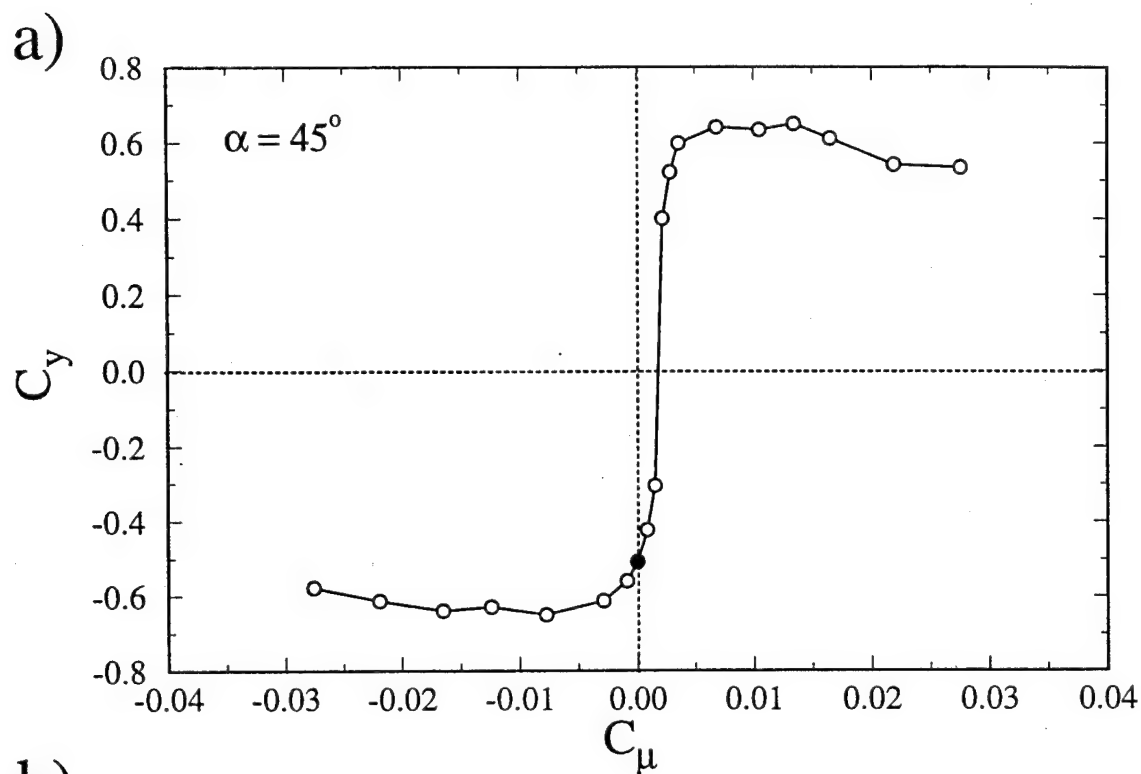
Fig. 31 The effect of forcing on the sectional side force coefficient. (a) $\alpha=45^{\circ}$; (b) $\alpha=55^{\circ}$.
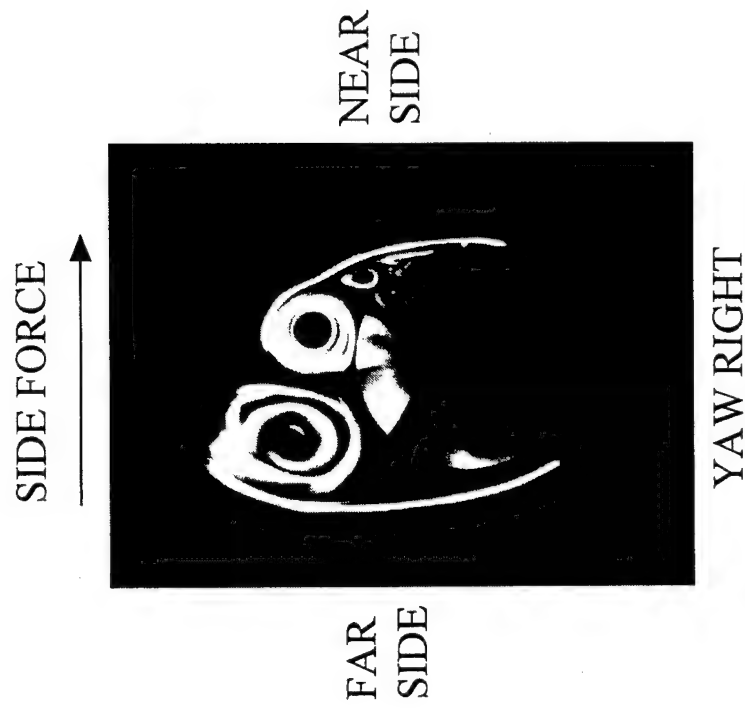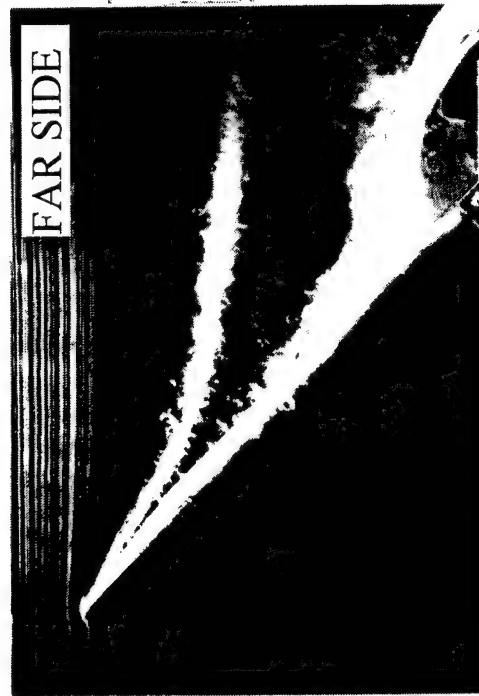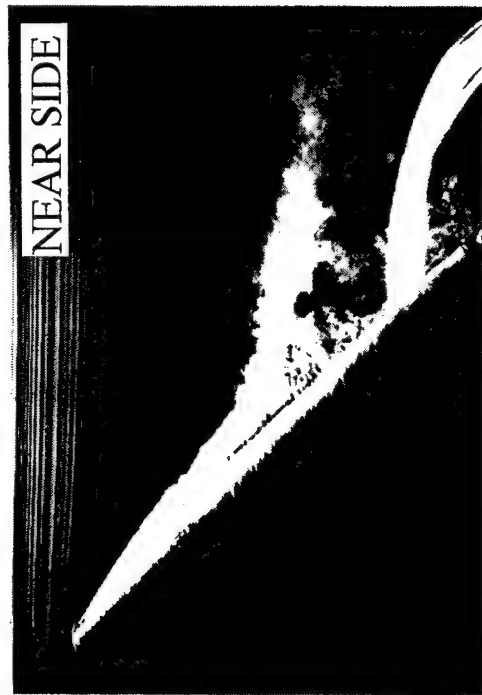
Fig. 32   Vortex configruation in its natural asymmetric state. (a) smoke-wire flow visualization; (b) pressure coefficient around the aziumuth of the model; (c) velocity. contours.

b)

c)
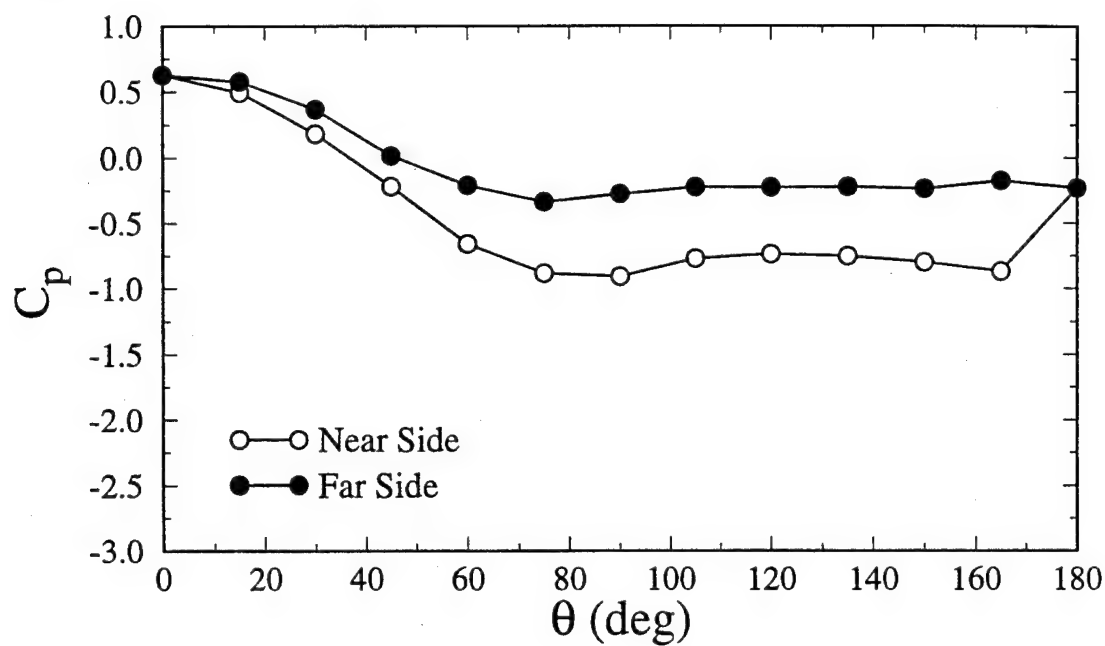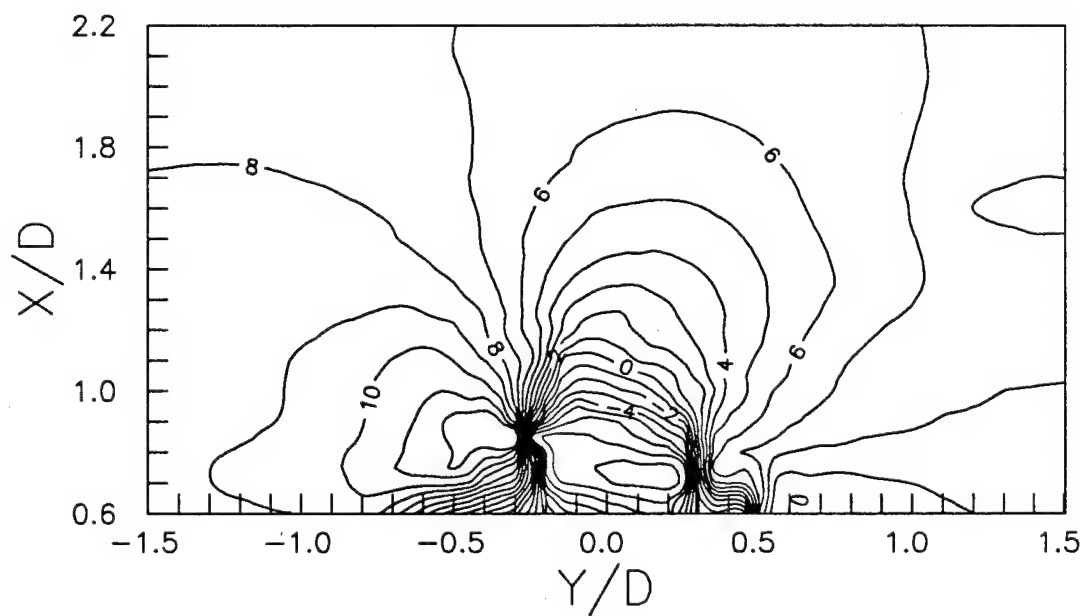
Fig. 32 (cont.)
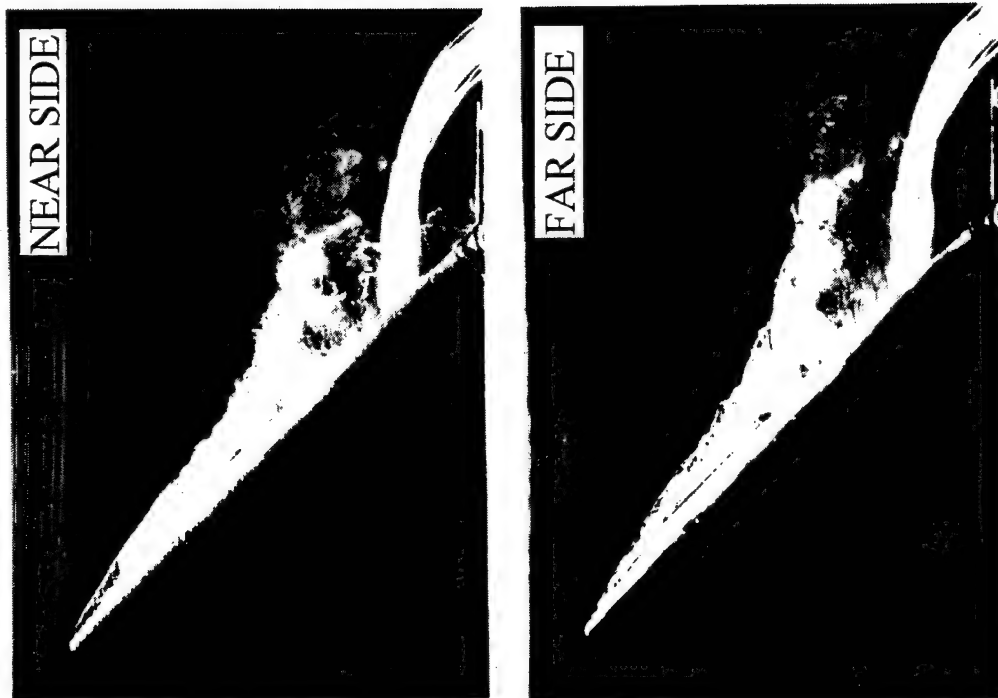
Fig. 33   Using control the forebody vortices are moved to a symmetric state. (a) smoke-wire flow visualization; (b) pressure coefficient around the aziumuth of the model; (c) velocity contours.

b)

c)

Fig. 33 (cont.)

SIDE FORCE

NEAR SIDE

FAR SIDE

YAW LEFT

BOTH SIDES

FAR SIDE
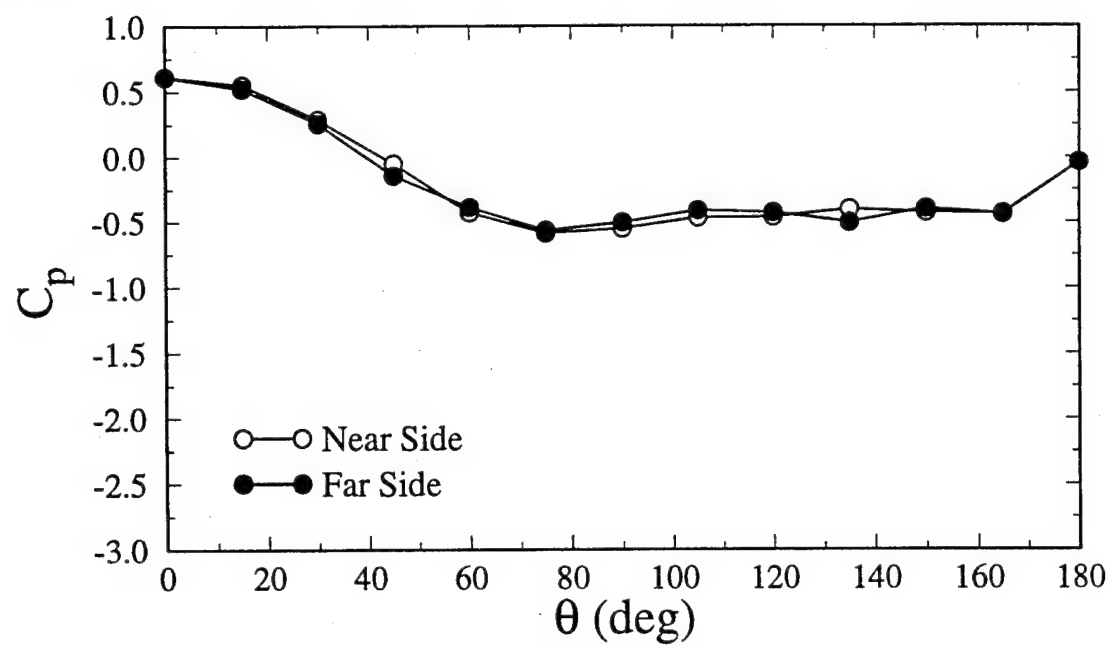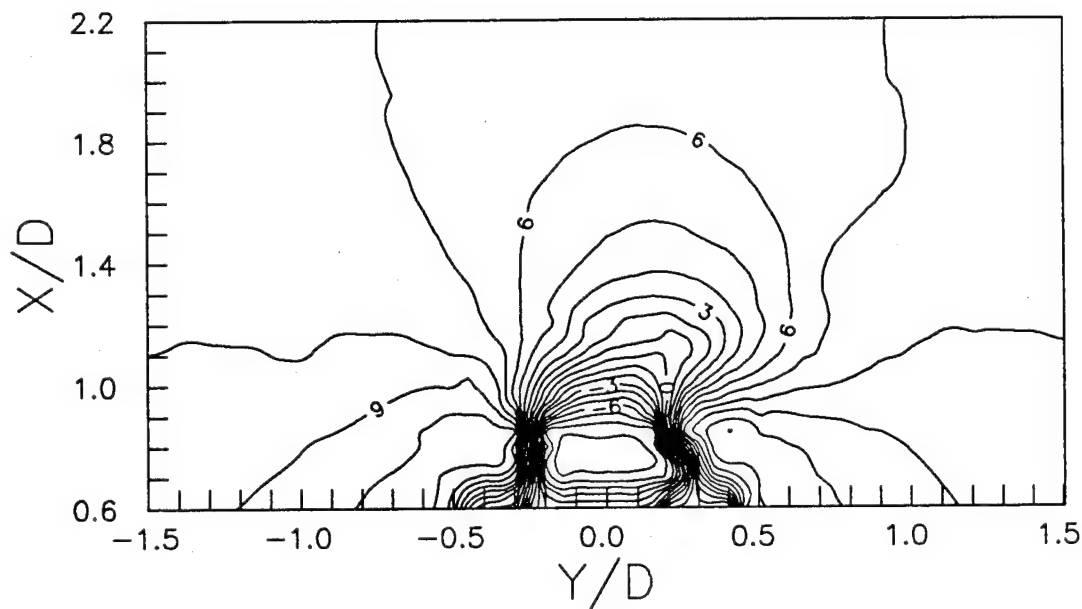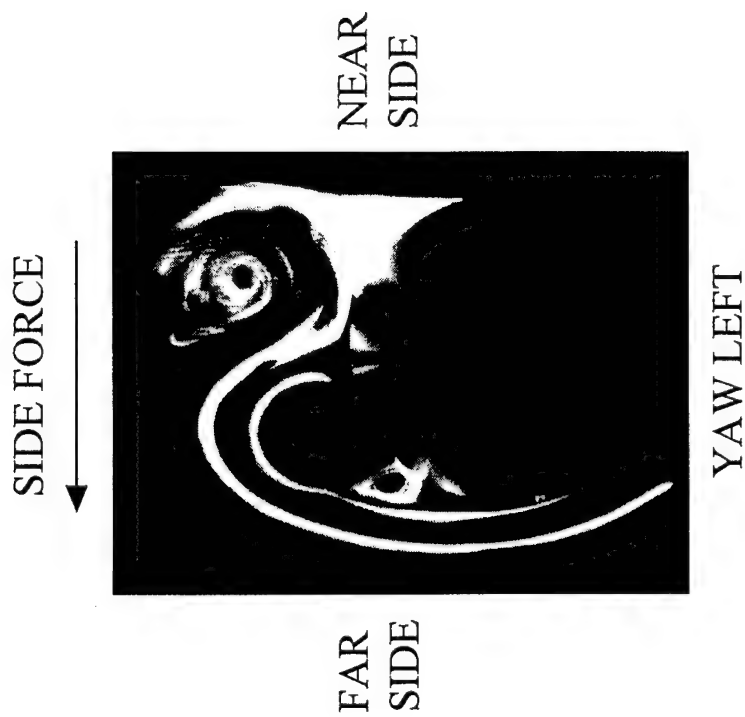
Fig. 34 Increasing the control amplitude move the forebody vortices to a configuration opposite to the natural case. (a) smoke-wire flow visualization; (b) pressure coefficient around the aziumuth of the model; (c) velocity contours.

b)
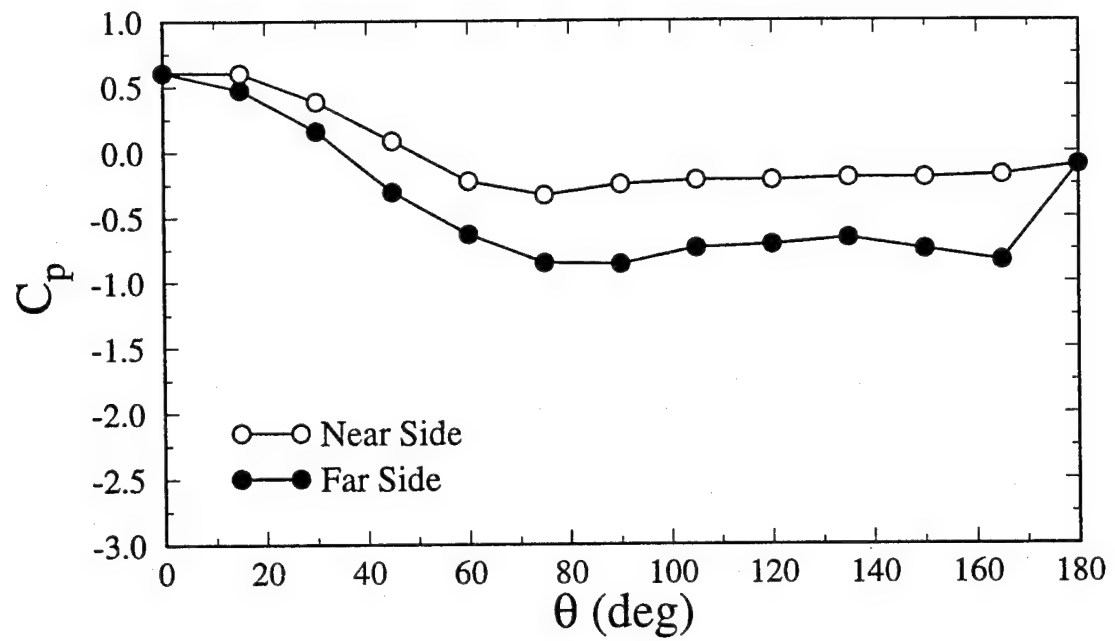
c)
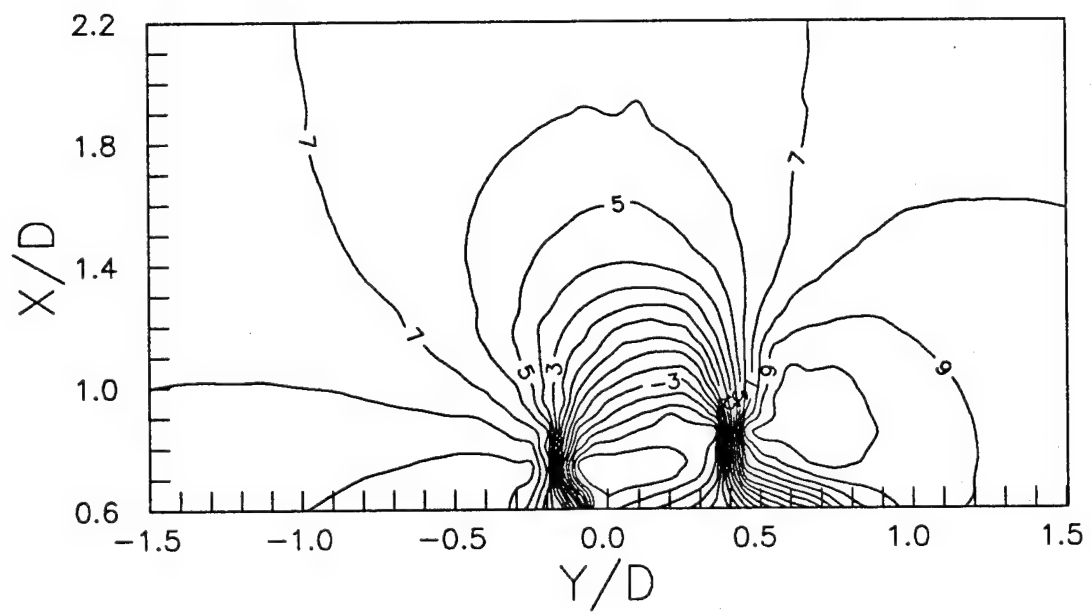
Fig. 34 (cont.)
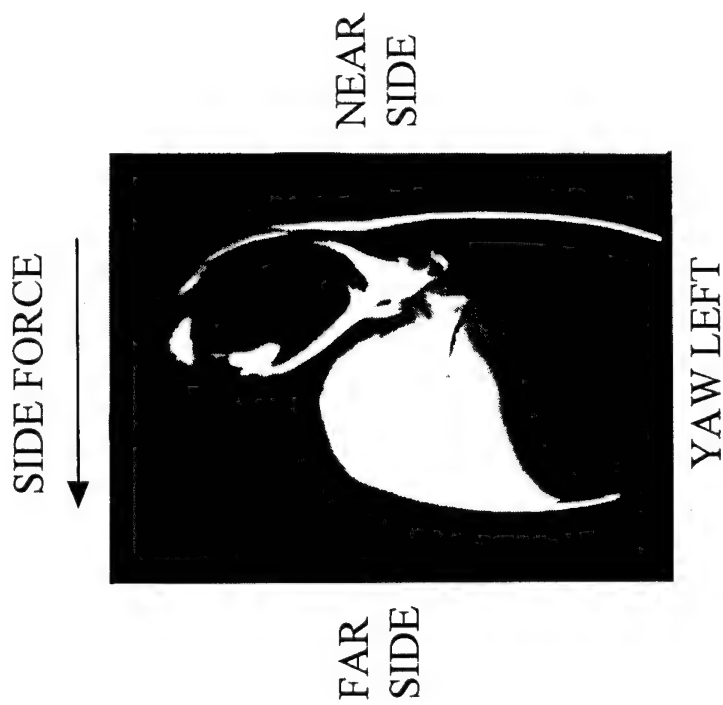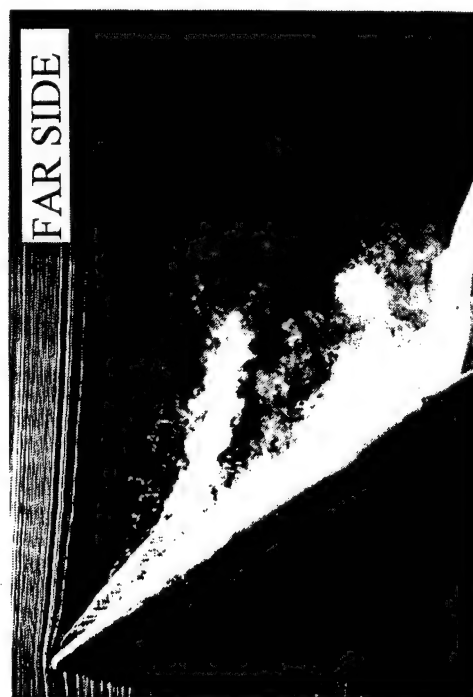
Fig. 35 Bistable behavior of forebody vortices in the yaw left configuration. (a) flow visualization; (b) pressure coefficient around the azimuth.
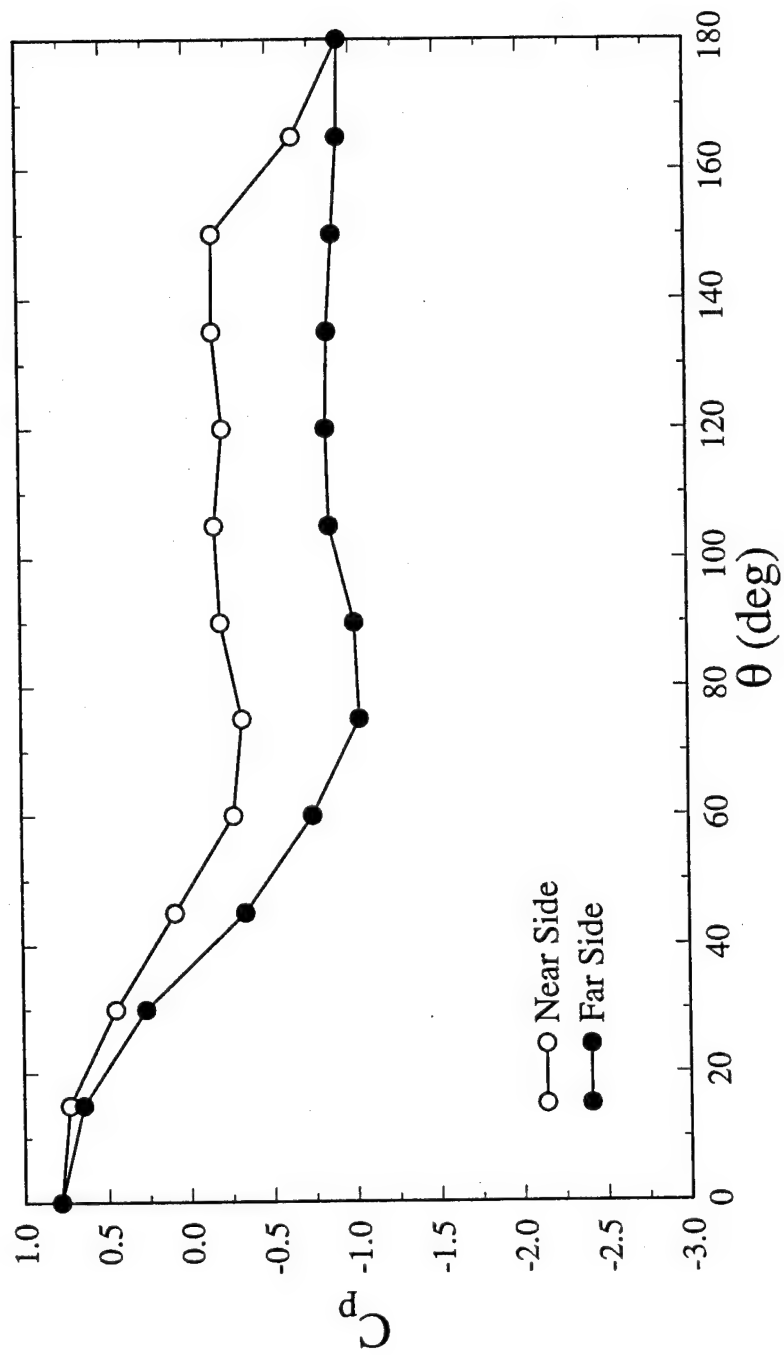
Fig. 35 (cont.)
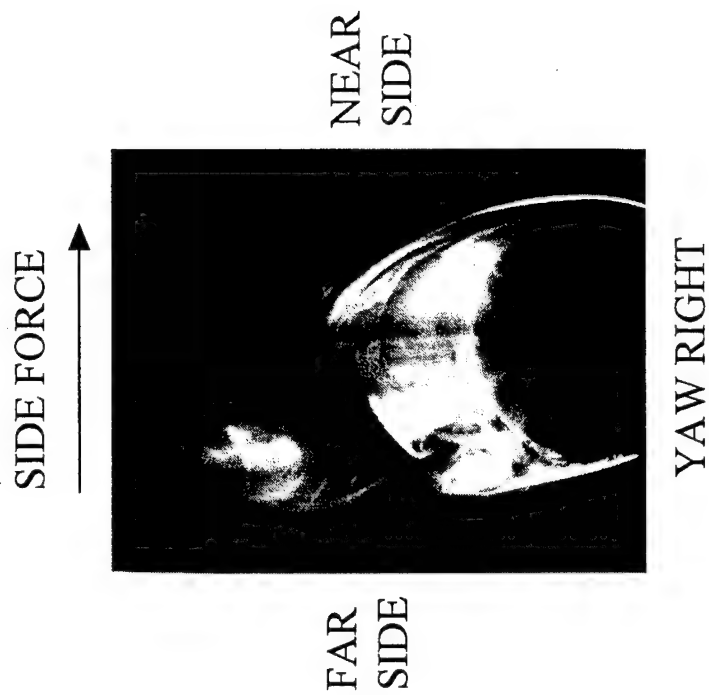
Fig. 36   Bistable behavior of forebody vortices in the yaw right configuration. (a) flow visualization; (b) pressure coefficient around the azimuth.
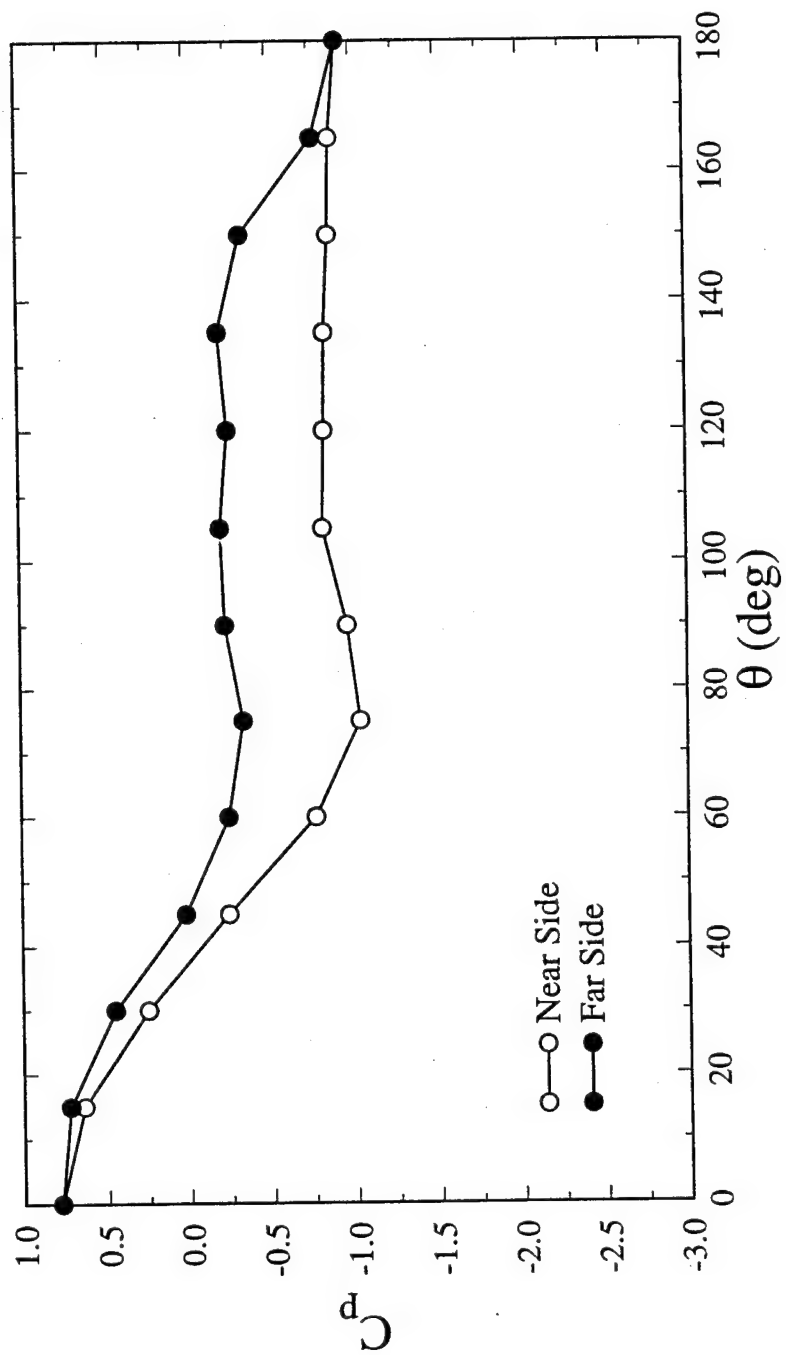
Fig. 36 (cont.)
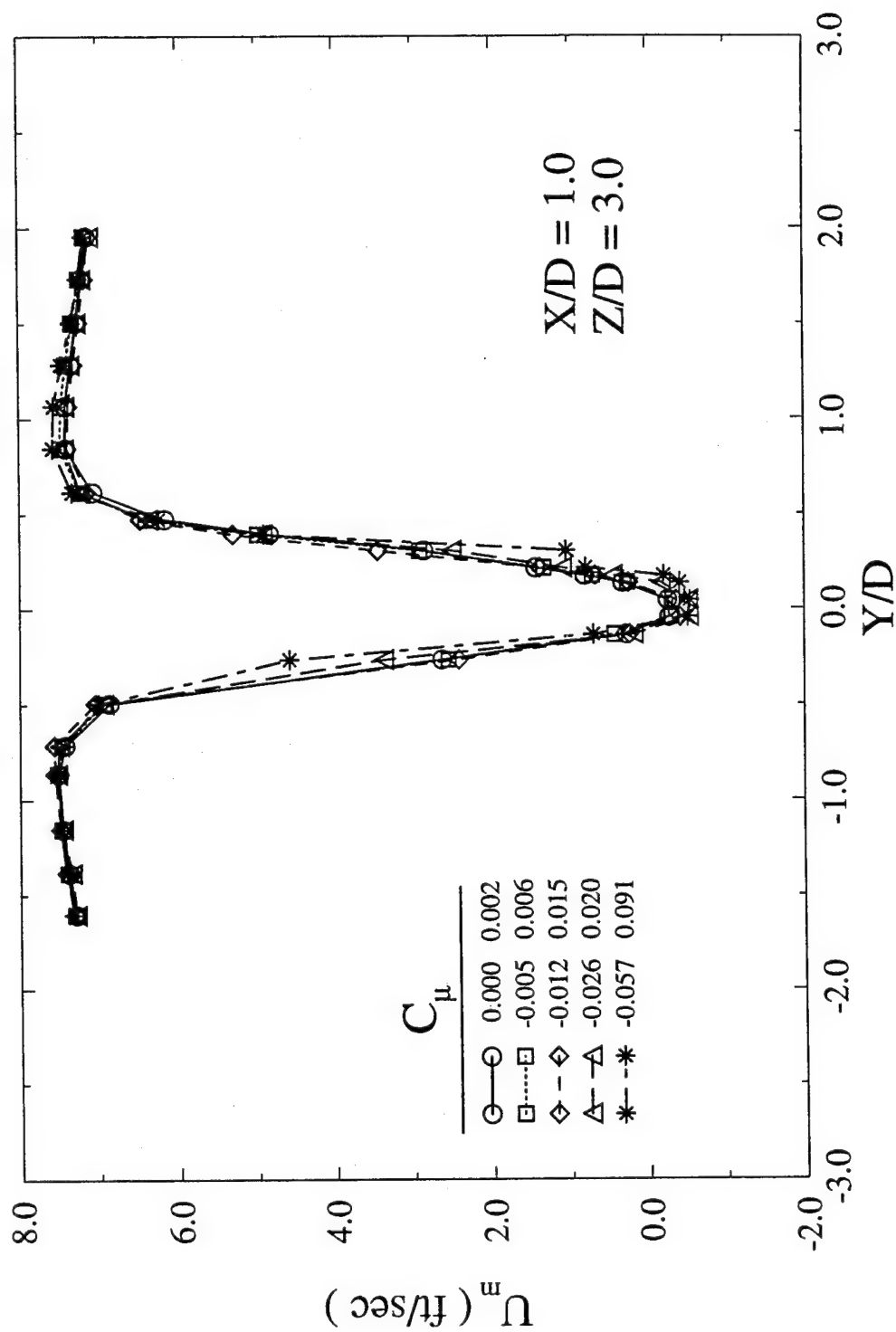
Fig. 37   Mean velocity profiles measureed when the vortices are in a symmetric configuration. This represents the base flow state.
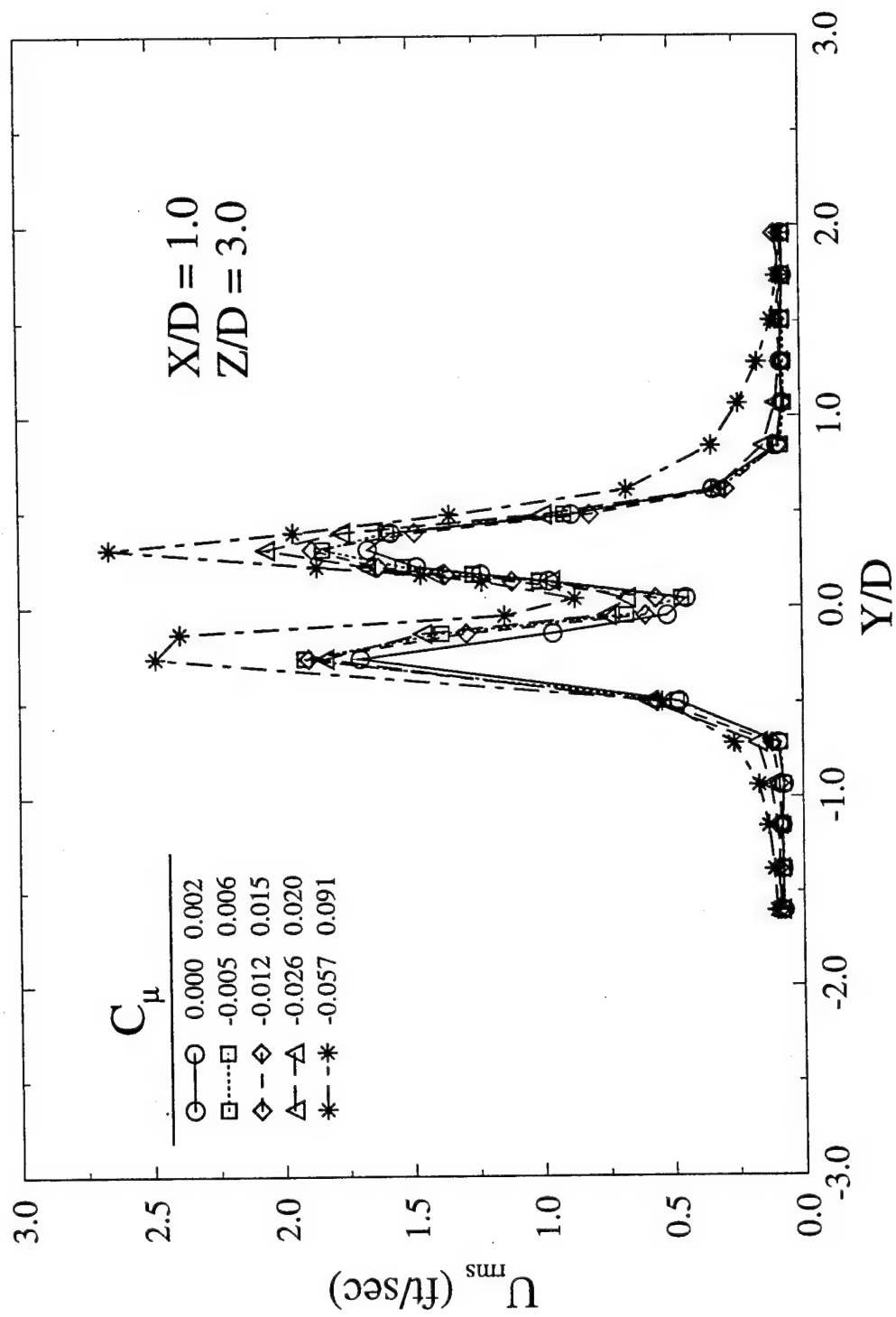
Fig. 38   Root mean square (r.m.s.) velocity fluctuation level when the flow is in its base state.
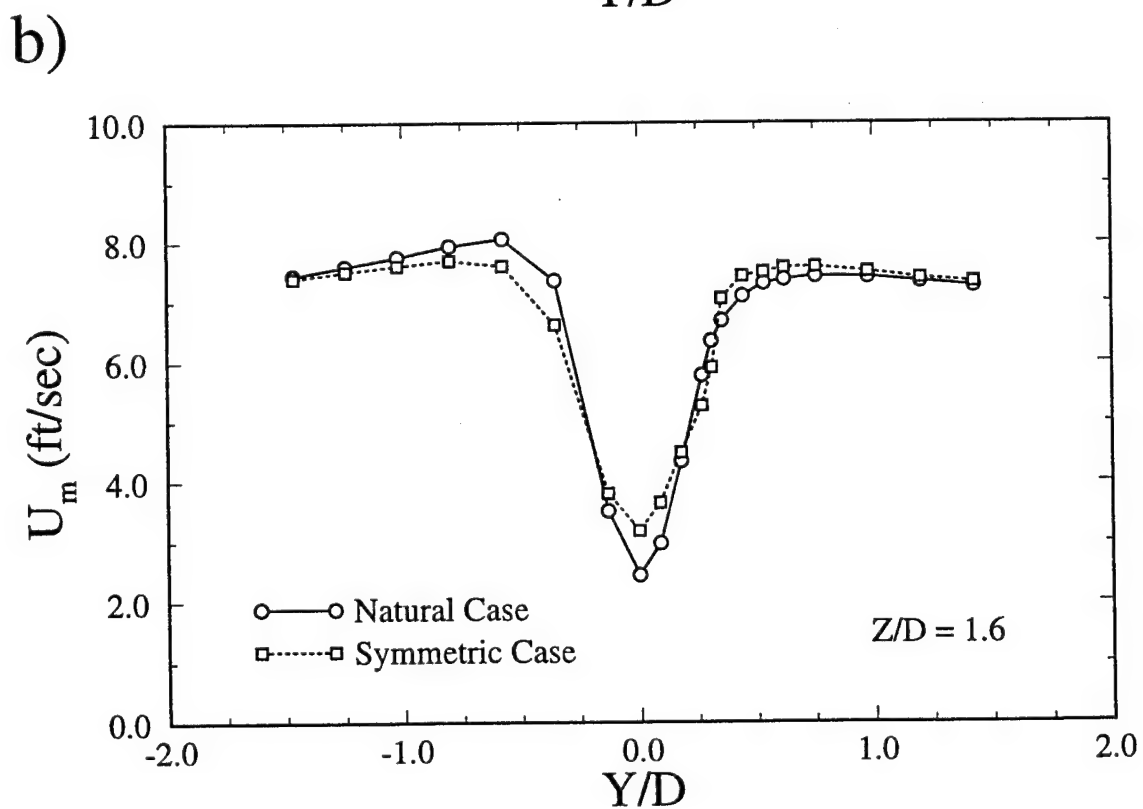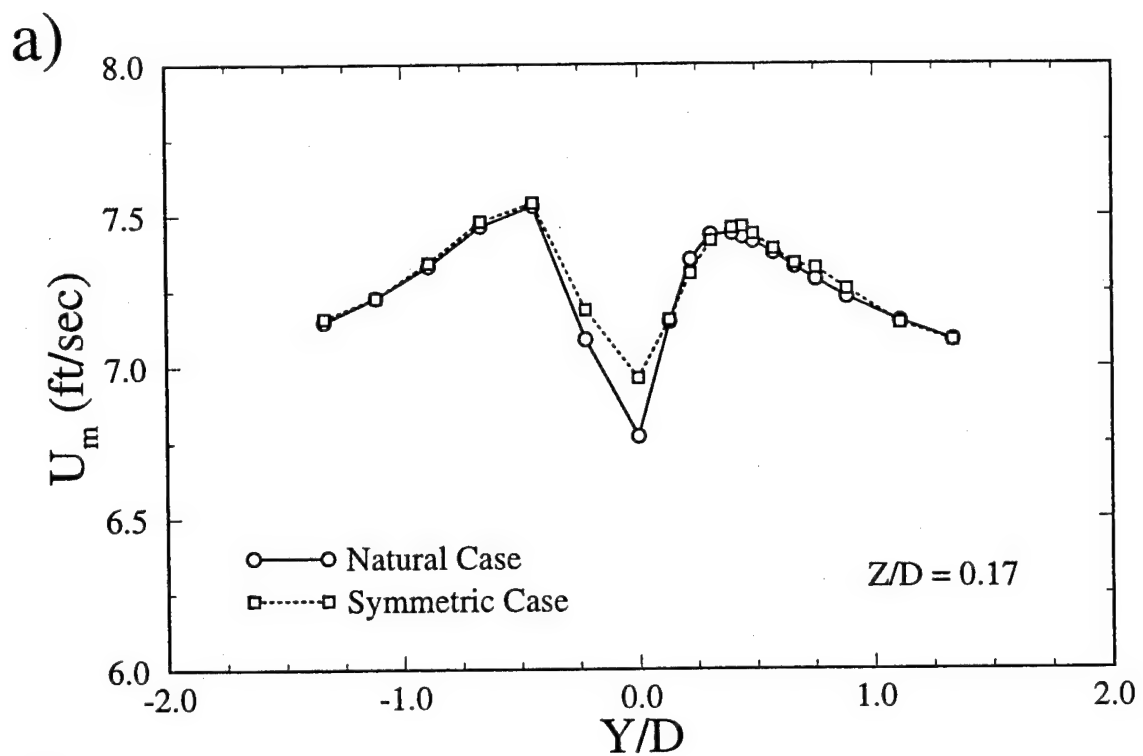
Fig. 39 Velocity profiles in the symmetric and naturally occurring asymmetric states. (a) z/D=0.17; (b) z/D=1.6; (c) z/D =3.0; (d) z/D=4.5.

c)

d)
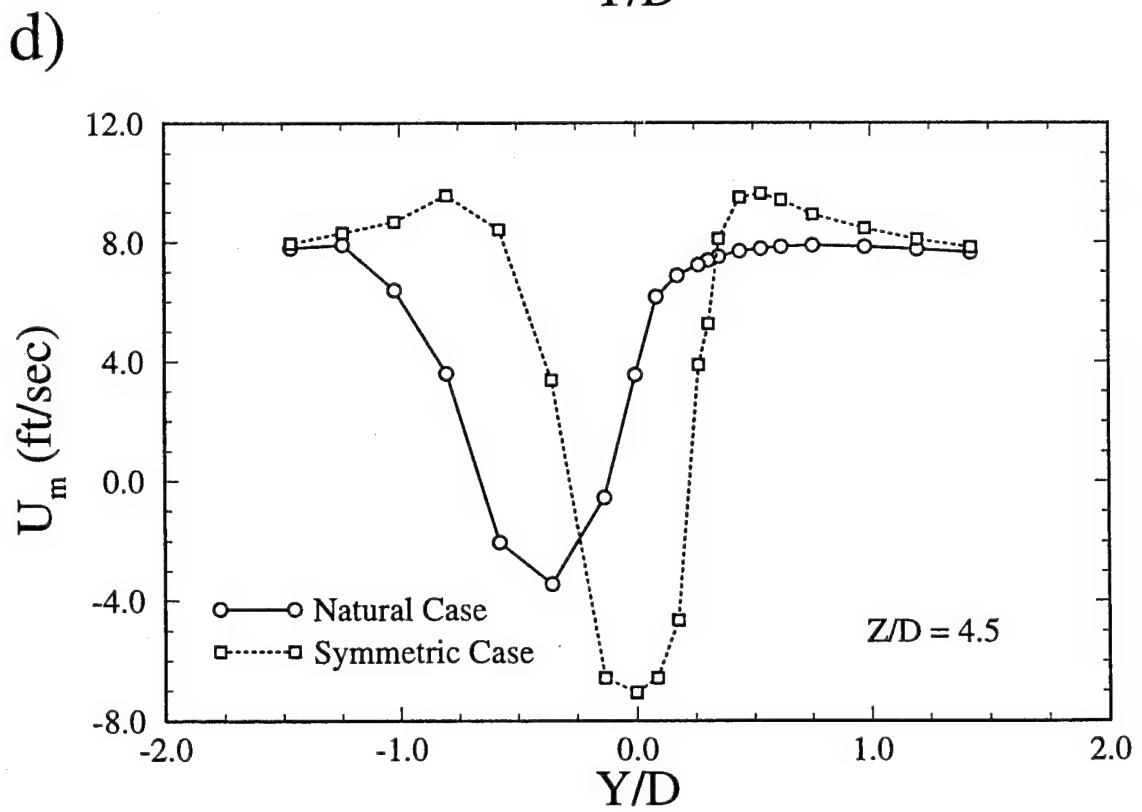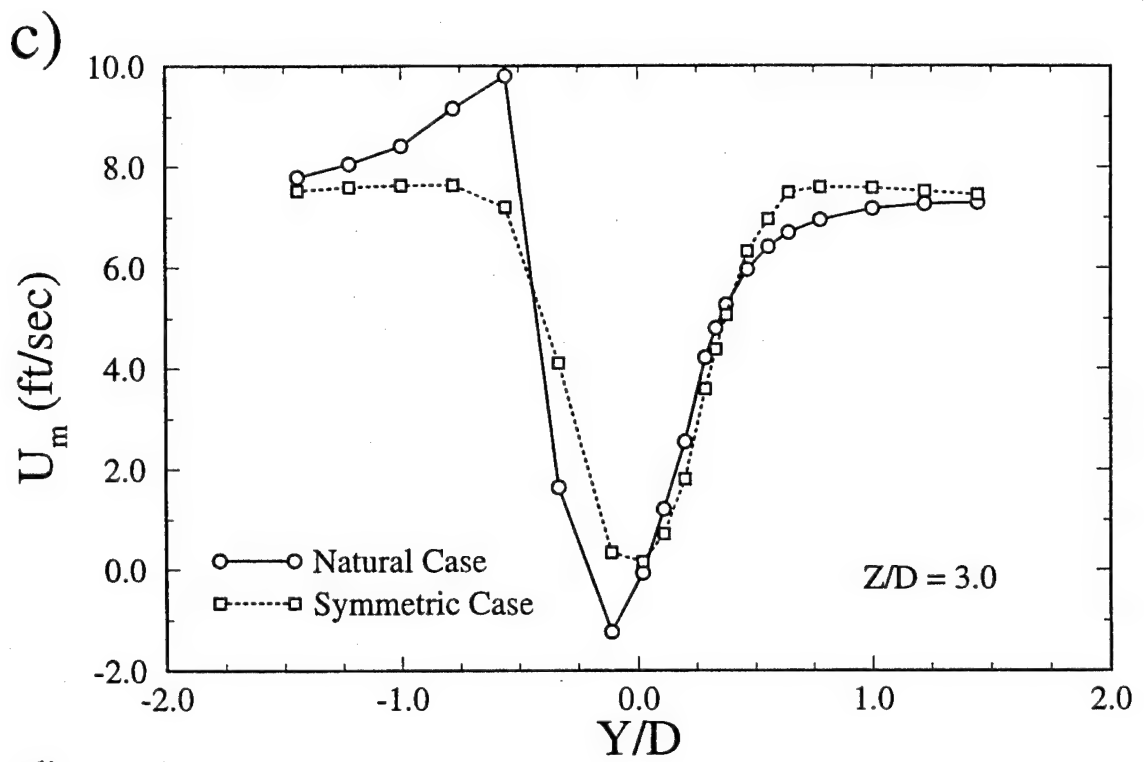
Fig. 39 (cont.)
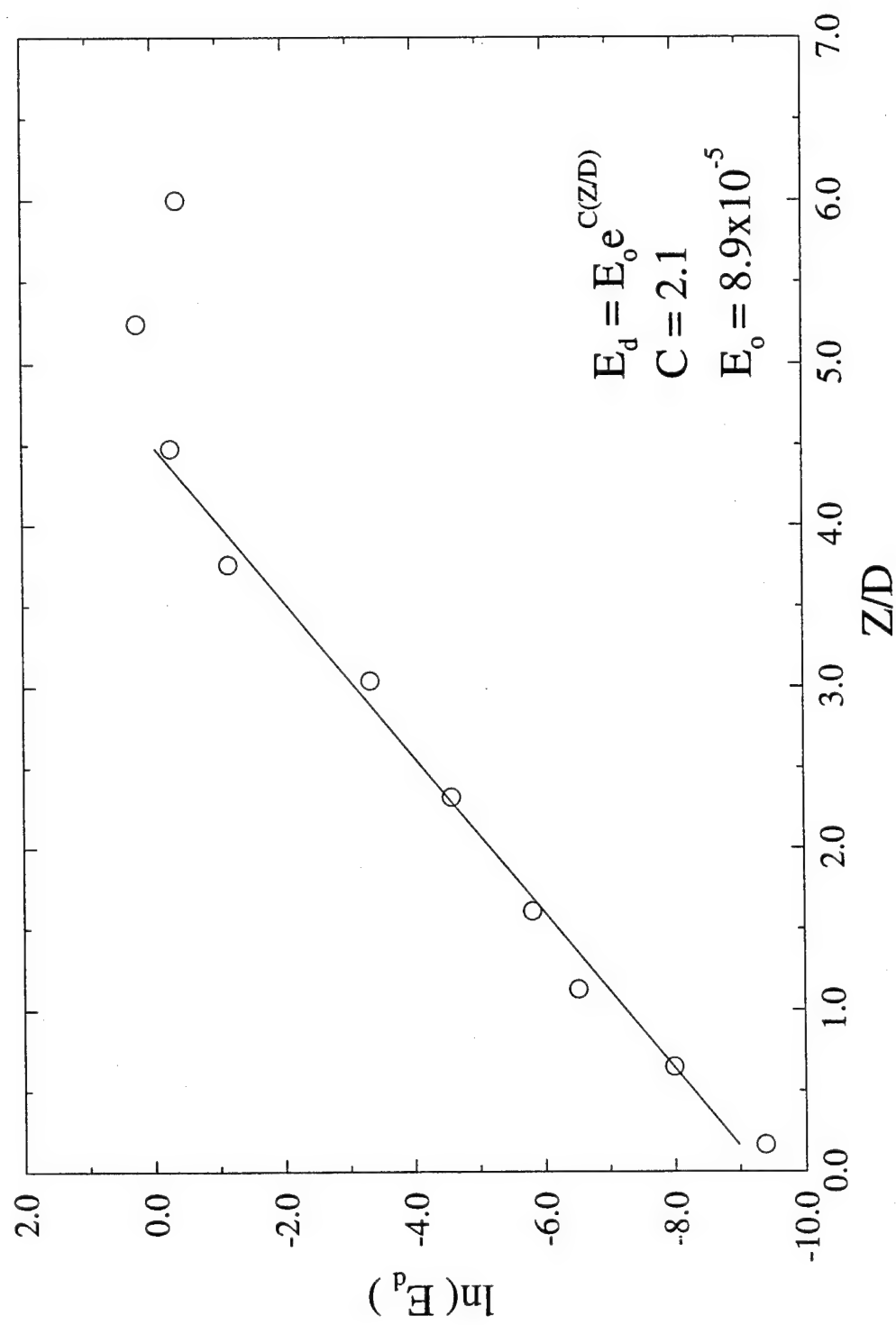
Fig. 40 Distortion energy growth along the axis of the model.

a)

b)
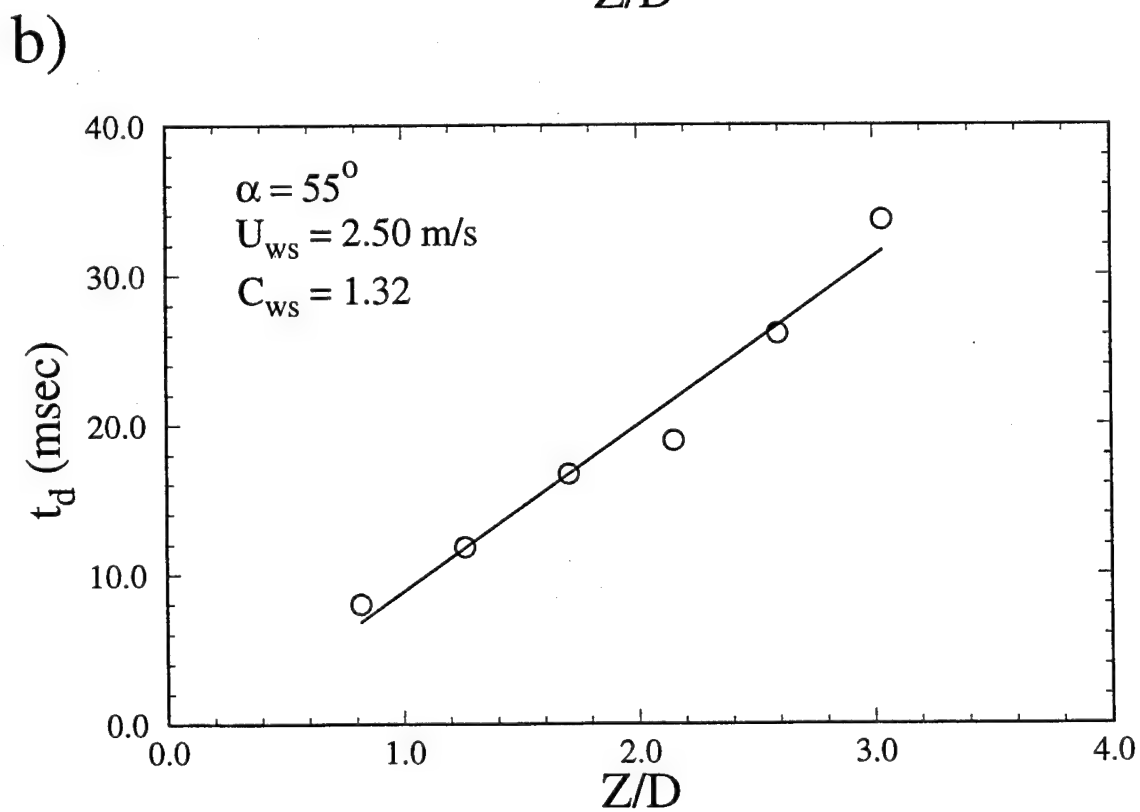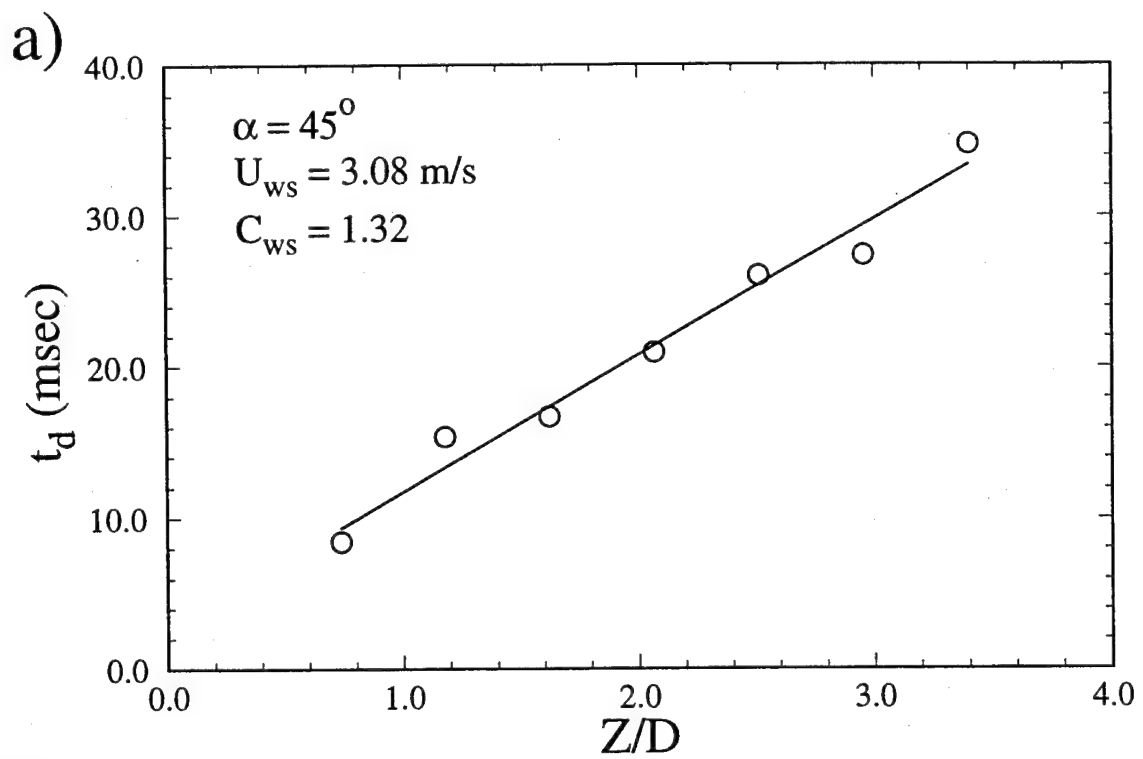
Fig. 41 Disturbance propagation speed along the axis of the model. (a) $\alpha=45^{o}$; (b) $\alpha=55^{o}$.

a)

b)
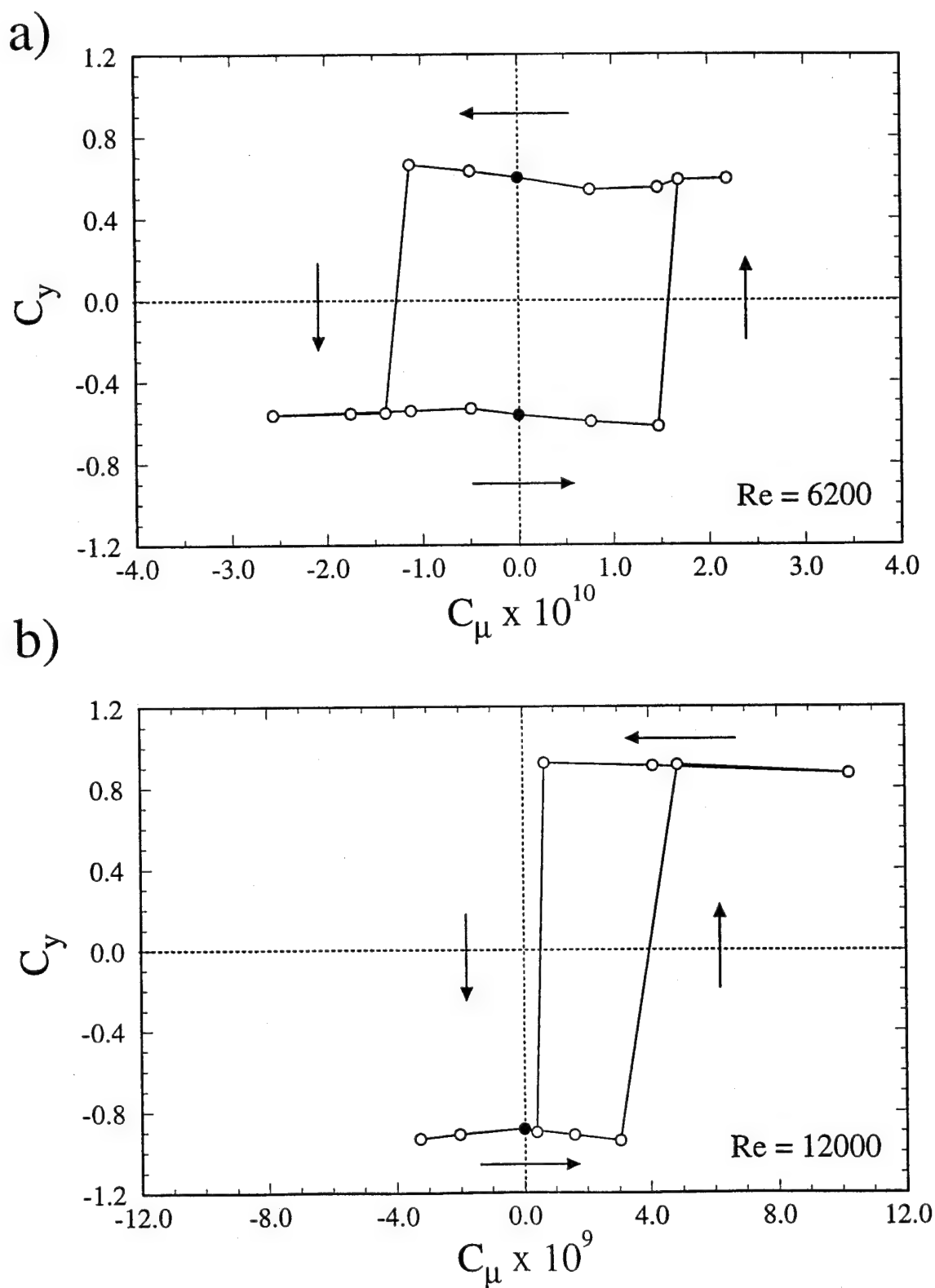
Fig. 42   The effect of Reynolds number on the side force hysteresis loop is shown at (a) Re=6,200; (b) Re=12,000; (c) Re=18,100, 24,000; (d) Re=30,000; (e) Re-36,000, 42,000, 48,100.

c)

d)

Fig. 42 (cont.)

e)

Re = 36000
Re = 42000
Re = 48100

$C_\mu \times 10^7$

C_y
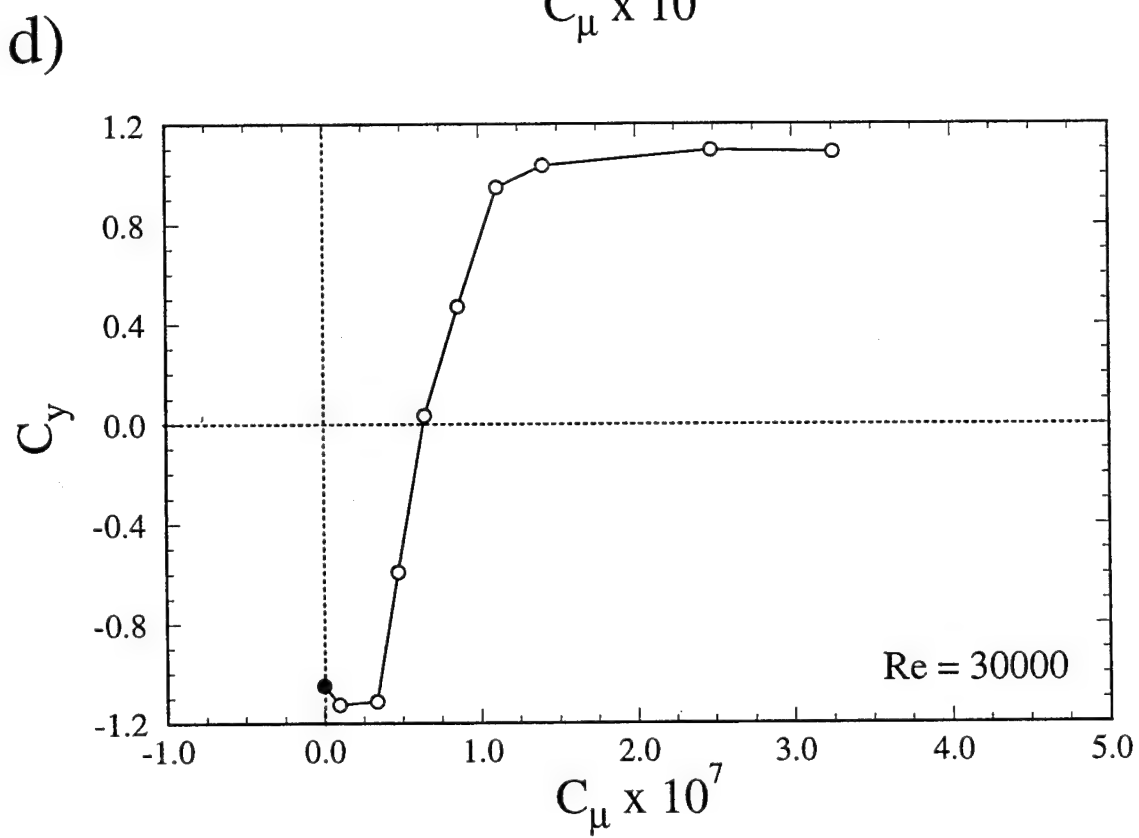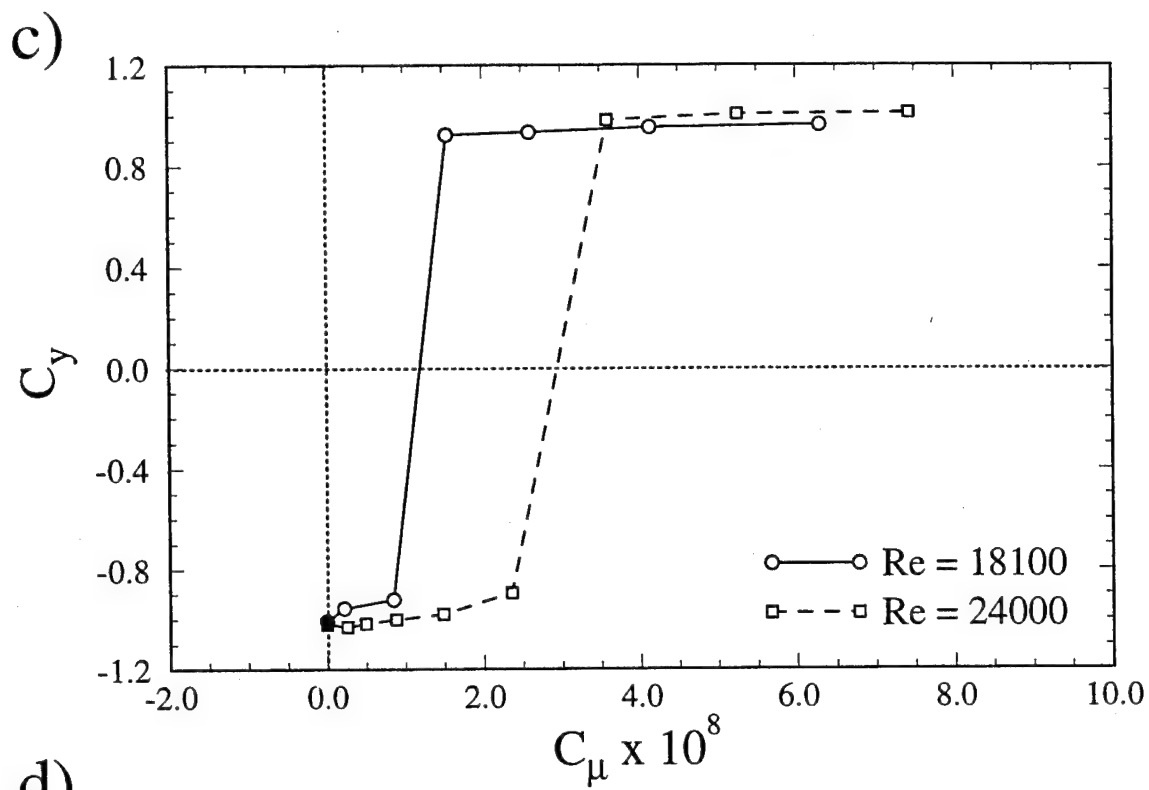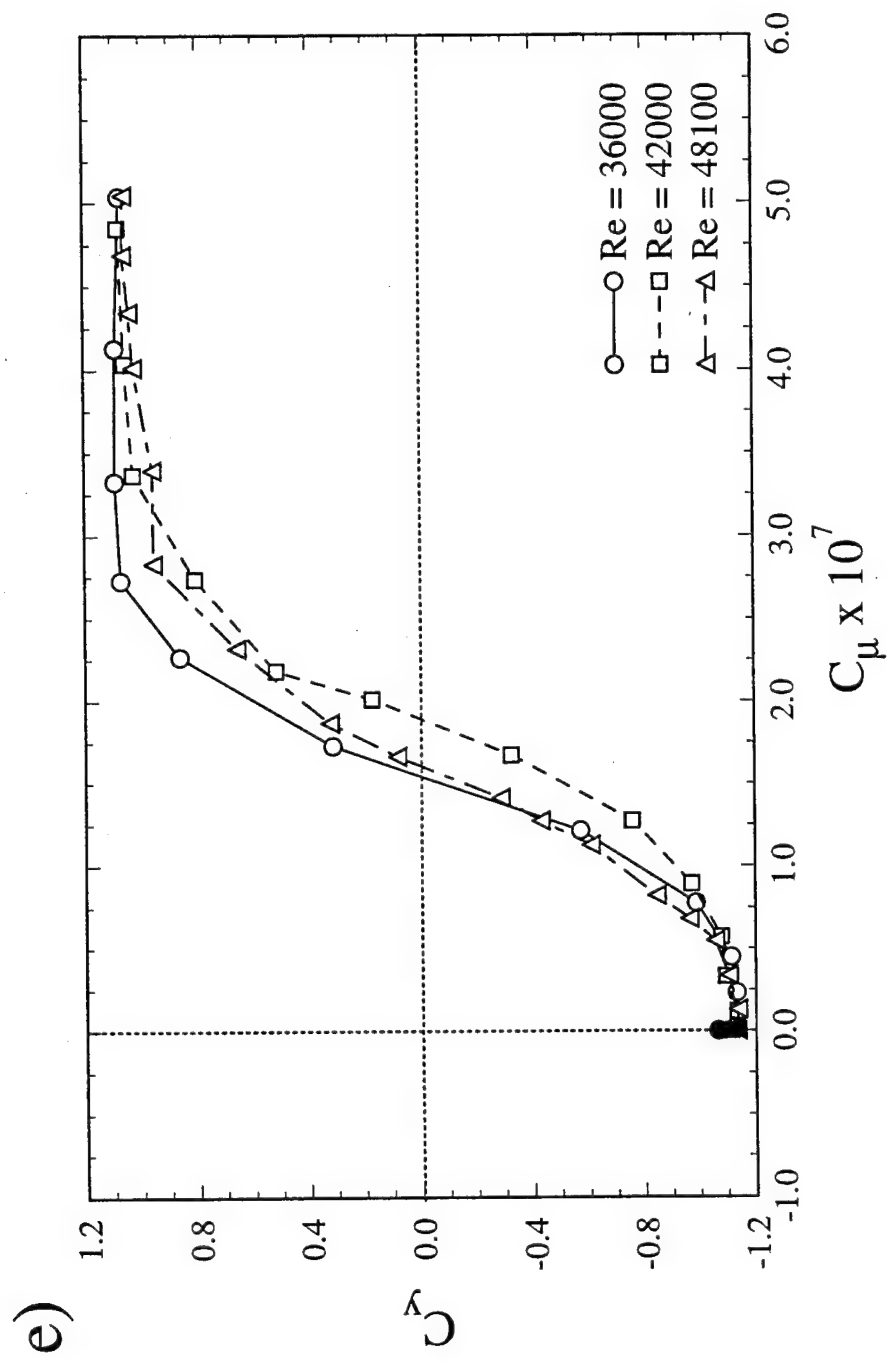
Fig. 42 (cont.)
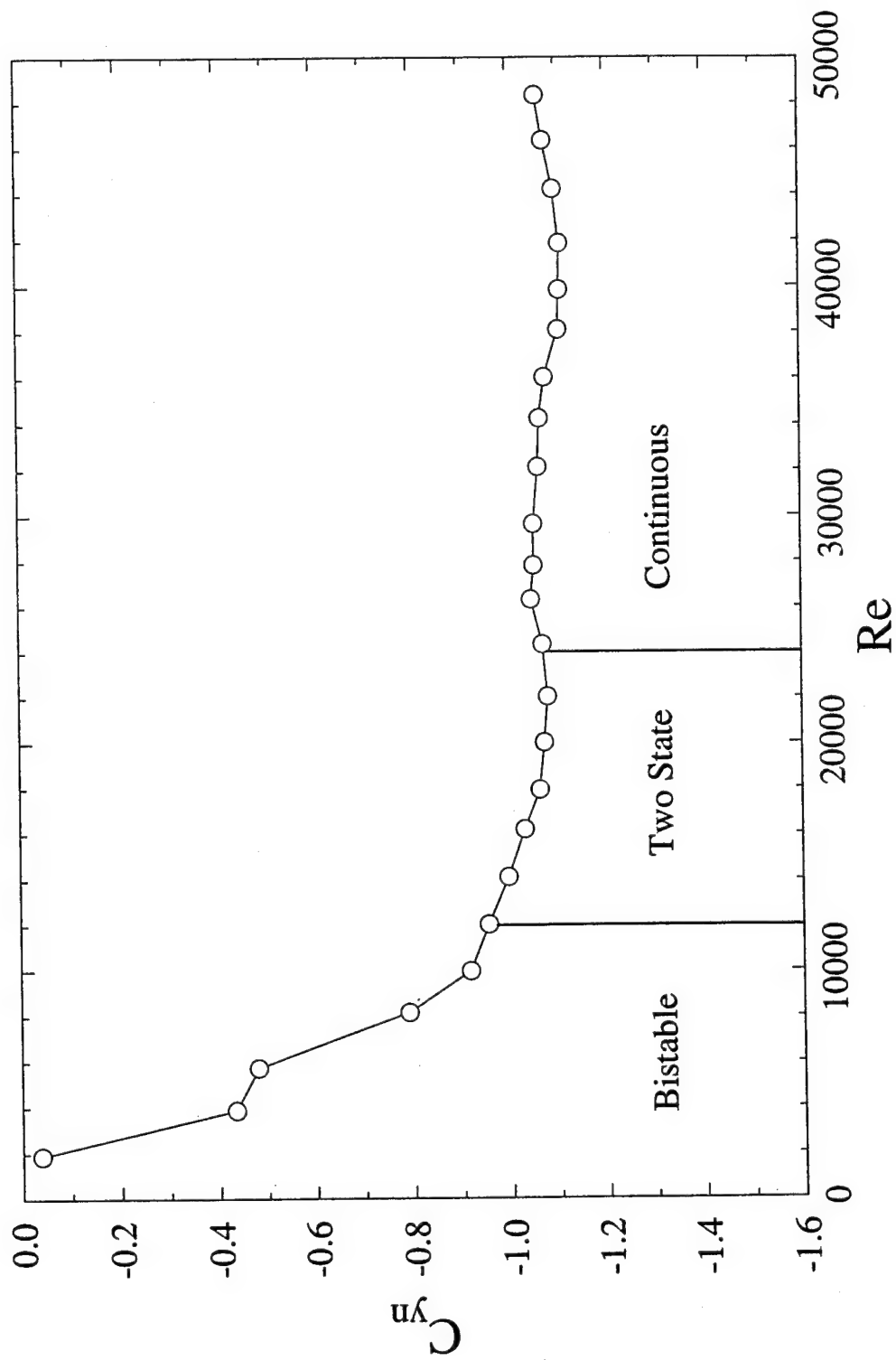
Fig. 43 The naturally occurring side force coefficient variation with Reynolds number.

$$C_\mu^* \sim Re^{3.9}$$
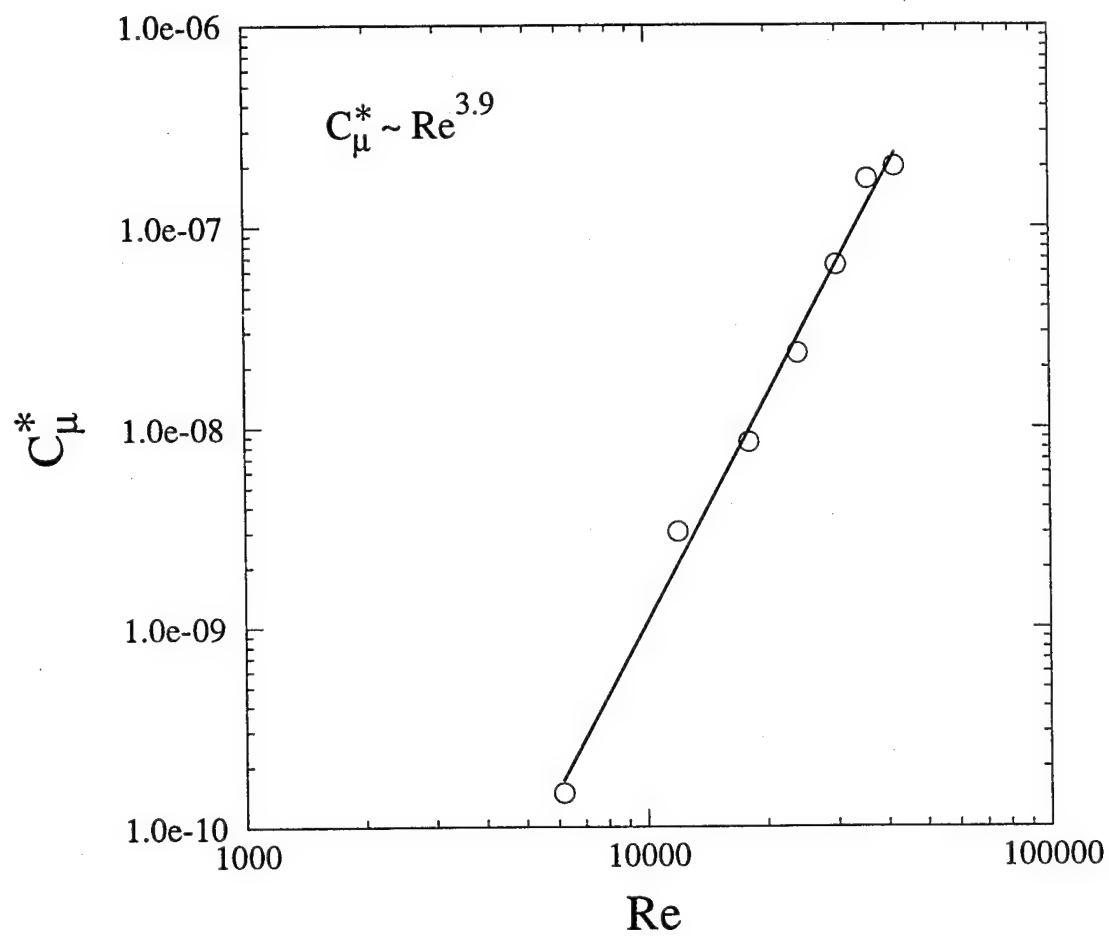
Fig. 44 Critical bleed coefficient required to achieve a symmetric state depends on the Reynolds number.
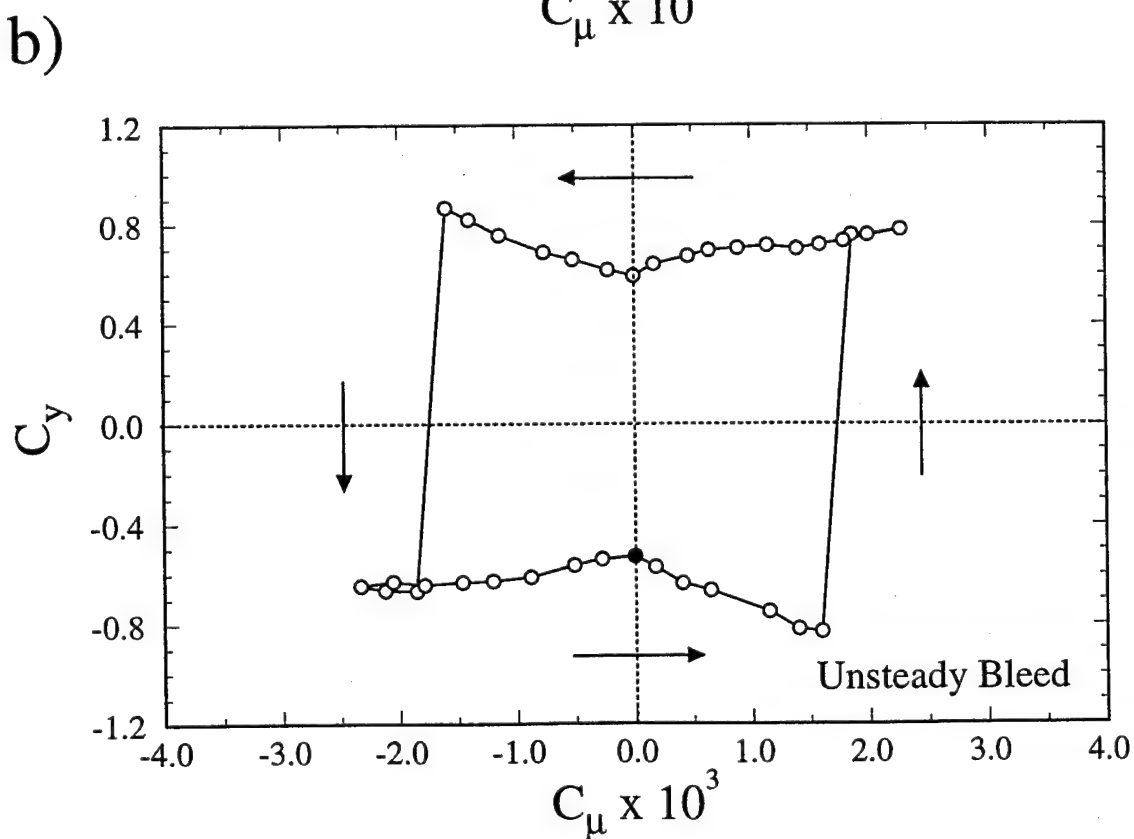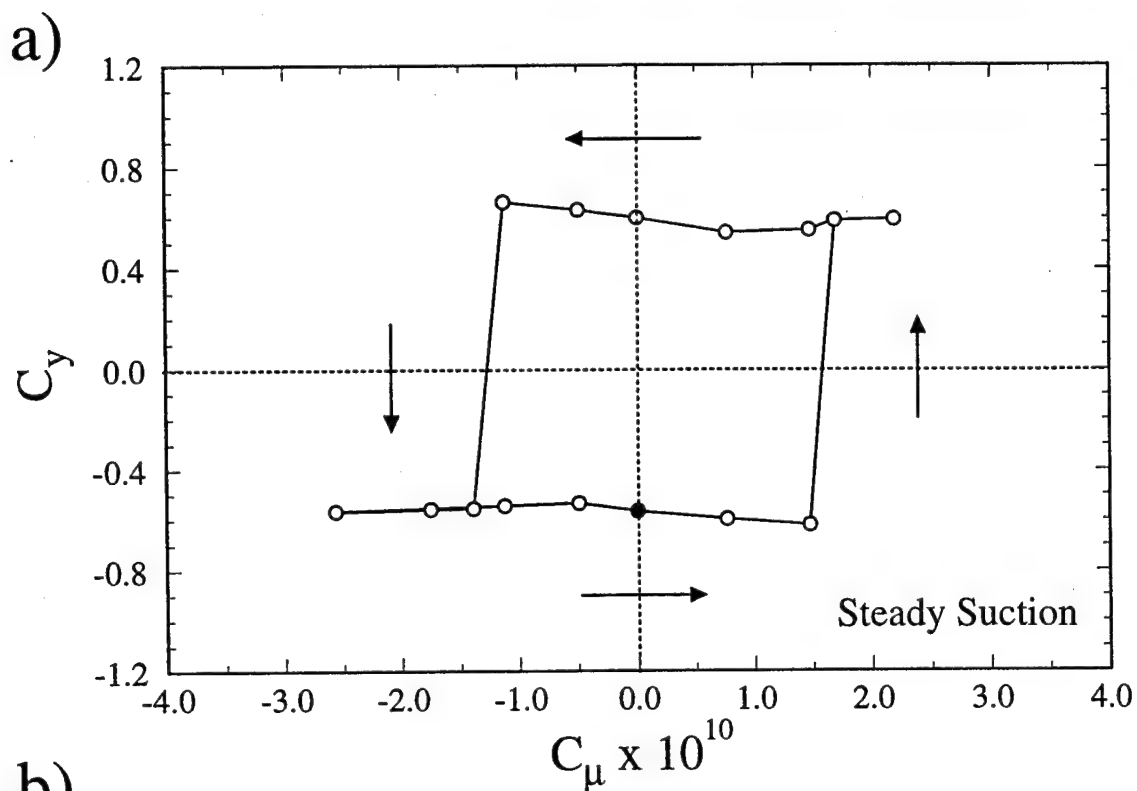
Fig. 45   Suction and unsteady bleed have similar effects on the control hysteresis loop, while blowing has an opposite effect.   (a) suction; (b) unsteady bleed; (c) blowing.

c)
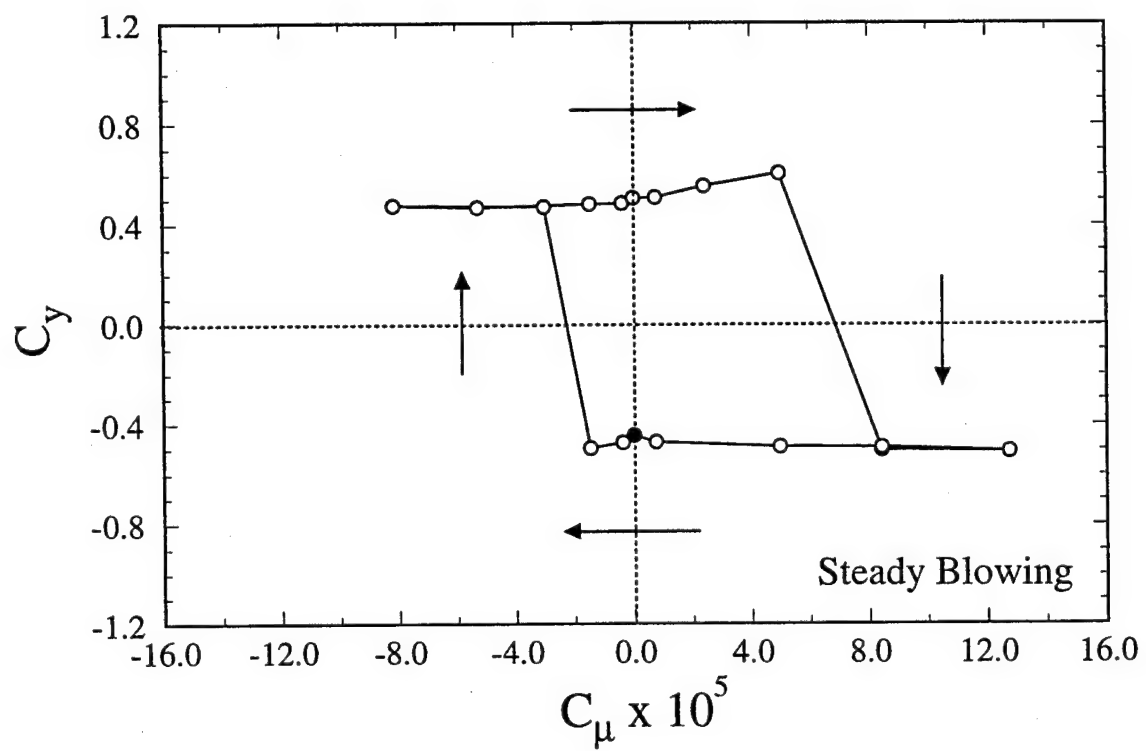
Fig. 45 (cont.)
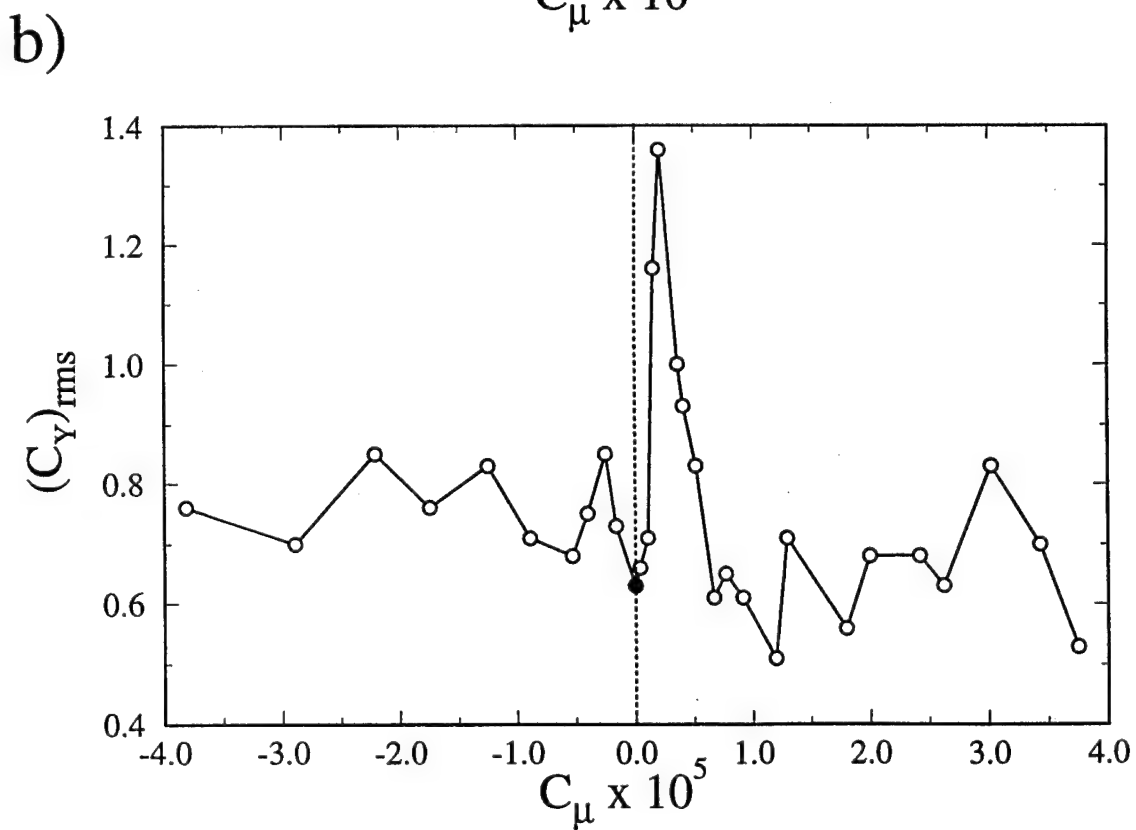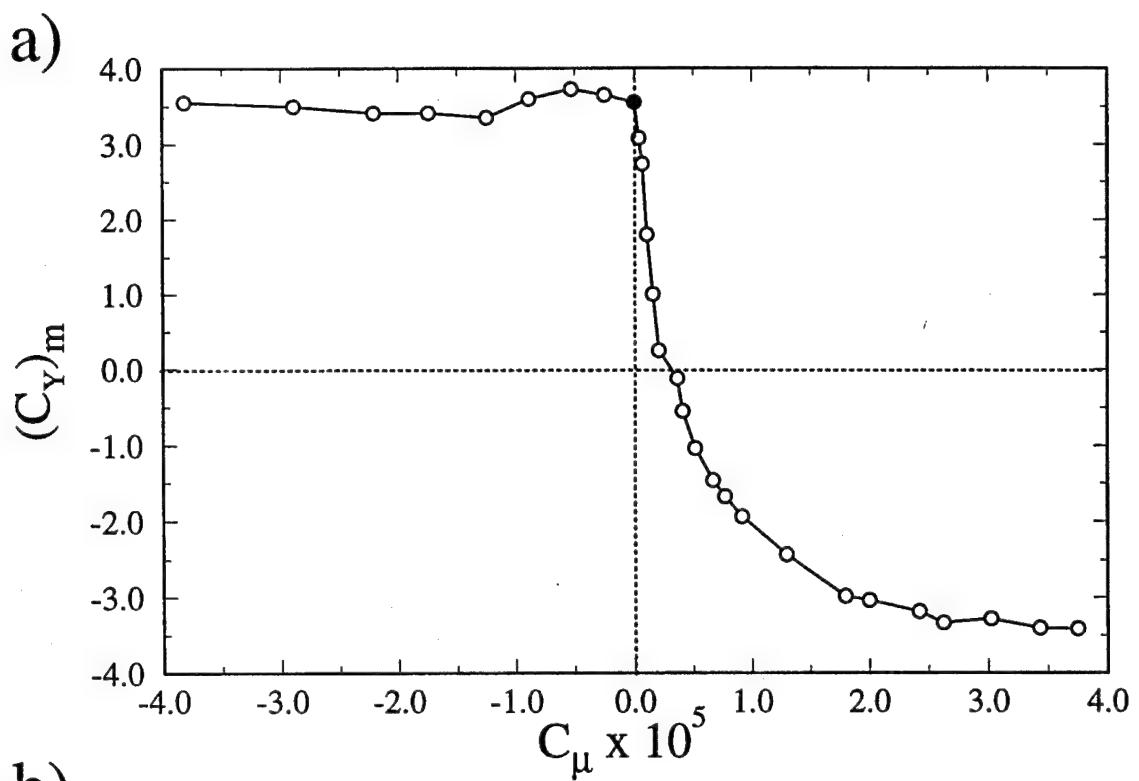
Fig. 46 Mean and r.m.s values of the side force coefficient. (a) mean Cy; (b) r.m.s.
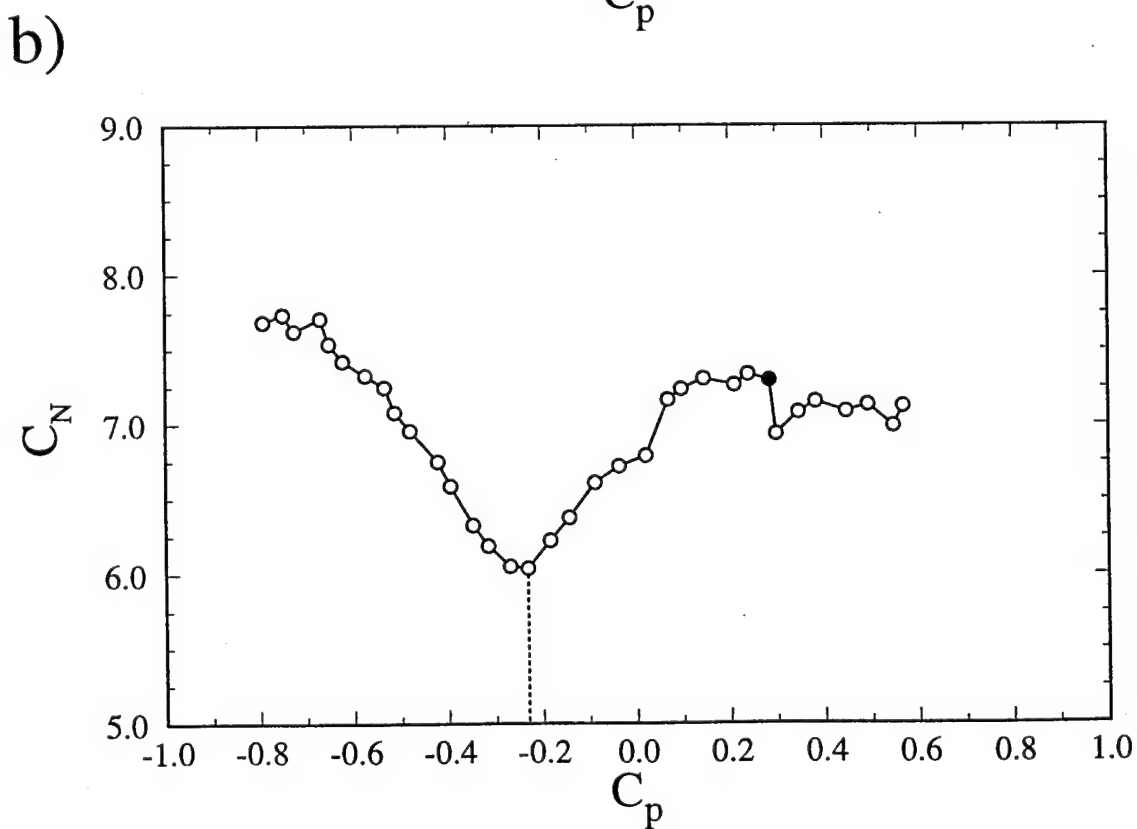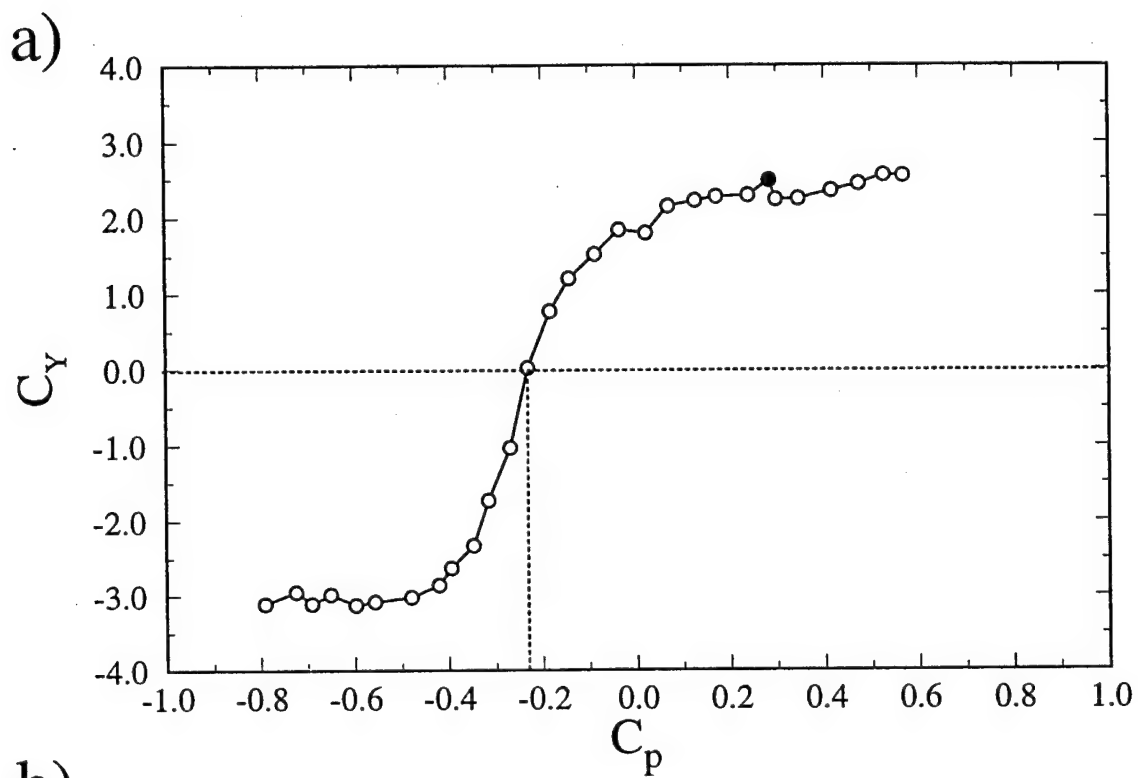
Fig. 47 Side force and normal force coefficients relation to Cp. (a) side force; (b) normal force.
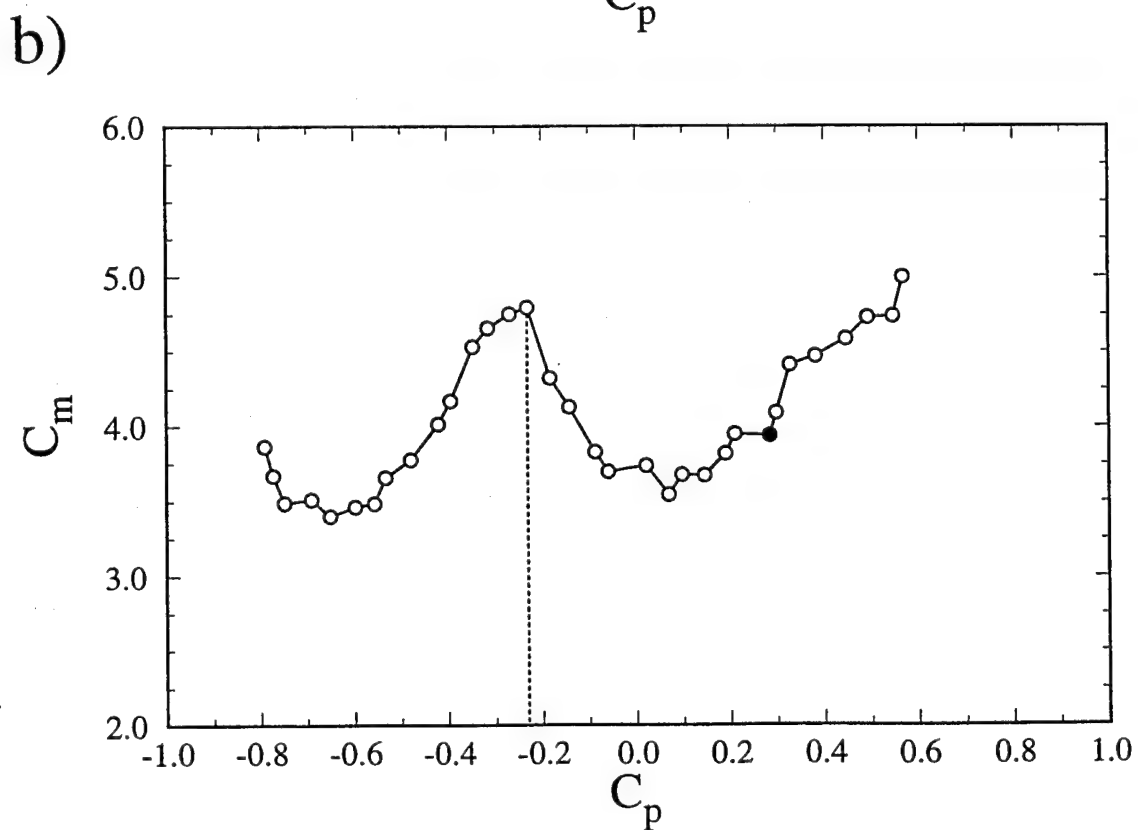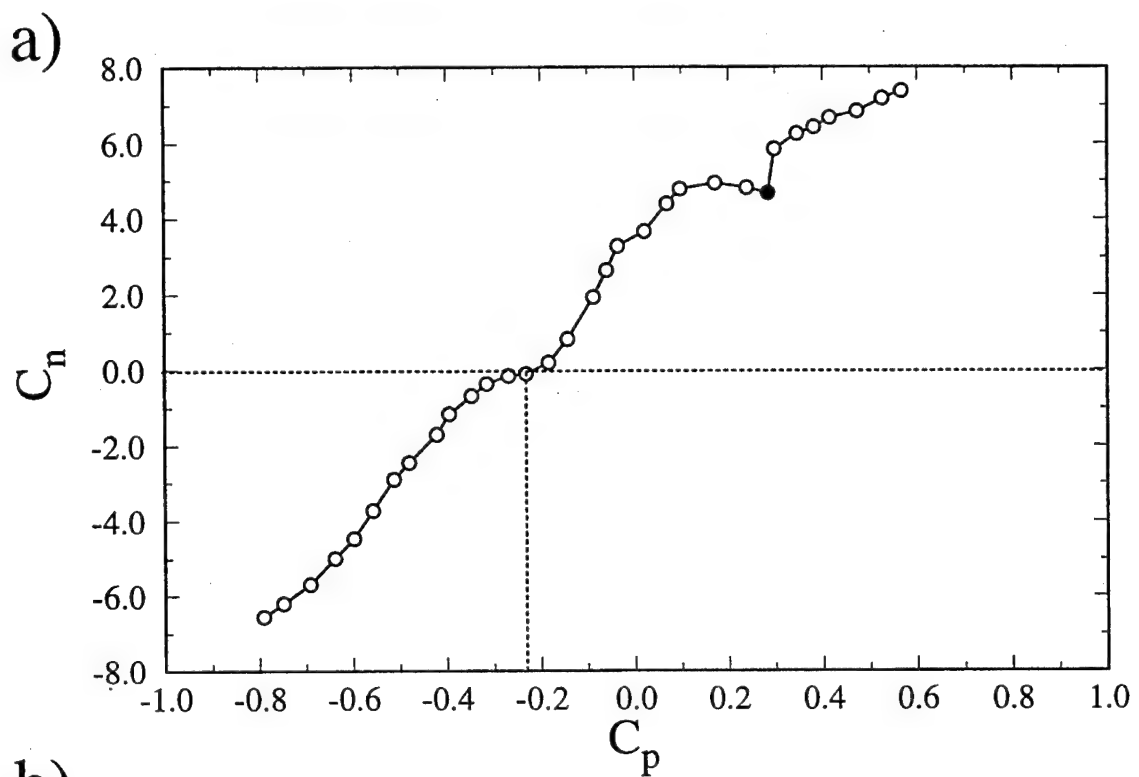
Fig. 48 Yaw and pitch moment coefficient relation to Cp. (a) yawing moment; (b) pitching moment.
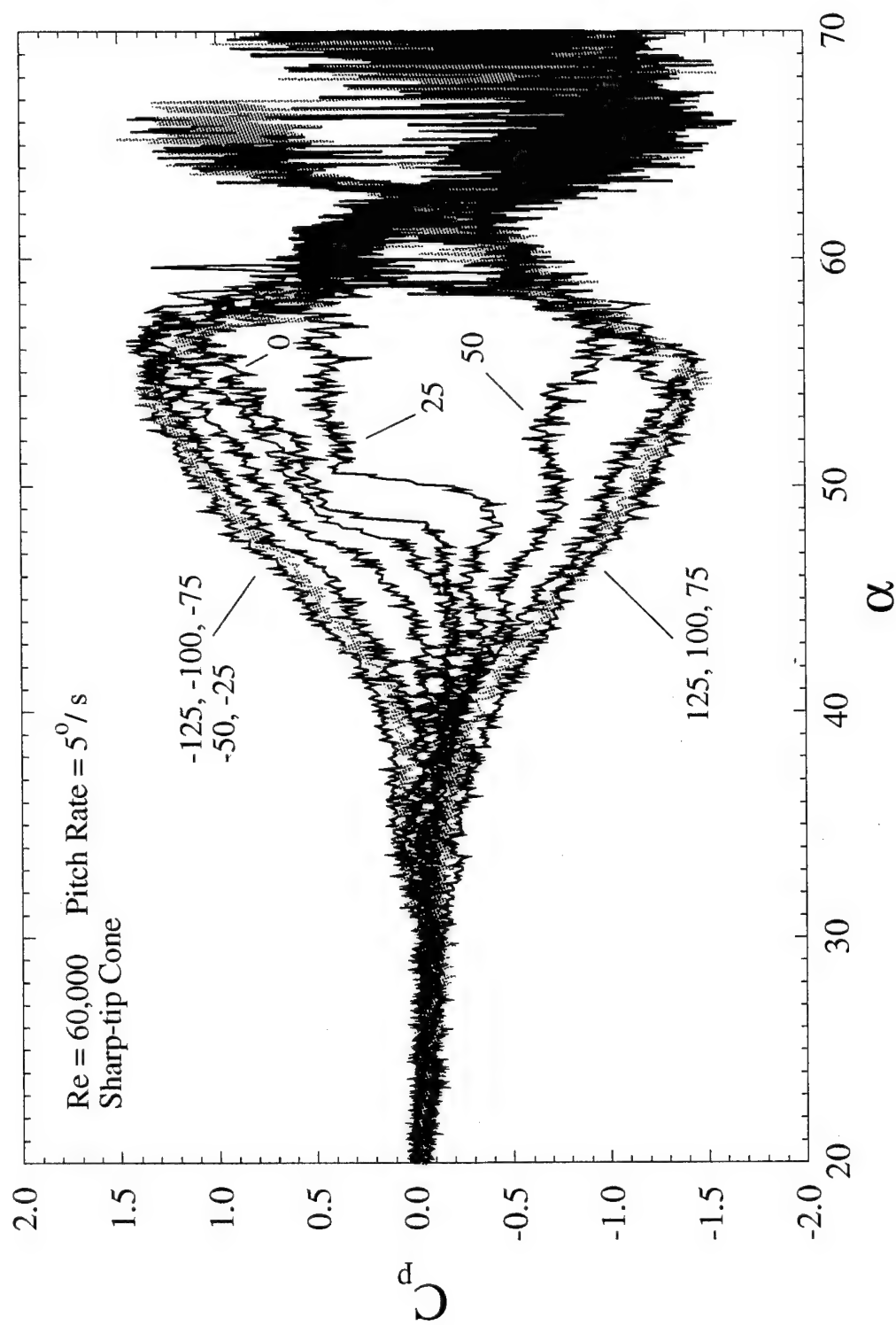
Fig. 49   Control map for the sharp-tip cone at Re=60,000, dα/dt=5°/s.   Differential
Cp vs. α is shown for different actuator settings.
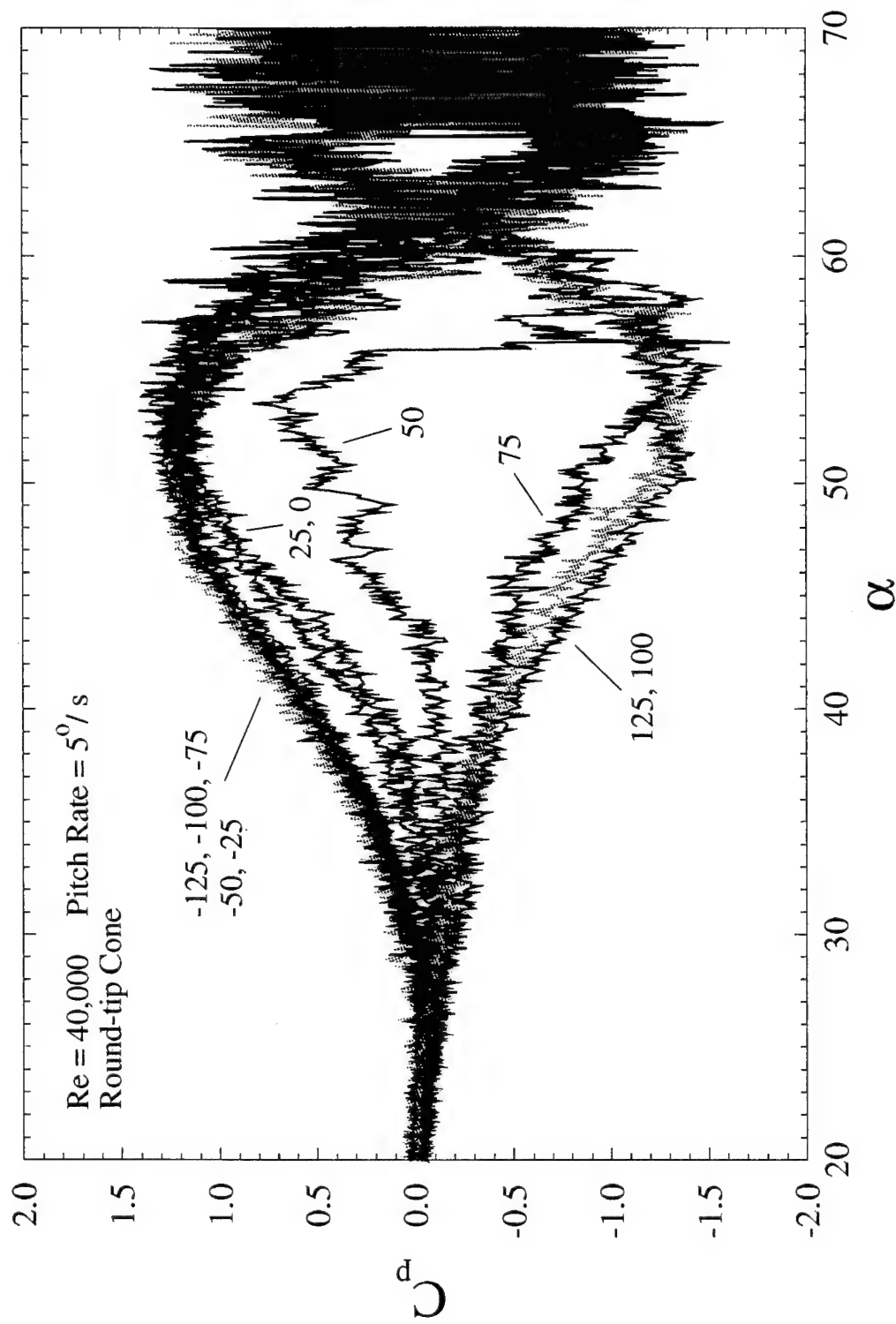
Fig. 50 Control map for the round-tip model at Re=40,000, dα/dt=5°/s. Differential Cp vs. α is shown for different actuator settings.
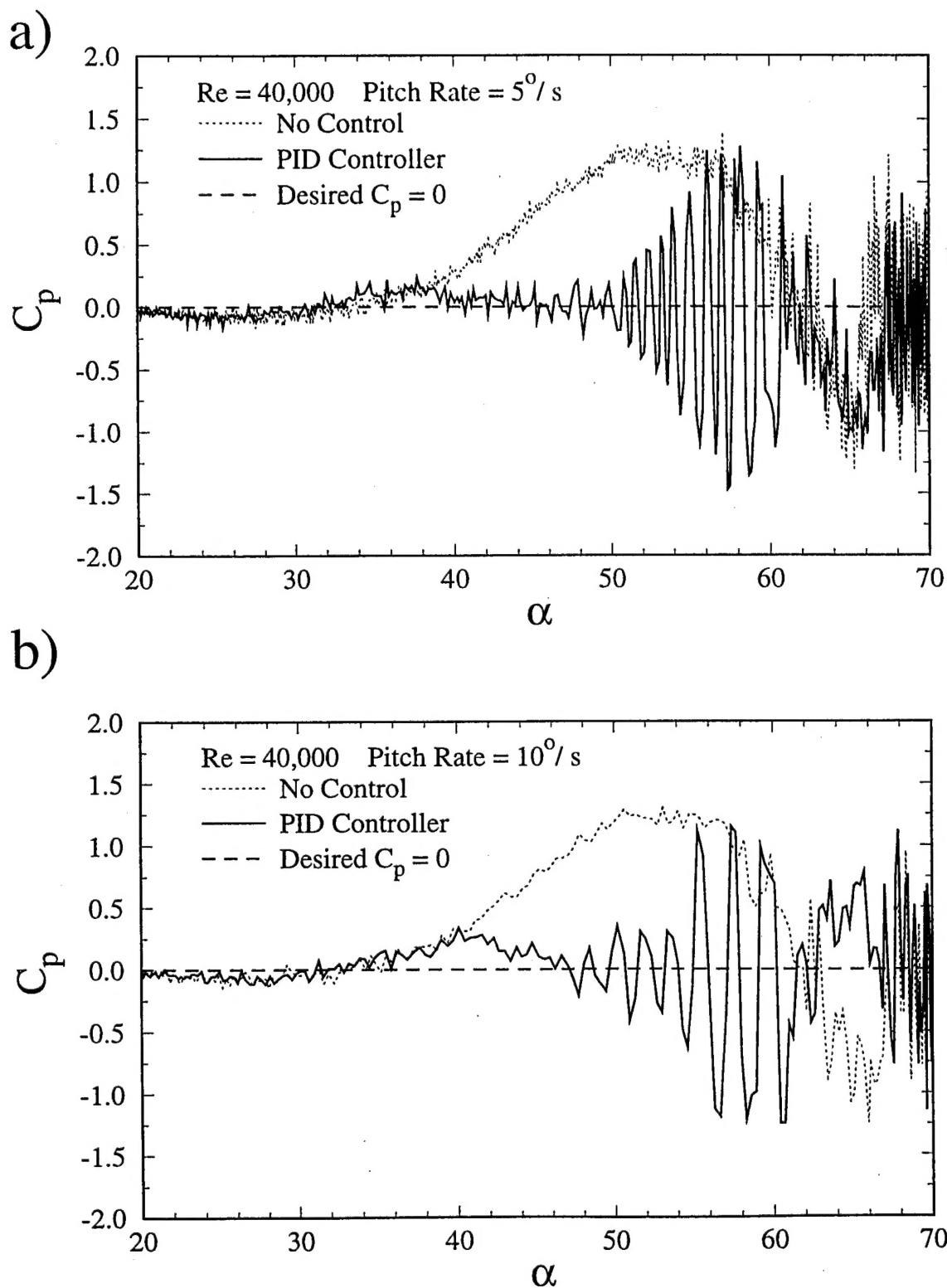
a)

b)
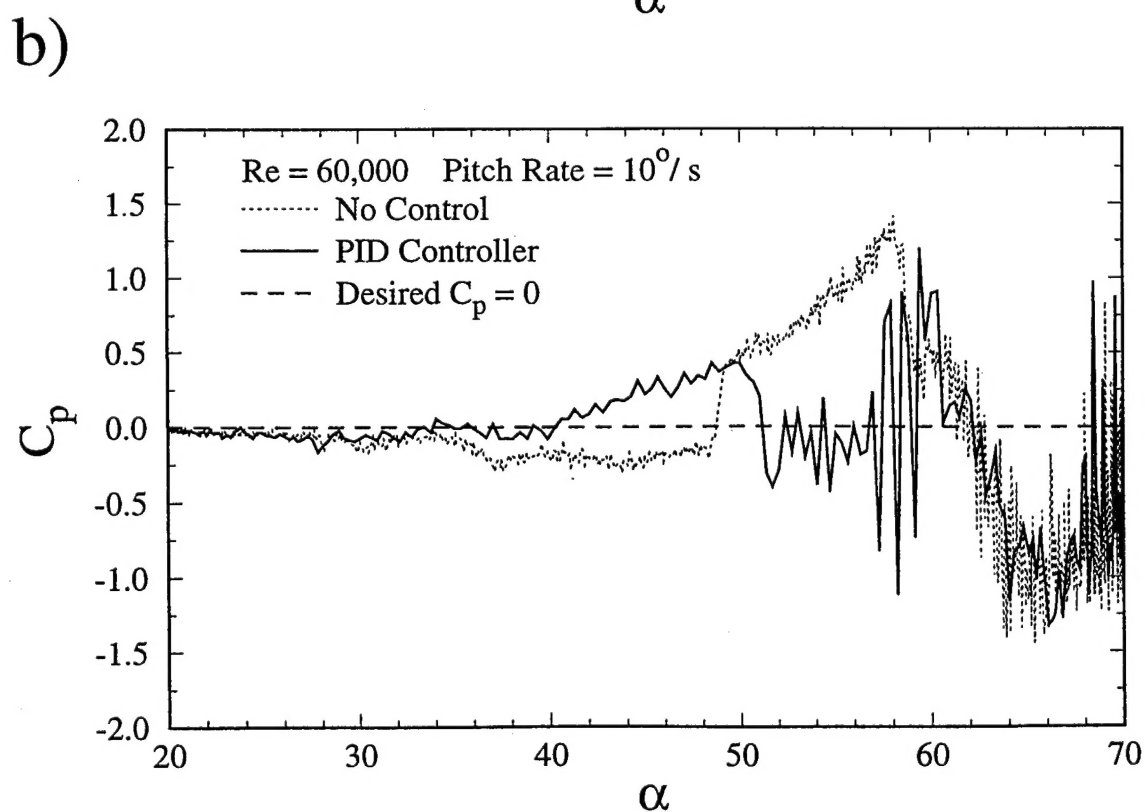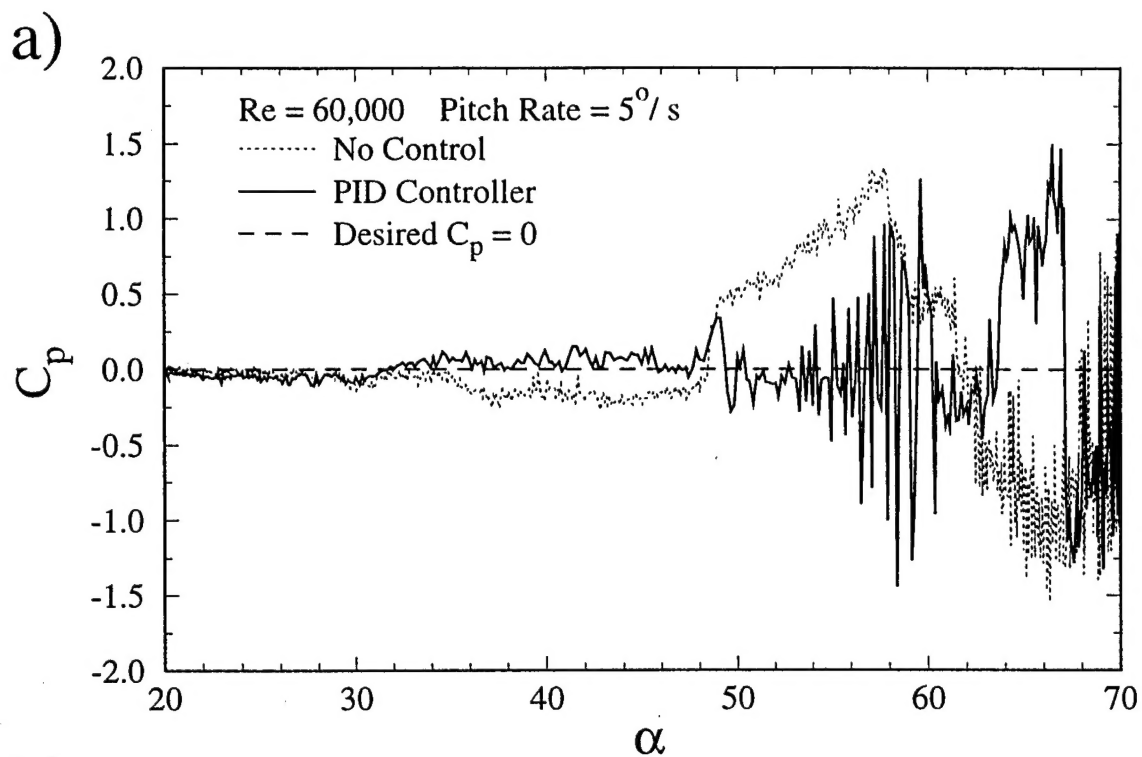
Fig. 51 PID control of the differential pressure on the sharp tip cone during pitch up maneuver. Comparisons between the natural case (dotted line) and the controlled case (solid line) are shown. (a) $d\alpha/dt = 5\ ^{o}/s$; (b) $d\alpha/dt = 10\ ^{o}/s$.

Fig. 52 PID control of the differential pressure on the round tip model during pitch up maneuver. Comparisons between the natural case (dotted line) and the controlled case (solid line) are shown. (a) dα/dt = 5 °/s; (b) dα/dt = 10 °/s.
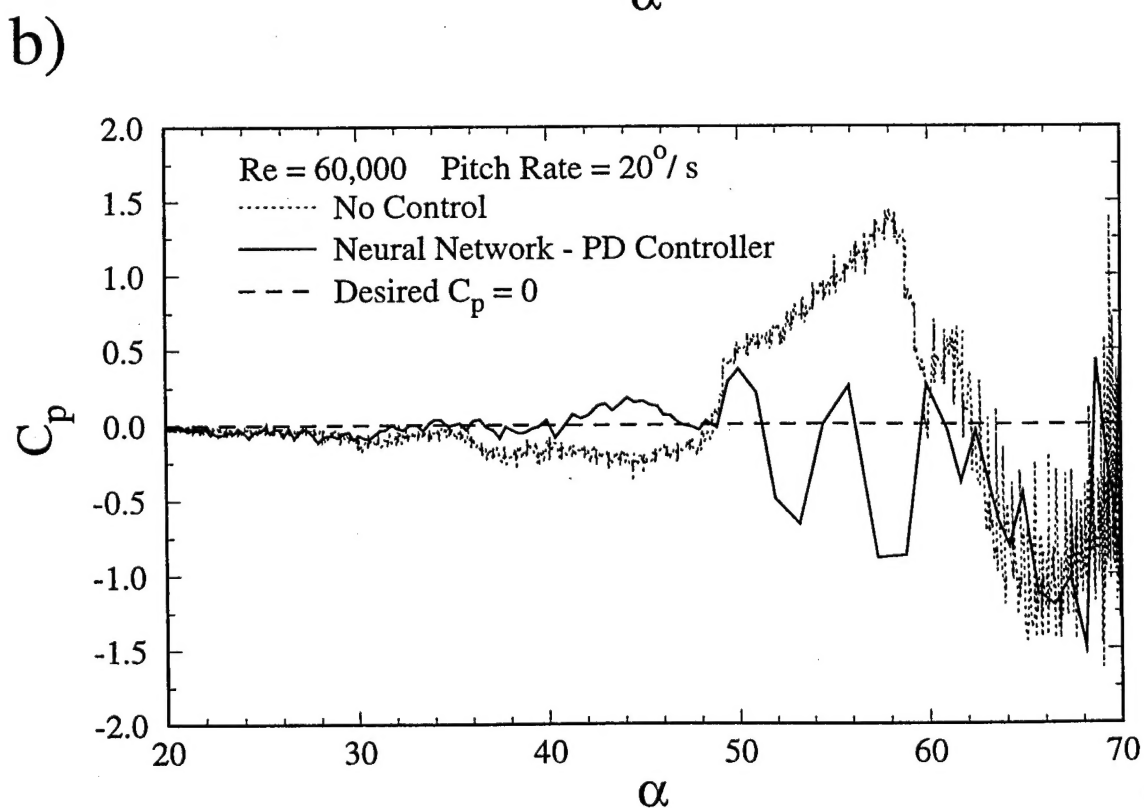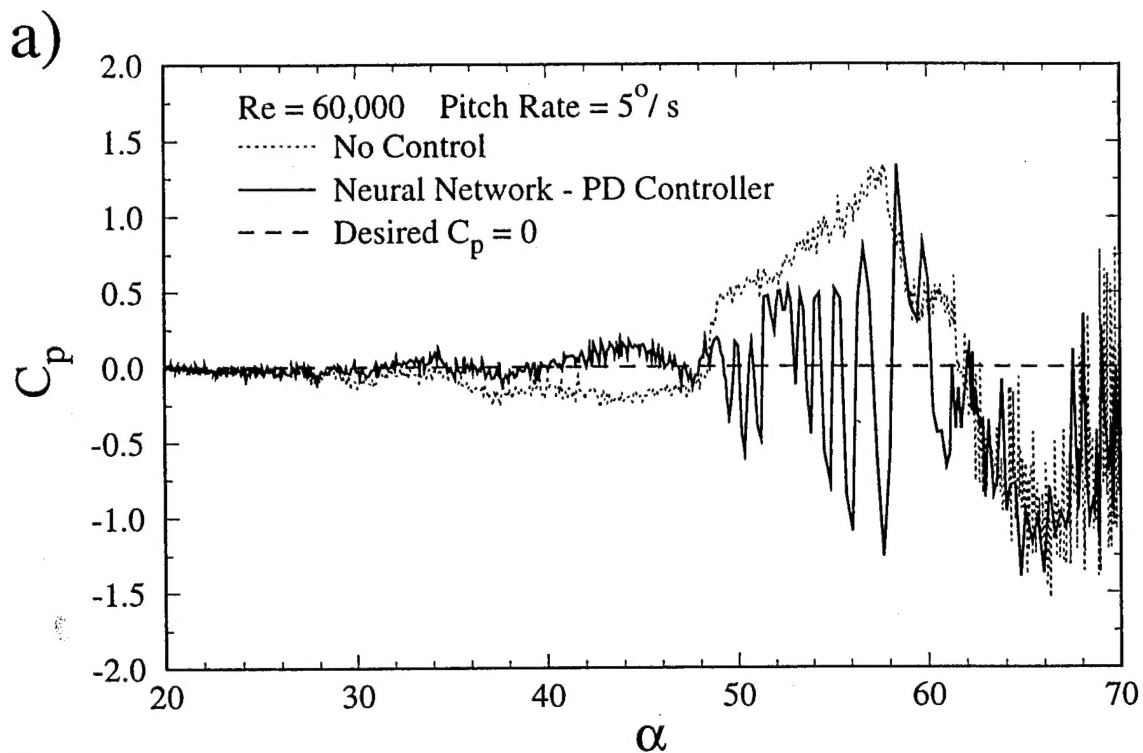
a)

b)

Fig. 53 Neural Net - PD control of the differential pressure on the sharp tip cone during pitch up maneuver. Comparisons between the natural case (dotted line) and the controlled case (solid line) are shown. (a) $d\alpha/dt = 5\ ^{o}/s$; (b) $d\alpha/dt = 20\ ^{o}/s$.
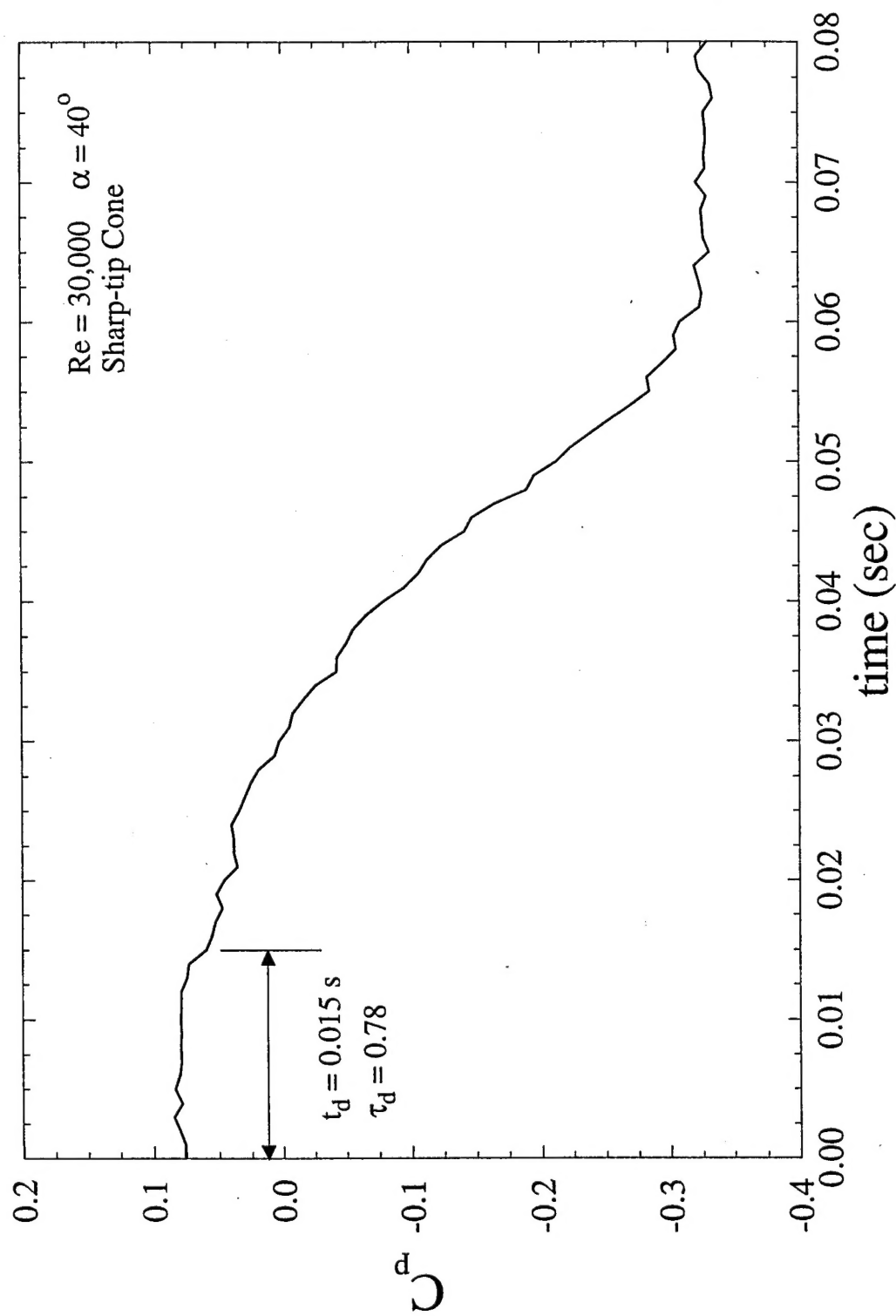
Fig. 54 Time delay between the actuator input and the response at the pressure transducers.